Impact Damage Formation on Composite Aircraft Structures

Hyonny Kim, Gabriela DeFrancisci, Zhi Ming Chen, Jennifer Rhymer, and
Jeff Tippmann
Department of Structural Engineering, University of California San Diego
La Jolla, CA 92093-0085

Project Description Paper Supporting Presentation Given at
Federal Aviation Administration Joint Advanced Materials & Structures (JAMS)
6th Annual Technical Review Meeting
19-20 May 2010, Washington State Convention & Trade Center, Seattle, WA

Abstract

The ongoing FAA research activities at UCSD are focused on impact sources that have realistic potential of producing widespread internal damage to composite fuselage and primary structure with little or no external visible detectability. Two impact sources are being actively investigated: wide area ground service equipment/vehicle contact, and high velocity hail ice impact. Stringer and frame-stiffened composite panels, designed to represent fuselage structure, have been fabricated. These were subjected to indentation loading using a “rigid” aluminum and a deformable rubber bumper (from beltloader). While localized damage and penetration was produced with the rigid indentor head, the rubber bumper did not create localized damage, instead exciting extensive stringer delamination that initiated near the shear ties (reaction points). The hail ice impact activity seeks to establish a database for the formation of damage by high velocity ice impacts, and develop models for predicting damage initiation failure thresholds as well the final state of damage produced.

1.0 Introduction

1.1 Overview

Impact damage resulting from collisions of ground vehicles/equipment with aircraft structural components, as well as from events such as hail and bird strikes, is a significant source of damage to commercial aircraft that has the potential to go by undetected. Impacts by hail and birds can occur at in-flight velocities, thereby posing significant threats to the structure. More commonly occurring, however, are blunt impact threats such as ground maintenance and service vehicles, equipment, etc., as shown in Figure 1. Ground service equipment (GSE) account for a significant percentage of damage occurring to commercial transport aircraft. 50% of major damage has been recorded to be caused by baggage vehicles and 60% of minor damage caused by collision with ground vehicles/ equipment (International Air Transportation Association [1]), costing the industry US$4 billion per year. This occurs during cargo movement while loading the aircraft, or docking of GSE around the aircraft doors. The areas in close vicinity of the doorway openings, while reinforced with metallic “scuff plates” to protect against accidental damage, are not sufficient as damage is often incurred beyond the coverage of the reinforcement. Figure 2 shows some examples of damage occurring at locations away from doors, and a belt-loader interfacing an aircraft. With new all-composite fuselage transport aircraft coming into service, significantly more composite skin surface area is exposed to such impacts. To address the difficulties that exist in being able to predict and detect the damage resulting from blunt impact, and to aid in assessing its effect on structural performance, focused investigation on the development of impact damage is needed. Of particular interest is damage that can be difficult to visually detect from the exterior, but could be extensive below the skin's outer surface. Extensive sub-surface damage (typically delamination, backside fiber failure) usually forms when impacts occur at levels just exceeding the amount needed to initiate failure (Kim et al. [2], Kim and Kedward [3]). This level is referred to as the failure threshold energy. Additionally, damage from blunt impacts to internal stiffeners can be extensive, as well as debonding between the stiffener and the skin. Of critical concern is whether such extensive damage can result in the structure losing ultimate and even limit load capability.

Figure 1. Maintenance/Service Threat Sources: Ground Vehicles, Luggage Carts, Cargo Containers, etc.

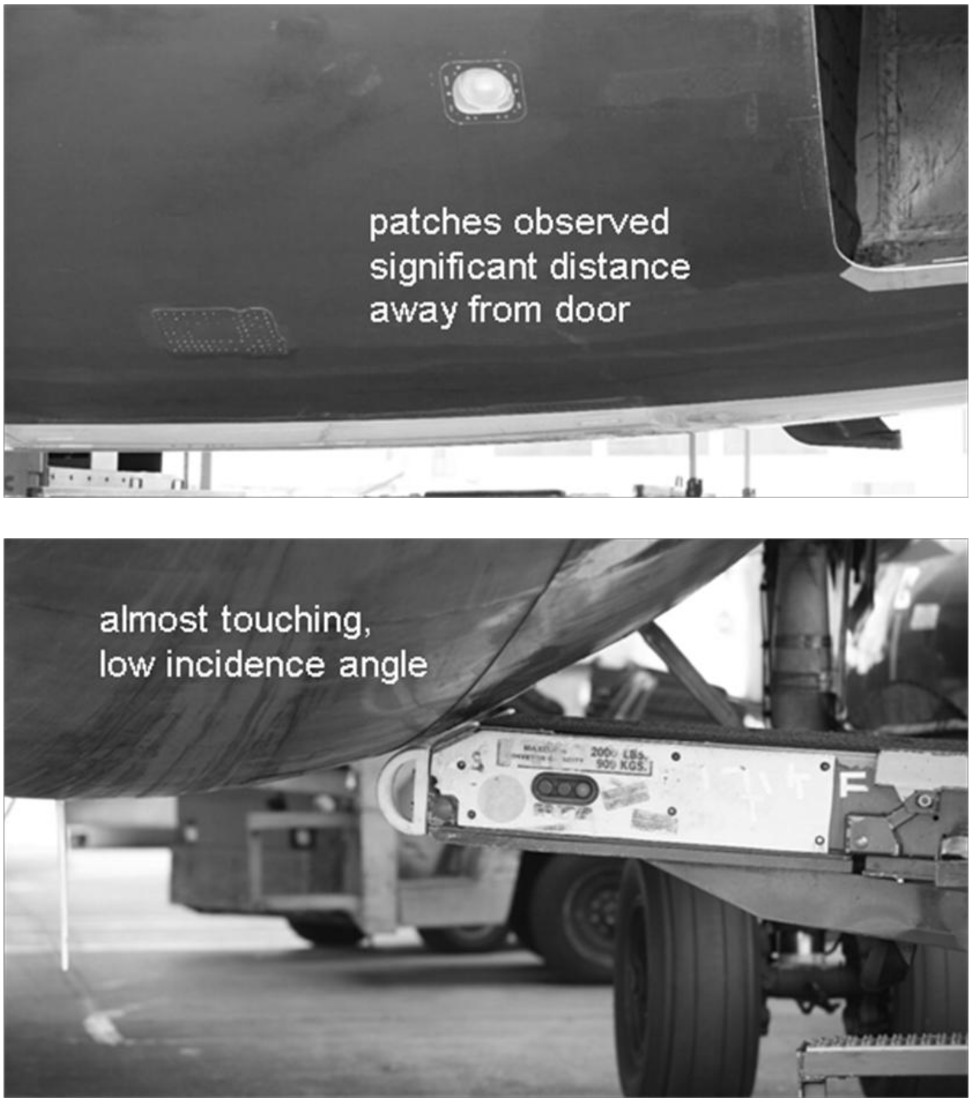

Figure 2. Examples of Damage Occurring in Acreage of Aircraft (i.e., Away from Doors) and Interaction Between Belt-Loader and Fuselage

UCSD Blunt Impact Focus. Blunt impacts can be defined as impact sources that can affect large areas or multiple structural elements, while potentially leaving little or no externally visibly detectable signs of damage. Blunt impacts come from a variety of sources and can involve a wide range of energy levels. UCSD is focused on two major sources that are presently of great interest to industry: ground service equipment (GSE) and large-sized hail ice impacts.

These sources are depicted in Figure 3, showing the portions of the aircraft where such threats typically occur. The side and lower facing surfaces of the aircraft are subject to contact with GSE, whereas all exposed upper and vertical surfaces are subject to ground hail impact (terminal velocity + wind gust) and forward-facing surfaces are subject to in-flight hail impacts. UCSD's activities on these areas are closely tied in with industrial activities and directly addresses aviation industry-driven needs for increased knowledge in these areas from both experimental and analytical/computational viewpoints, ultimately enabling the development of more efficient and safe aircraft structures.

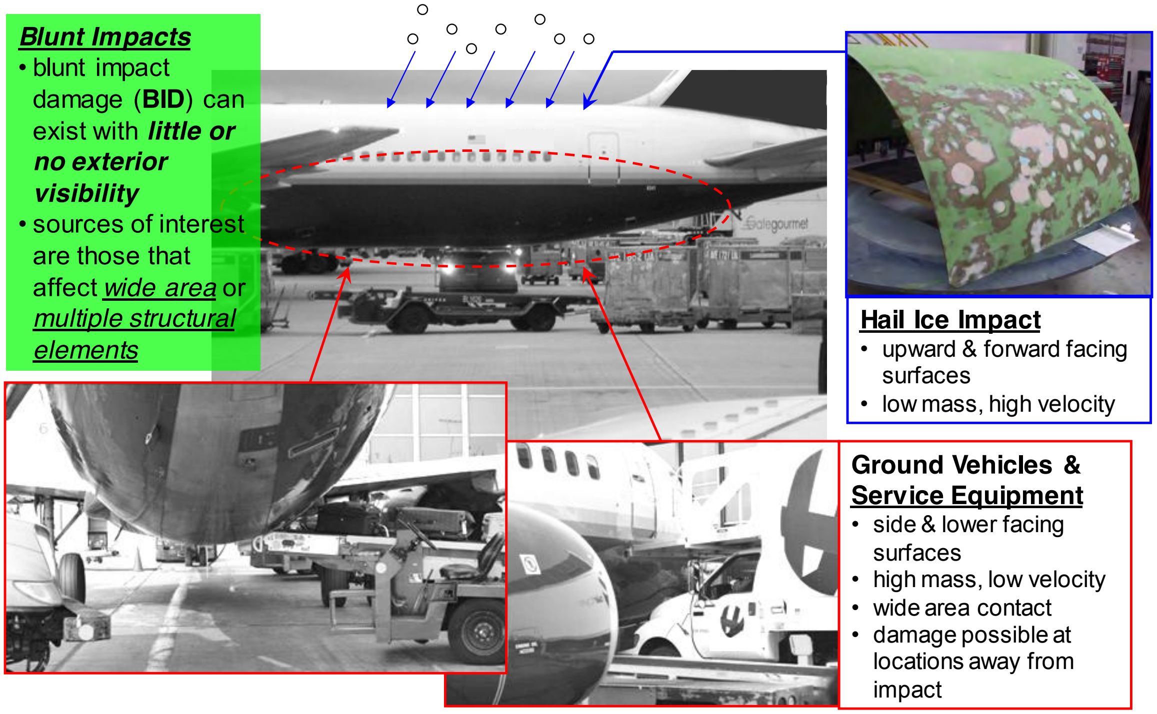

Blunt Impacts
- blunt impact damage (**BID**) can exist with ***little or no exterior visibility***
- sources of interest are those that affect *wide area* or *multiple structural elements*

Hail Ice Impact
- upward & forward facing surfaces
- low mass, high velocity

Ground Vehicles & Service Equipment
- side & lower facing surfaces
- high mass, low velocity
- wide area contact
- damage possible at locations away from impact

Figure 3. UCSD Blunt Impact Focus: Hail Ice and Ground Service Equipment

1.2 Objectives

The objectives of this research project focuses on impact damage formation by a range of sources, including: (i) low velocity wide-area blunt impact –

vehicle/ground maintenance contact with composite aircraft structure, and (ii) high velocity hail impact. Objectives are listed for each area:

Low-Velocity High-Mass Wide-Area Blunt Impact:

1. Identify which blunt impact scenarios are commonly occurring and are of major concern to airline maintenance organizations and aircraft manufacturers.
2. Develop methodology for blunt impact threat characterization and prediction, including sub-structure test methods development to experimentally evaluate blunt impact threats on large panel-sized specimens.
3. Experimental identification of key phenomena and parameters governing high energy blunt impact damage formation, particularly focusing on what conditions relate to the development of massive damage occurring with minimal or no visual detectability on the impact side.
4. Damage tolerance assessment of blunt impact damaged structures with focus on conditions related to loss of limit load capability for level of damage incurred, and which types of structural configurations and details are more prone to this loss of capability.

High Velocity Hail, Bird, and General Impact:

1. Investigate impact damage initiation and damage formation to composite panels, including those of skin-stiffened and sandwich construction.
2. Develop models predicting impact damage to composite panels.
3. Develop unified treatment methodology for predicting damage initiation by variety of impactor projectile types – e.g., bird, hail, tire fragment, runway debris, lost access panel, etc.

1.3 Expected Outcomes

Accomplishment of these objectives are intended to aid maintenance engineers in assessing whether an incident could have caused damage to a structure, and if so, what sort of inspection technique should be applied to resolve the extent of damage. Furthermore, it is expected that design engineers can make use of the research outcomes to: (i) improve the resistance of composite aircraft structures to damage from blunt impacts as well as a variety of other sources such as hail- and bird-strikes, runway debris, lost access panel, etc, and (ii) provide critical information on the mode and extent of seeded damage, particularly those not easily detected by visual inspection, resulting from a wide gamut of impact threats – i.e., low to high velocity.

1.4 Research Partners

UCSD's research on impact of composites is of direct interest to industry. The following Table 1 summarizes the research partners that are actively participating in the project with UCSD. Large and small aircraft manufacturers, a small composites-specialized engineering firm, and a material supplier are represented. Additionally, consultants John Halpin and Jack Bish will lend their expertise to the project in the areas of aircraft damage tolerance (Halpin) and automotive crash safety (Bish) applied to vehicle impacts onto aircraft.

Table 1.Research Team Members

Name of Persons/ Company	Description/ Expertise	Role in UCSD Project
John C. Halpin, Ph.D., JCH Consultants	Consultant on Aircraft Safety and Composites	Advise on direction of project, provide guidance on tests, data reduction, results interpretation and dissemination to the public and senior-level individuals in industry as well as to military (Air Force).
Boeing (David Polland, Al Fawcett, Kevin Davis, Arne Lewis, Nikhil Rao)	OEM – Large Transport Aircraft	Provide guidance and input on both blunt impact and hail ice impact topics. Particular focus on blunt impacts onto panels of stiffened-skin construction. Possibly supply test panels.
Airbus (Michel Mahe, Andre Calligaris)	OEM – Large Transport Aircraft	Provide guidance and input on both blunt impact and hail ice impact topics. Particular focus on glancing blunt impacts onto panels of stiffened-skin construction. Possibly supply test panels.
Bombardier (Isabelle Paris, Rushabh Kothari)	OEM – Small/Regional Aircraft	Provide guidance and input on hail ice impact, particularly focused on sandwich panels. Supply test panels for ice impact.
Bell Helicopter (Constantin Sohn)	OEM – Rotorcraft	Provide guidance and input on hail ice impact, particularly focused on sandwich panels. Supply test panels for ice impact.
San Diego Composites (Dan Jacobson)	Composites Design and Manufacturing	Provide technical advice the direction of the project, guidance on the design of the large-scale blunt impact composite test panels, guidance on the design of tooling for manufacturing the test panels, and access to large autoclave for curing panels.
Cytec (Abdel Abusafieh, Mike Stuart)	Materials Supplier	Provide technical advice on project directions. Provide guidance on use of materials. Supply carbon/epoxy prepreg materials to support fabrication of test specimens at UCSD for both blunt impact and hail ice studies.
United Airlines (Eric Chesmar)	Airline	Provide guidance and feedback on project directions particularly with reference to operator view. Participate in on-site meetings.
Delta Airlines (Ray Kaiser)	Airline	Provide guidance and feedback on project directions particularly with reference to operator view. Participate in on-site meetings.
Sandia National Laboratory (Dennis Roach)	Government Lab	Conduct advanced non destructive investigation (NDI) on impacted test panels to aid in understanding of damage extent developed, and determine detectability of non-visible damage modes.
Jack Bish, Ph.D., Consultant	Automotive Crash Safety and Crashworthiness; Vehicle Crash Testing	Provide information on state of the art practices used by automotive industry to assess and model low-speed vehicle impact scenarios. Guide implementation of codes to model aircraft blunt impacts by ground vehicles. Advise on future planning of tests using real vehicle for “projectile.”

1.5 Summary of Previous Years' Results

The multi-year impact project has been ongoing at UCSD. A summary of previous years' results (work done prior to July 2009) is listed below:

- Conducted surveys to industry querying definitions of blunt impact damage and sources. Observed airport operations at LAX with United Airlines host. Photographs and video records taken and discussions with personnel noted. This activity served to define blunt impactor geometry and threat sources for UCSD experiments.
- Investigated low velocity impact damage to composite panels in lab-scale scenario, using instrumented pendulum impactor – results show dramatic increase in failure threshold energy as function of impactor tip radius and inability to create local damage when rubber pad (represents rubber bumper) was used between impactor and target panel.
- Studied via dynamic finite element simulation the effect of impactor radius on stresses developed in large curved composite panels subject to up to 3 m radius blunt impacts. Also investigated effect of contact angle/ orientation and found impulse to be predicted by trigonometric scaling equations – namely the more shallow angle of contact will transmit higher total impulse to the impacted structure.
- Conducted two industry-agency workshops at UCSD: on January 23, 2009, and on June 30 to July 31, 2009. These focused on the description

of industry experiences in blunt impact damage sources, and the definition and “steering” of UCSD’s composite panel specimens and experiments.

- Defined ice impact test matrix, in collaboration with Sandia Labs, based on Toray T800/3900-2 material system. Acquired and fabricated all test specimens supporting this activity. Roughly ½ of specimens were painted with aerospace-grade white paint coating by professional aviation services shop. These will be used in visual detectability studies.

2.0 Summary of Recent Year Project Results

The results described herein are a summary of the work conducted since the last FAA JAMS review meeting held in July 2009. The project activities are described in two separate subsections. (i) wide area blunt impact, and (ii) hail ice impact.

2.1 Wide Area Blunt Impact Damage

2.1.1 Overview

The primary objective of the Wide Area Blunt Impact Study is to assess the damage resistance, and also the extent of damage formed, of composite structures to impact by wide area blunt sources such as ground vehicles. This includes developing an understanding of failure modes, internal stresses and relationships between loading situations and varying geometric (and stiffness) properties of the indentor. This will be achieved by a combination of experimental observation of the evolution of damage modes (failure history) for a series of large-sized test specimens, the determination of the spatial extent of damage possible within these specimens, and analyses of these tests, which includes validation of finite element models with “rigid” indentors. Specific interest will be to find conditions that directly relate to widespread structural damage with little to no visual detectability. This is especially important for ground service equipment (GSE) with rubber bumper materials which soften the contact-interaction with aircraft structure, in combination with composites which do not dent easily unless subjected to severe concentrated impact forces. Also, a methodology will be established for testing and analysis of blunt impact events, specifically how to properly represent stiffness and mass boundary conditions for substructure testing.

This project’s objectives will be achieved via three major tasks: (i) Task 1. Identification of Common Impact Scenarios. (ii) Task 2. Methodology for Impact Threat Characterization and Prediction. (iii) Task 3. Key Phenomena and Parameters Governing Impact Damage. The overarching framework describing the scope of this project is shown in Figure 4. Several critical components such as threat characterization and modeling are covered by Tasks 1 and 2 which feed into understanding the damage developed by blunt impacts. Task 3 will provide understanding of damage via a series of focused experiments. These all feed into providing the OEMs with design and decision criteria for evaluating occurrences of blunt impact damage, and assessing locations where these events are critical, i.e., “what, when, where, how…”

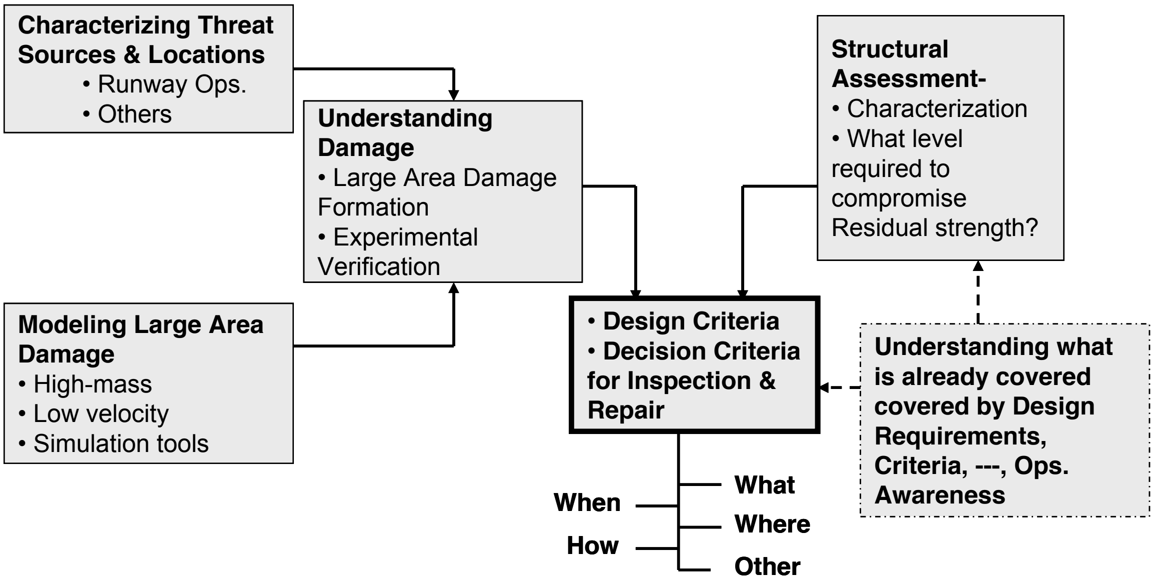

Figure 4. Logic Diagram for Low Velocity High-Mass Wide-Area Blunt Impact

2.1.2 Test Specimen Description

The large-scale blunt impact experimental activities planned at UCSD are to be conducted over multiple phases, as described by the “building block” pyramid shown in Figure 5. The first phase of activity will focus on establishing a basic understanding of key failure modes, how these are excited in relationship to bluntness parameters and incidence angle of the impact, and the establishment of a “clean” database measuring structural response and failure development. In addition to assessing the mechanisms of how blunt impact damage forms, these data will be critical to the development of modeling methodology and simulation tools for predicting damage. Following phases II and III involve larger-sized test specimens (and accompanying models) and will account for dynamic effects, geometry scaling, and ever-important boundary condition effects. At each level, high fidelity finite element modeling and correlation will used to establish damage prediction capability.

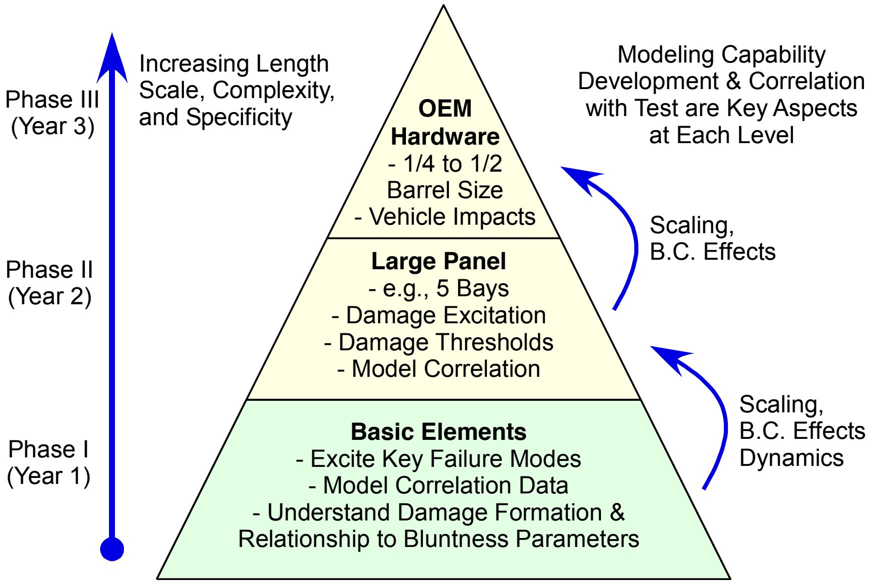

Figure 5. Blunt Impact Testing Building Block

For Phase I in Figure 5, two types of specimens have been devised with the guidance from industry over the course of two workshops. The first configuration (specimen ID series: FrameXX), shown in Figure 6, is primarily focused on damage development to the circumferential frame members and their connection to the skins. Originally this specimen was to represent a “Steady State” Zone, as depicted in Figure 7, and be “line loaded” and have two frames. However, during the Working Meeting on-site at UCSD held on June 30 to July 1, 2009, it was agreed, based on input from Boeing and Airbus, that the critical location was where the indentor terminates due to biaxial bending that develops at that location. This is the Transition Zone condition indicated in Figure 7. A third frame was therefore added to the UCSD FrameXX specimens, and the end of the long indentor will terminate directly under the center frame (see Figures 6 and 7).

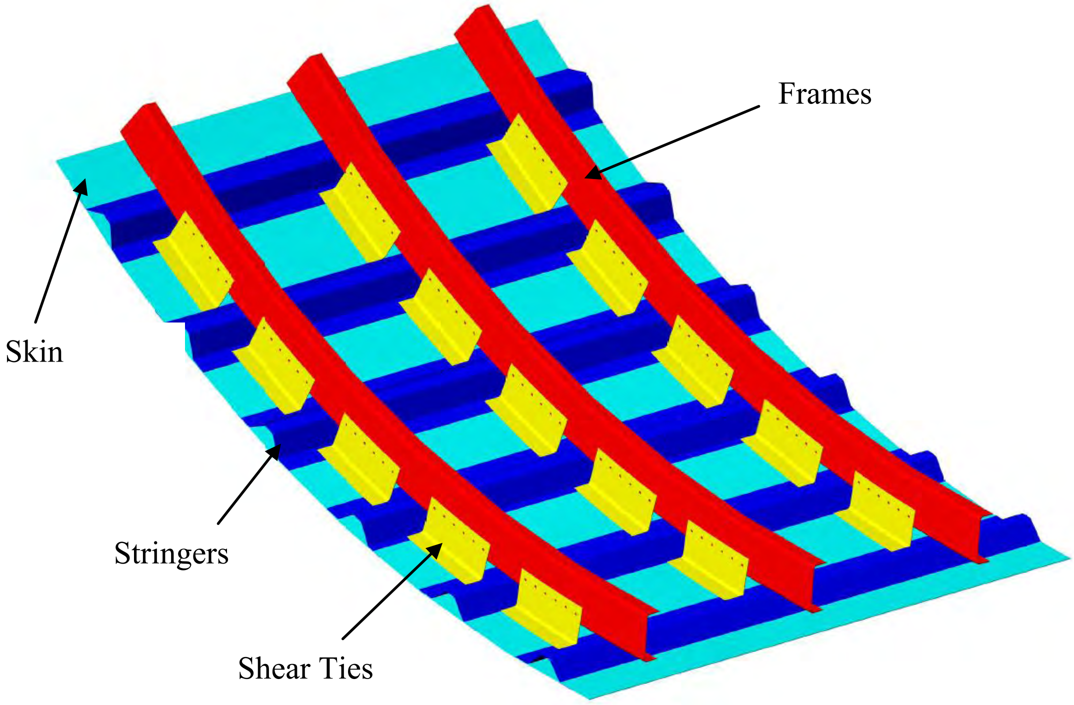

Figure 6. Frame Focused Test Specimen (Series ID: FrameXX)

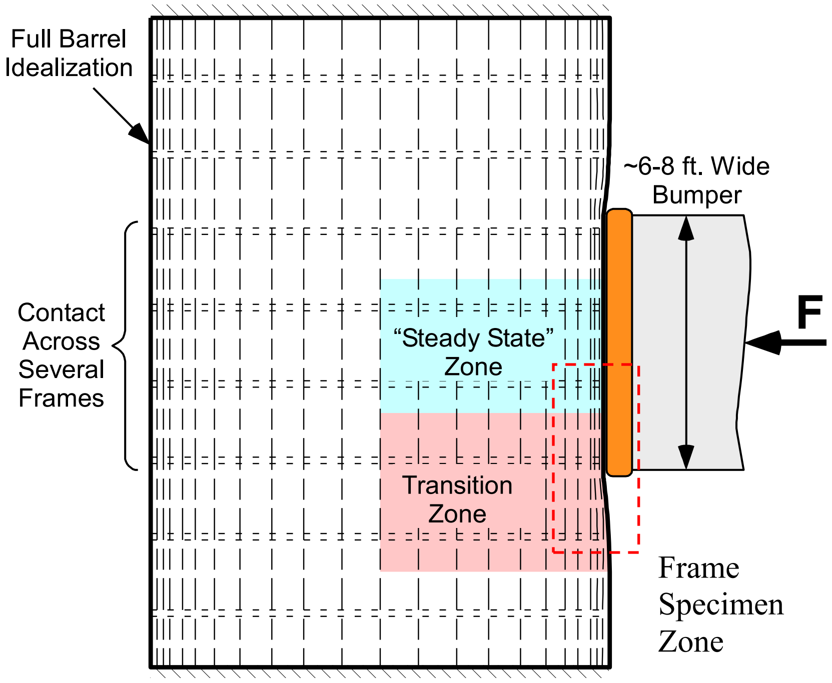

Figure 7. Deformation Zones for GSE Bumper Impact onto Full Barrel

The second configuration, shown in Figure 8, is focused on damage formation to the stringers and their connection to the skins, i.e., representing localized (not "line load") impacts occurring between frames.

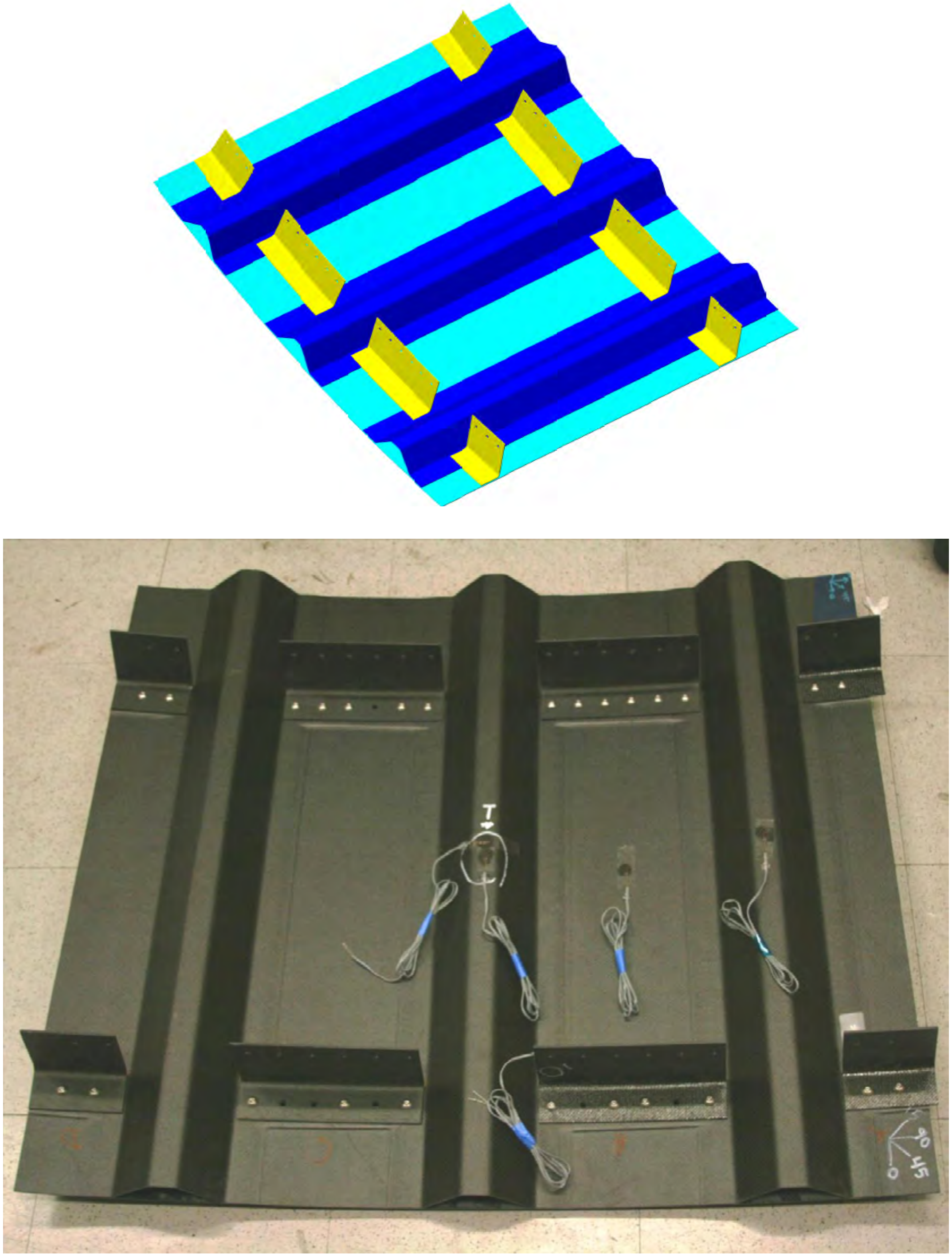

Figure 8. Stringer Focused Test Specimen (Series ID: StringerXX)

The test matrix indicating the number of specimens and testing conditions for both specimen types is shown in Table 2. The impact locations for each of the conditions are depicted in Figures 9 and 10. Photographs of the "rigid" indentors are shown in Figure 11 and the rubber bumper in Figure 12. This is an OEM belt loader bumper purchased from TUG.

Table 2. Wide Area Blunt Impact Test Matrix

	Specimen ID	**Indentor**		
		Rigid 12"R	**Rigid 3"R**	**Bumper**
Stringer Specimens (See Figure 8)	Stringer00		L1-F	
	Stringer01		L3-F	
	Stringer02			L3-F
	Stringer03	L3-F		
	Stringer04	L1-F		
	Stringer05			L1-F
	Stringer06	L2	L2	

	Specimen ID	**Indentor**	
		Rigid 3"R	**Bumper**
Frame Specimens (See Figure 1G)	Frame01	L1	L1-F
	Frame02	L2	L2-F

Notes:

1. "LX" indicates indentation locations 1, 2 or 3. Refer to Figures 9 and 10 for test locations.
2. "F" indicates testing to failure.
3. Stringer06 will be tested on one stringer until initial failure (small damage) with the 3 in. radius indentor, then shifted to test to failure under the other stringer with the 12 in. radius indentor.

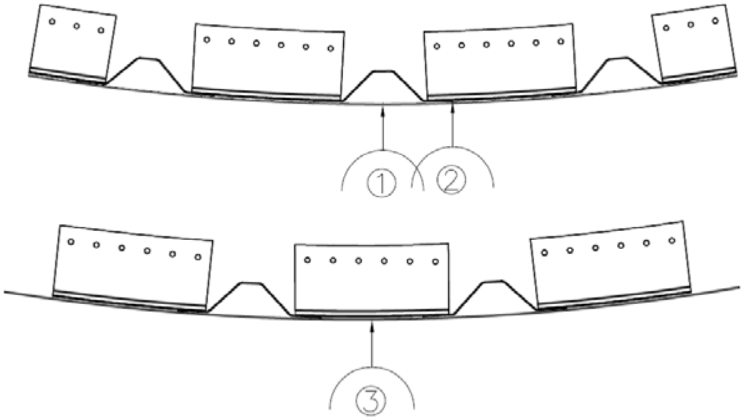

Figure 9. Stringer Impact Locations

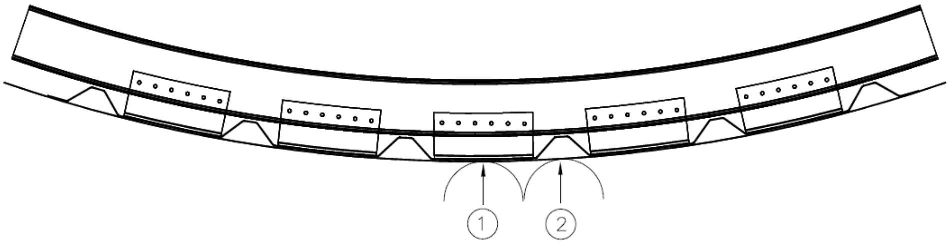

Figure 10. Frame Specimen Impact Locations.

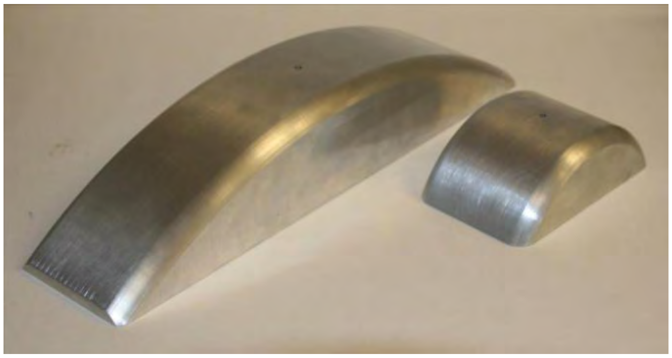

Figure 11: 12 in. and 3 in. Radius “Rigid” Indentors for Stringer Specimen Tests

Figure 12: OEM Rubber Bumper for Stringer Specimen Tests

Influence of To-Date Results on Test Matrix. After having completed testing of stringer specimens Stringer00, 01, and 02, it was observed (confirmed) that the bumper was the critical case, creating significant internal damage (e.g., extensive stringer delamination from skin) that is not visible on the indentation side. The 3 in. radius indentor created a localized, visible damage at Locations 1 and 3 (see Figure 9), so the remaining tests will focus on the damage caused by “blunter” 12 in. radius indentor and the rubber bumper, as reflected by the test matrix conditions for specimens Stringer03 to 06 (see Table 1G). Additional results are provided in detail in the results Section 2.1.5 of this paper.

The frame specimens will have two locations of indentation (see Figure 10): location 1 is expected to be a direct load path to the internal structure, while location 2 is expected to be more compliant. The indentors to be used with the frame specimen simulate a line load and are shown in Figures 13 and 14. The 3 in. radius “rigid” indentor will be fabricated from solid aluminum alloy and will be used to gather elastic-response (no damage) for model correlation. The final failure modes will be developed using the rubber bumper (see Figure 14), which is the experimental condition of interest defined during the UCSD Working Meeting on June 30 to July 1, 2009.

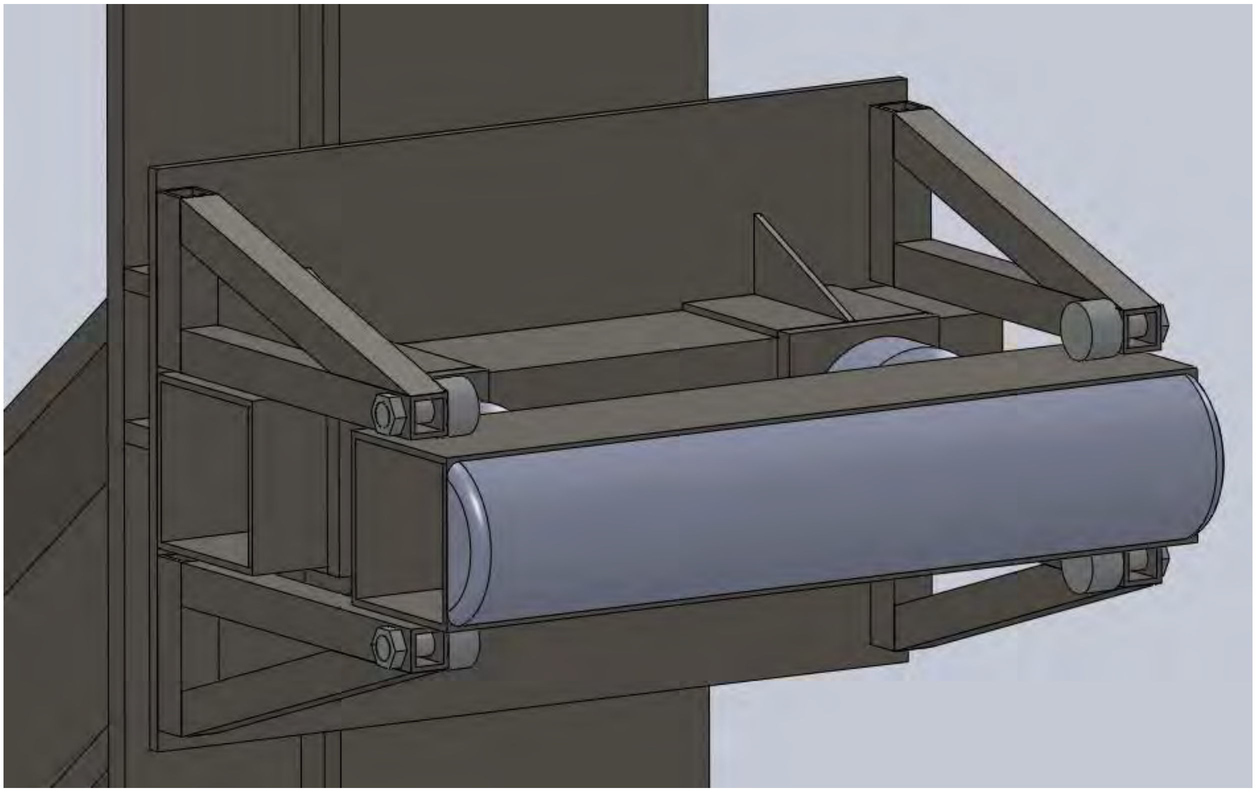

Figure 13: 3 in. Radius “Rigid” Indentor for Frame Specimen Tests

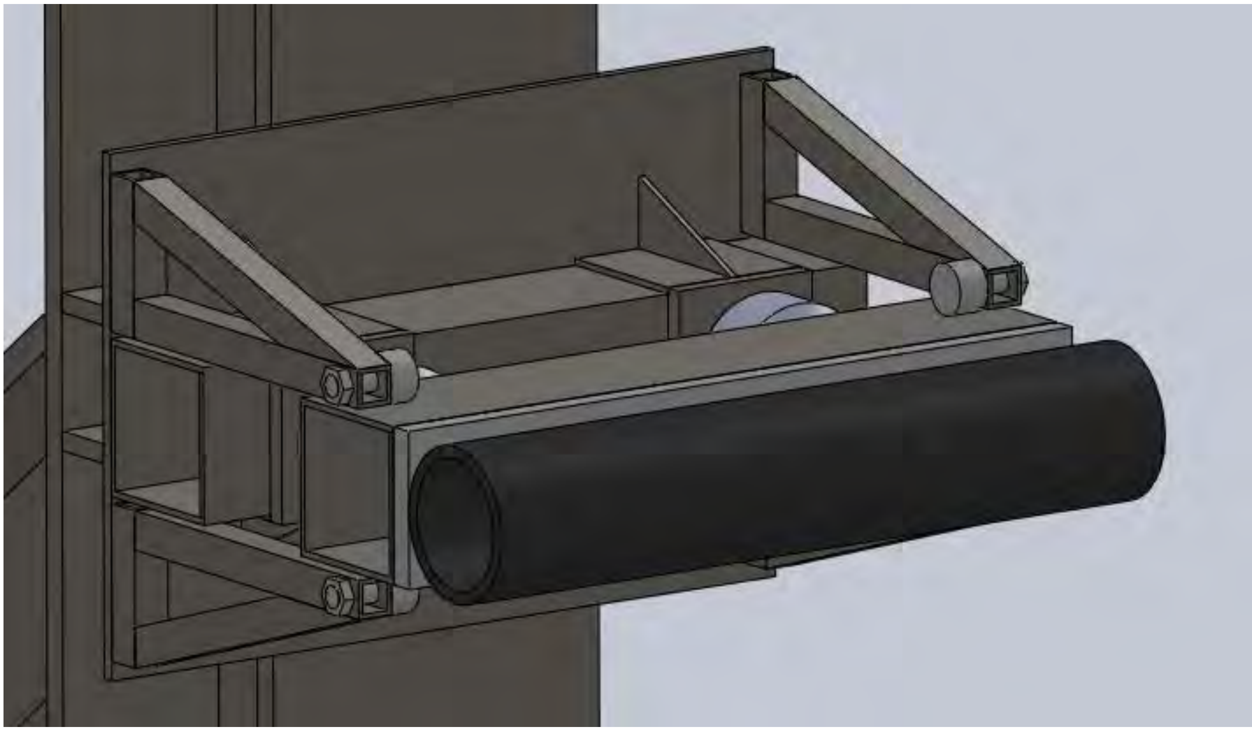

Figure 14: Rubber Bumper for Frame Specimens Tests

2.1.3 Test Specimen Details

Manufacturing

All the test specimens are being fabricated by UCSD in conjunction with UCSD's industrial research partner San Diego Composites. This includes specimen design, tooling design and manufacture, fabrication and evaluation of trial parts, and fabrication of the specimens themselves. A documentation system of material out time tracking and ply layup tables with check-off sheets was used to control quality of parts production. These documents are all archived in case questionable failures occur tied to suspicion of some mistakes in layup. Specimen materials are carbon fiber and toughened epoxy matrix (reflecting current aerospace fuselage materials) provided by UCSD's industrial partner Cytec Engineered Materials. Specifically these materials are X840 unidirectional tape, and X840 3k and X840 6k woven fabrics.

For both stringer and frame specimens, the stringers and shims (spacers to ensure a constant thickness to bolt shear ties to skin) are co-cured to the skin. Layup for all parts is done by hand at UCSD then transported to San Diego Composites to cure. The cure cycle is as follows:

1. Apply 22 In Hg vacuum
2. Apply 85-100 psi, do not vent vac
3. Heat-up to 355F +/- 10F at 1-5F/min
4. Hold 120-180 minutes at 355F +/- 10F
5. Cool to <140F at 5F/min max

Figure 15 shows the 6-ft diameter autoclave (at San Diego Composites) with the specimens loaded in prior to cure.

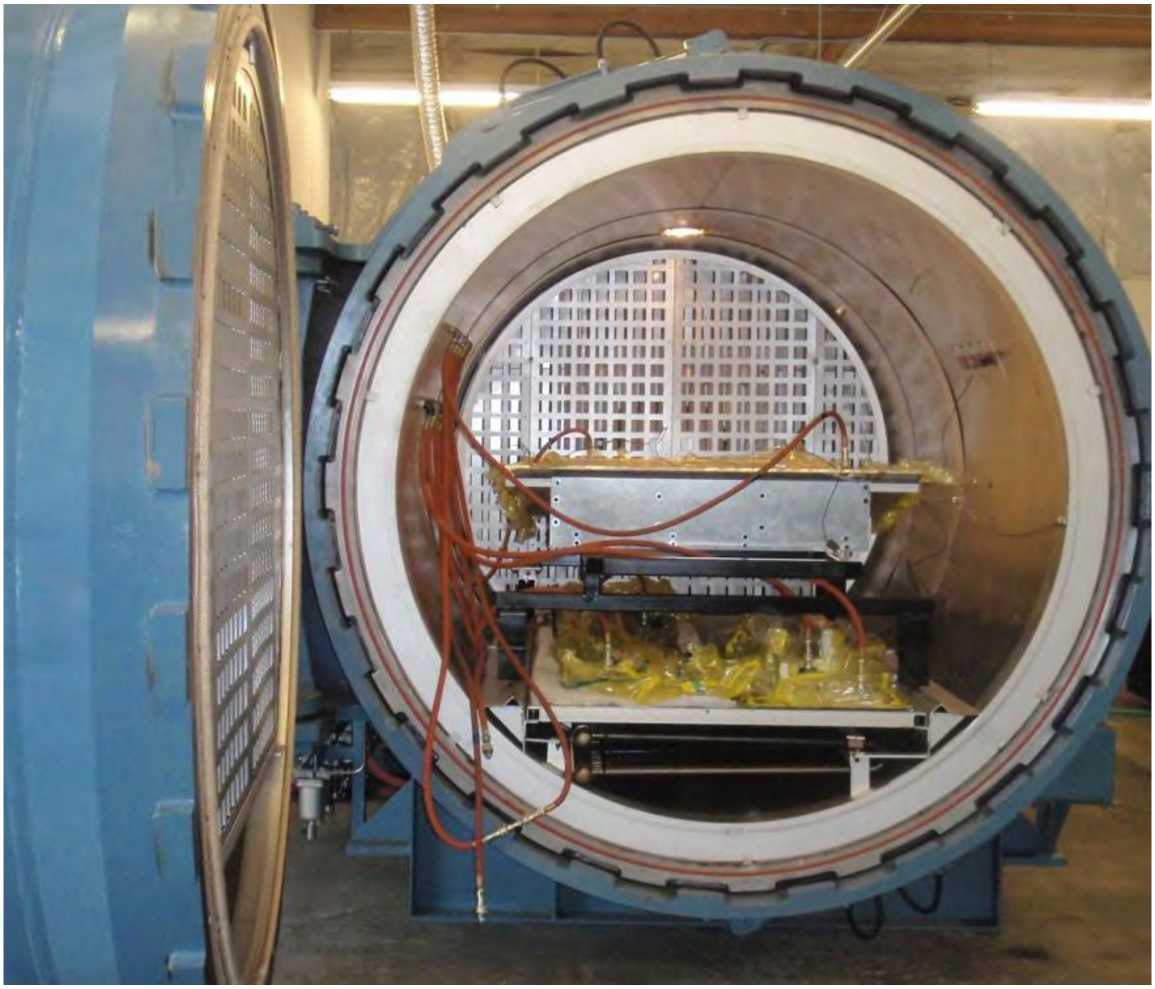

Figure 15. 6 ft. Diameter Autoclave at San Diego Composites

The skin layup is $[0/45/90/-45]_{2s}$ with 0/90 fabric on each side, and the stringers are $[0/45/-45/90/45/-45/0]_s$. The frames and shear ties are all-fabric for increased drapability into compound curved regions of the tools. The shear ties have a layup sequence of $[\pm 45/0\text{-}90]_{3s}$ and the frames have the same layup sequence, with an additional two 0/90 layers in the caps for increased bending rigidity. The shear ties and frames are a bolted assembly using HiLok fasteners. Finished parts are shown in Figures 16 through 18.

Figure 16: Finished Stringer Specimen

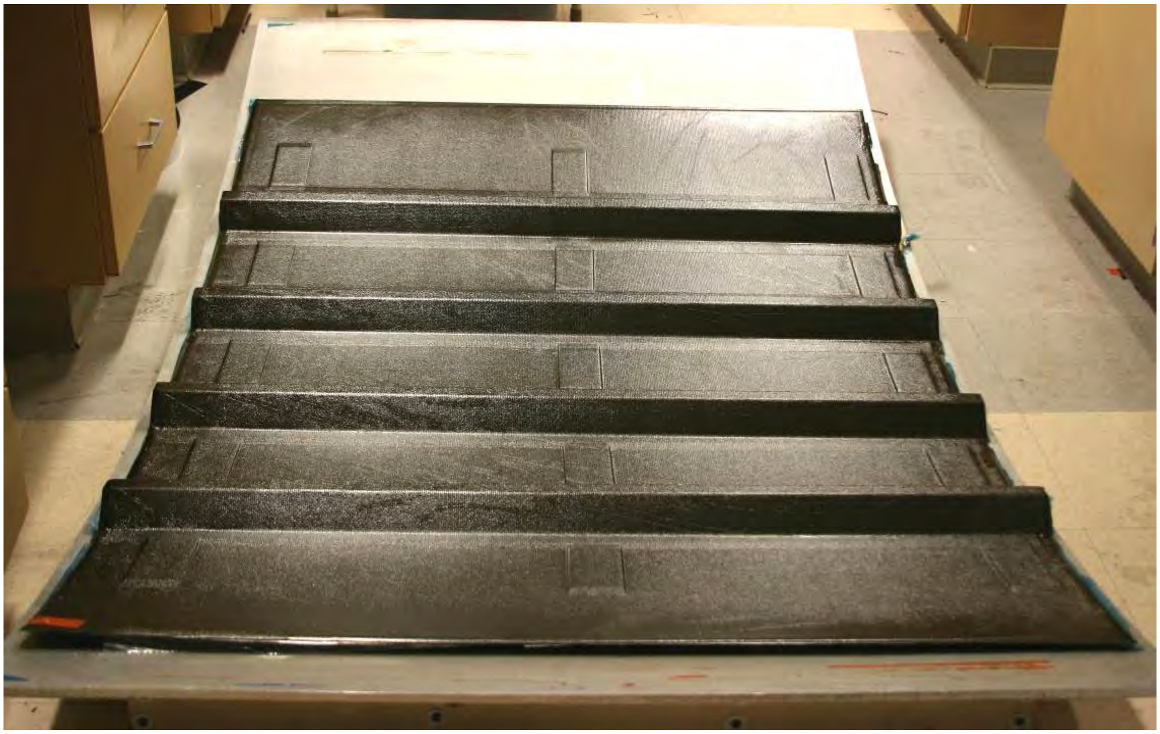

Figure 17: Frame Specimen Without Frames or Shearties; Approximate Overall Dimensions are 6 x 4 ft.

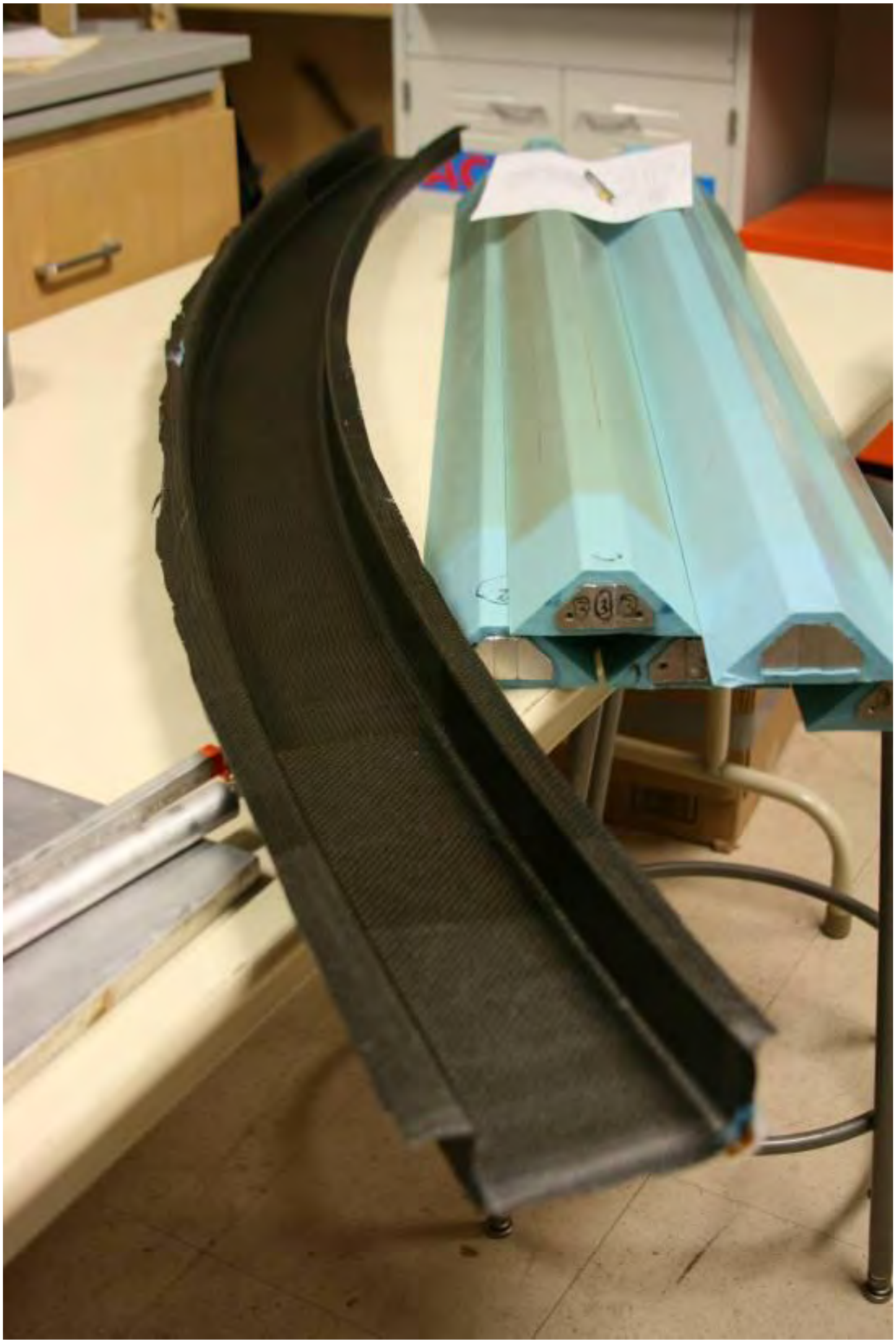

Figure 18: Untrimmed C-Channel Frame; Stringer Internal Silicone Molds

A critical detail is the stringer-to-skin corner detail. Manufacturing trial studies were used to determine the best way to control this geometry and insure that defined radius is maintained in this location, and that the geometry is consistently produced for each specimen in all stringers. This is important since one of the key failure modes is delamination of the stringer flanges from the panel skin. The corner detail geometry is shown in Figure 19.

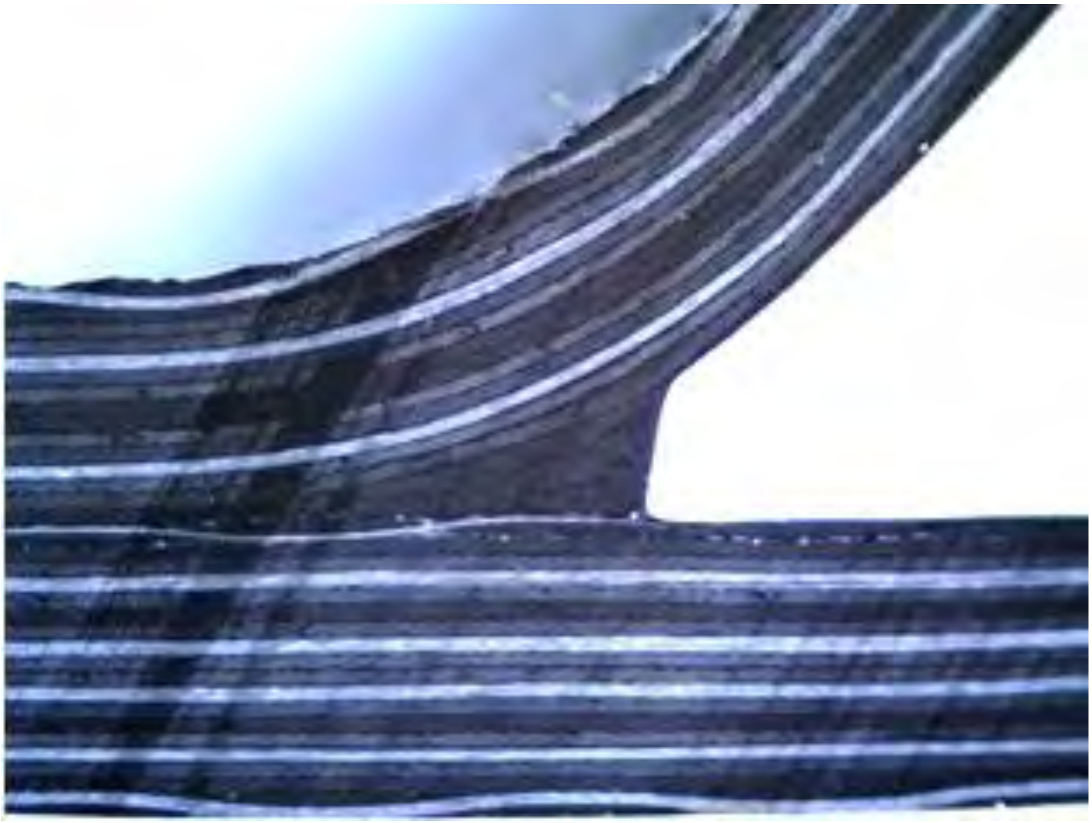

Figure 19. Corner Detail of Stringer-to-Skin Connection

Manufacturing Challenges. It should be noted that the manufacturing activity has been greatly challenging, with many setbacks in tooling acquisition (supplier manufacturing errors), as well as the large number of person-hours of labor required to cut plies and conduct layup for each specimen. This component of the project has delayed the expected rate of testing progress that was expected in this project. The benefit, however, is that the specimen, being 100% designed and manufactured by UCSD, has no associated restrictions affecting the public dissemination of the test results.

2.1.4 Boundary Conditions

Stringer Specimens

The Stringer specimens are tested in the Powell Structural Research Lab at UCSD using a 600 kip SAETEC uniaxial tension/compression test machine. The shearties are bolted to heavy L-angle steel fixtures that have been waterjetted to the same dimensions and curvature as the frame. The L-angles are then bolted to the SAETEC machine table. The typical test setup for the stringer specimen is shown in Figures 20 and 21.

Frame Specimens

The boundary conditions for the frame specimens are critical to ensure that the specimen response replicates the behavior of a full barrel. Because of the low speeds of the ground service equipment represented by these experiments, a pseudo quasi-static response will be excited in the panel structure, and therefore boundary conditions play an important role in the specimen response. Boundary conditions must therefore be carefully designed so as to allow correlation of data from a substructure panel specimen to the full barrel.

Figure 20: Specimen Stringer02 test setup in SAETEC Machine

Figure 21. Specimen Side View of Stringer02 Under Compression Loading

To ensure proper boundary conditions of the frame specimens, spring stiffness will be implemented in the hoop direction K_H (i.e., direction tangential to panel surface) and the boundary support rotational degree of freedom K_θ of the test specimens (see Figure 22).

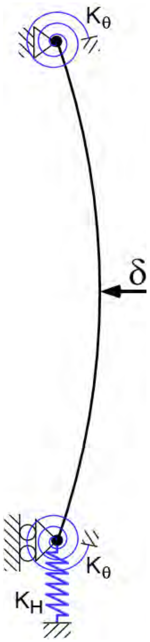

Figure 22. Hoop and Rotational Degree of Freedom Stiffness at Boundaries

The determination of the appropriate value of spring stiffness is achieved via a set of finite element models: one of the full barrel (see Figure 23), and one of the Frame test specimen. Using indentor displacement δ as the common “loading” metric for comparison between the frame specimen and the full barrel models, an iterative process is used to determine the correct spring stiffness needed in the frame specimen boundaries such that boundary displacements are equivalent. The comparison metrics between the full barrel model and the frame specimen are described in Figures 23 through 26. Mainly hoop-direction and rotation displacements must be made to match up between the frame specimen and the full barrel. Doing so would achieve equivalence, thereby making results measured from the frame specimen applicable to the full barrel. The displacements and rotations will be matched based on data from the second frame in the full barrel model and the outside frame (fully under indentor) of the frame specimen (see “frame of interest” in Figures 24 and 26).

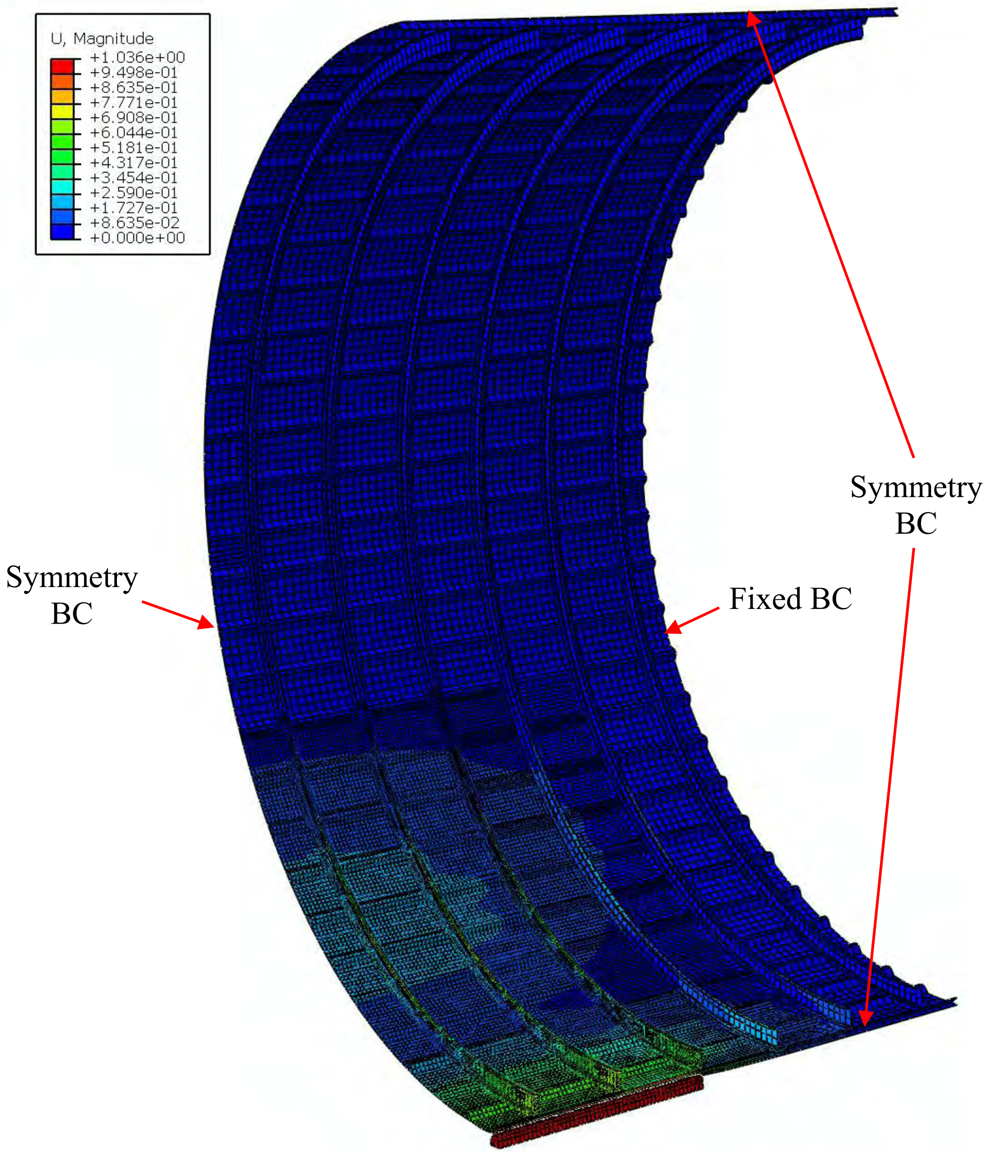

Figure 23. Full Barrel Quarter Symmetric Model with Equivalent Elastic Constants, 3 in. Radius Indentor; Model Represents a Full Barrel With Fixed Outer Boundaries – Only ¼ of Geometry is Modeled Due to Quarter Symmetry

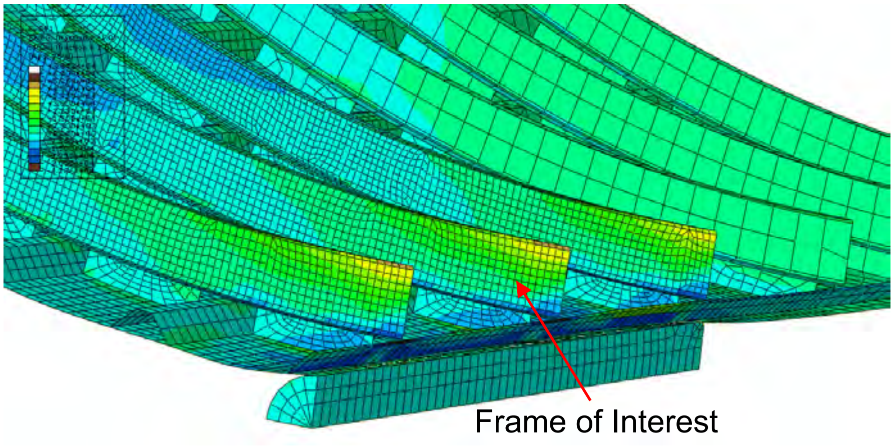

Figure 24. Full Barrel Quarter Symmetric Model Representing a 3 in. Radius Indentor with Equivalent Composite Properties

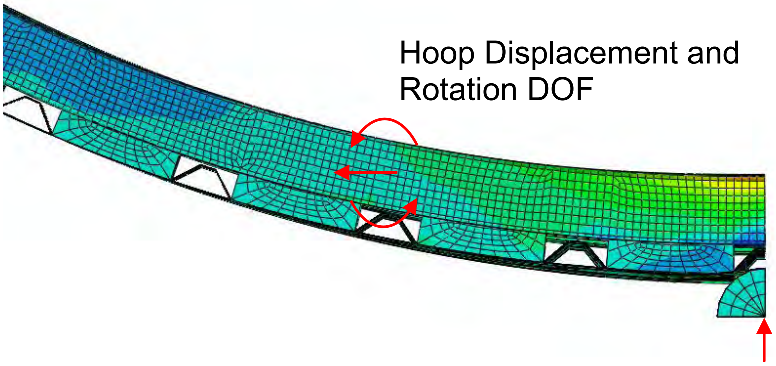

Figure 25. Side View of Full Barrel Quarter Symmetric Model. Parameters of interest to be compared between full barrel finite element model and frame specimen: indentor displacement, hoop displacement of the frame, and rotation of the frame

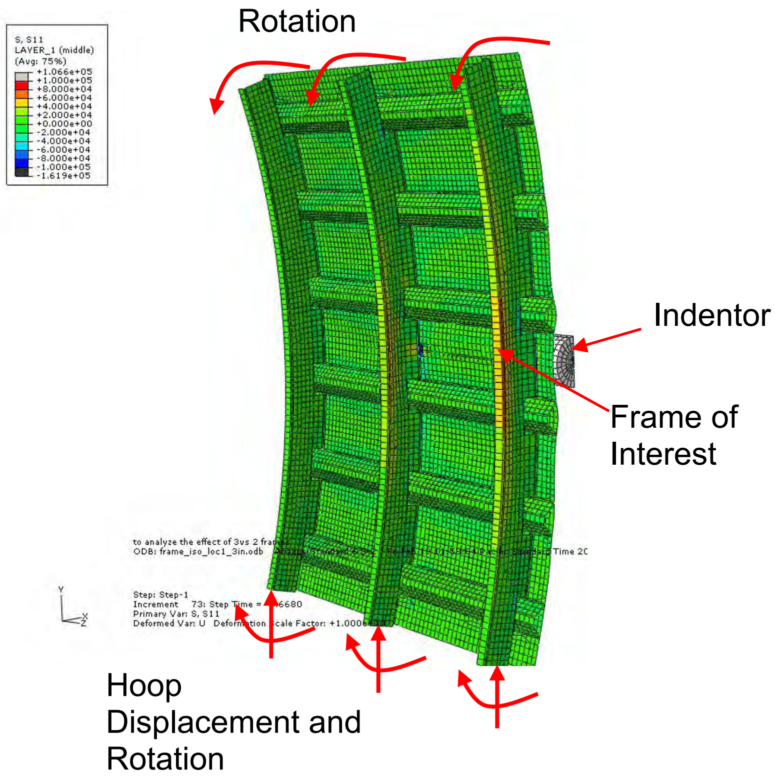

Figure 26. Frame Specimen with Applied Spring Properties at Boundary Conditions Found from the Quarter-Symmetric Model

Figures 27 and 28 show model predictions of the frame hoop displacement and rotation as a function of applied indentor displacement. It can be seen that the frame specimen, in the absence of any boundary spring stiffness, exhibits much larger displacement and rotation than the full-barrel model. This is due to the frame specimen behaving essentially like a simply-supported panel with no in-plane displacement constraint at the boundaries (i.e., K_H and K_θ are zero in Figure 22). The resulting bending moment distribution across the span of the panel will inherently be different than in the full barrel model case in the absence of the spring stiffness, and therefore the proper representations of these boundary stiffness values is of critical importance in order to obtain equivalence.

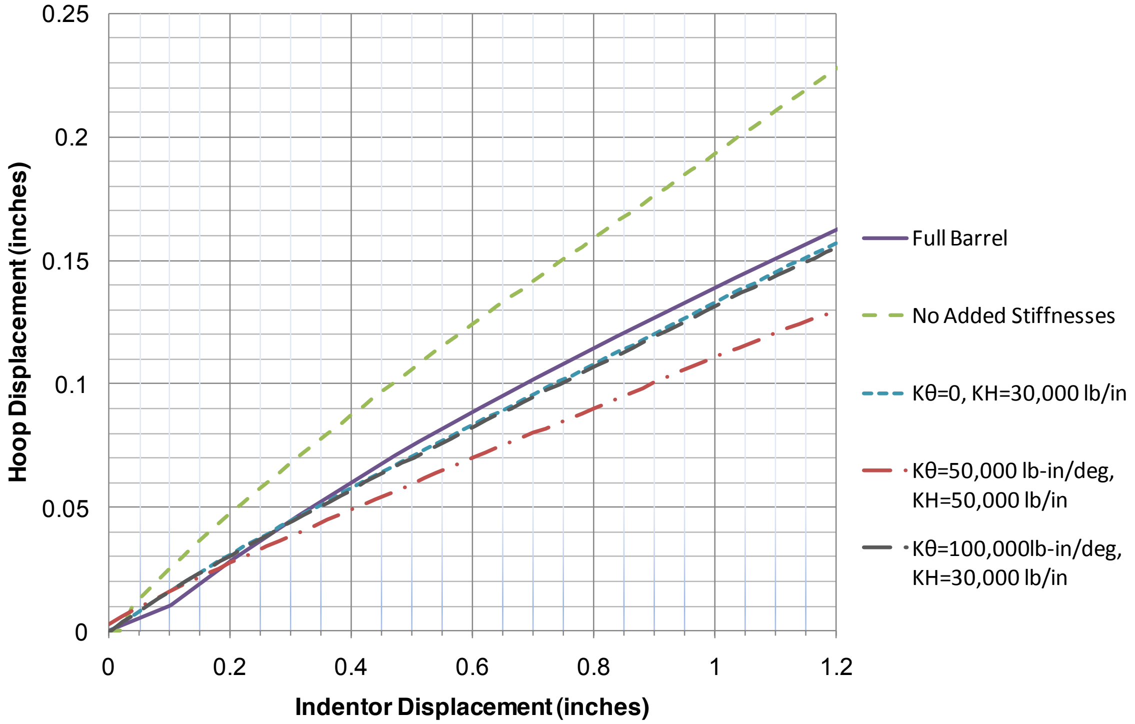

Figure 27. Hoop Displacement for Various Translational Stiffnesses of Frame Specimen and Full Barrel Model

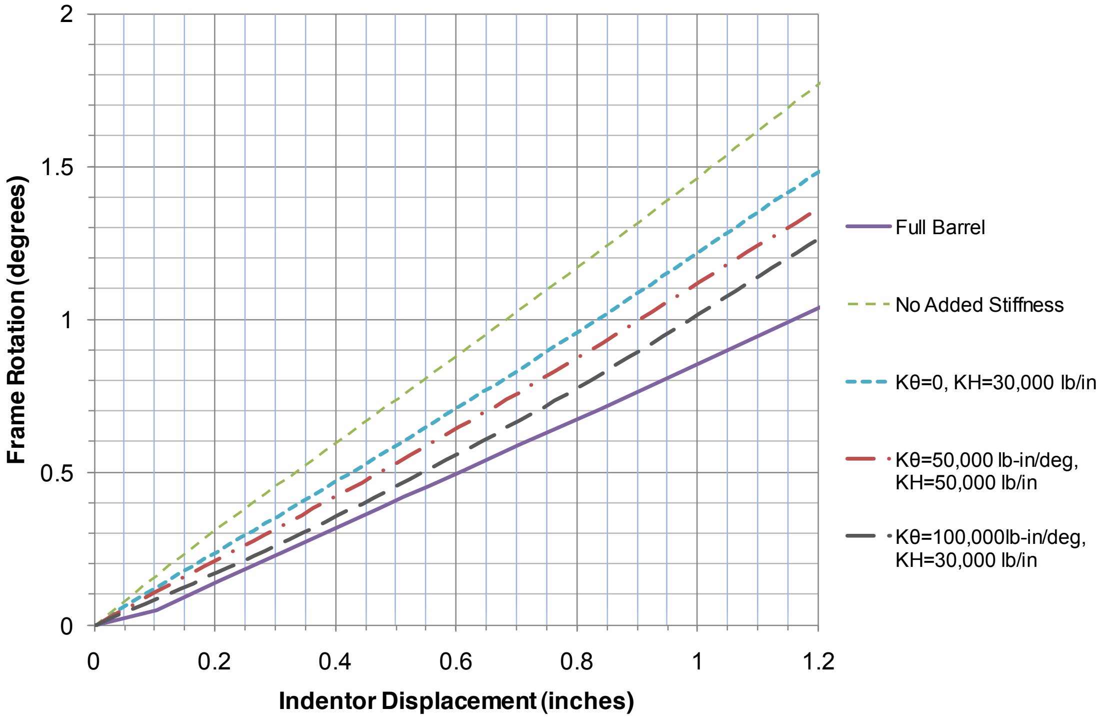

Figure 28. Rotation at Support Location Due to Indentation at Frame of Interest for Both the Frame Specimen and Full Barrel Model

Using an iterative approach to determine the spring stiffness values, Figure 27 shows that an initial choice of hoop spring stiffness K_H of 50,000 lb/in was too high since the hoop displacements are predicted to be lower in comparison to the full barrel displacements. Iterating further, an assumed hoop stiffness K_H of 30,000 lb/in is found to closely match the hoop displacements of the full barrel model. The boundary rotations in both the frame specimen and the full barrel model are shown in Figure 28. In this figure it can be seen that an assumed rotational stiffness value of K_θ = 100,000 in-lb/deg together with hoop stiffness of K_H = 30,000 lb/in yields rotational displacements to match closely with the full barrel model. Another iteration, with increased value of rotational stiffness K_θ must be explored, but has not been completed by the time of this paper's writing. Finally, once the boundary stiffness values have been determined, key stresses within the frame specimen will be compared with the full barrel model to confirm that the stress state generated in the frame specimen model is equivalent to the full barrel. It should be noted that although the indentor displacement is shown out to 1.2 inches, the stiffness of the system is to be determined by the data collected from the first 0.5 in. of indentor displacement (i.e., seek to match initial linear deformation range).

Experimental Setup – Frame Specimens

The frame specimens are to be indented with a 3 in. radius line loading "rigid" indentor as well as a deformable rubber bumper (tube geometry). These are shown in Figures 13 and 14. The indentor heads and supporting fixture assembly are to be mounted on a 1-D shake table in the UCSD Powell Structural Research Lab. In this Phase I of tests, the 1-D shake table will be used in a quasi-static displacement control mode to apply indentation slowly to the specimen, which will be mounted to a reinforced concrete “strong wall” as shown in Figure 29. The advantages of conducting these tests using the 1-D shake table system are: (i) the system is inherently capable of dynamic movement and can be used in Phase II and III studies involving truly dynamic movement of high-mass objects representing GSE, and (ii) the strong wall system is extremely rigid and large sized (30 ft height) permitting “upgrade” to larger specimen sizes, even able to accommodate a complete half-barrel of a wide-body aircraft.

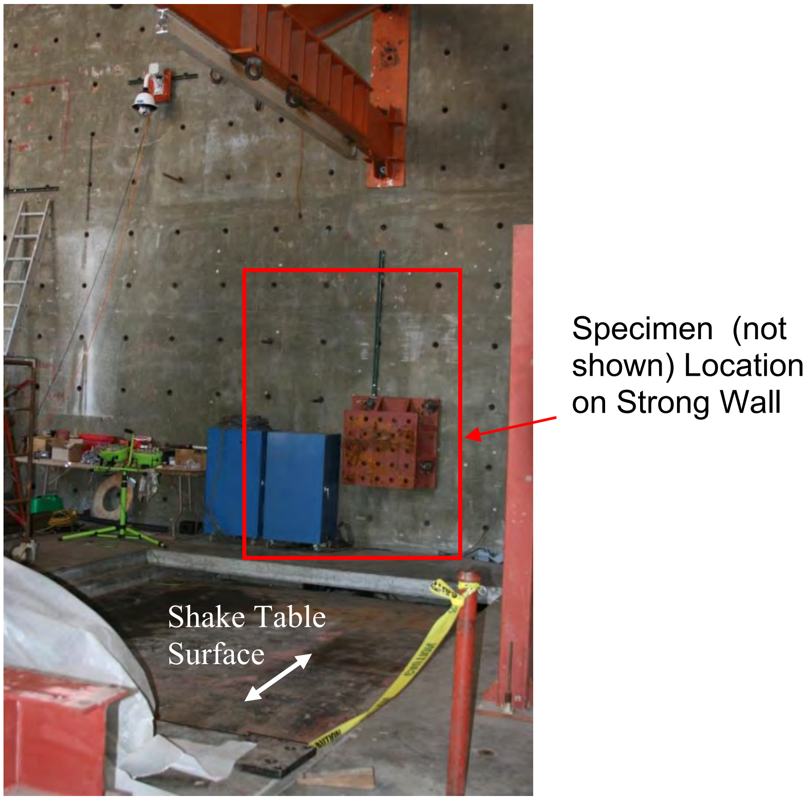

Figure 29. Shake Table and Strong Wall for Frame Specimen Test; Scale Information: Mounting Holes on Wall are 24 in. Apart

As indicated in Figure 29, the test specimen will be vertically mounted and the indentation movement will be horizontal. The planned experimental setup for the frame specimens is shown in Figure 30 (note that only a portion of the strong wall and floor are illustrated here). The specimens will be mounted vertically on the strong wall, with a bearing track (or rollers) at the lower boundary condition to allow hoop-direction translation. Figure 31 shows a top view detail of the setup, and Figure 32 shows detail of the lower boundary condition, with springs used to provide the desired stiffness (i.e., K_H and K_θ), as determined from the finite element models.

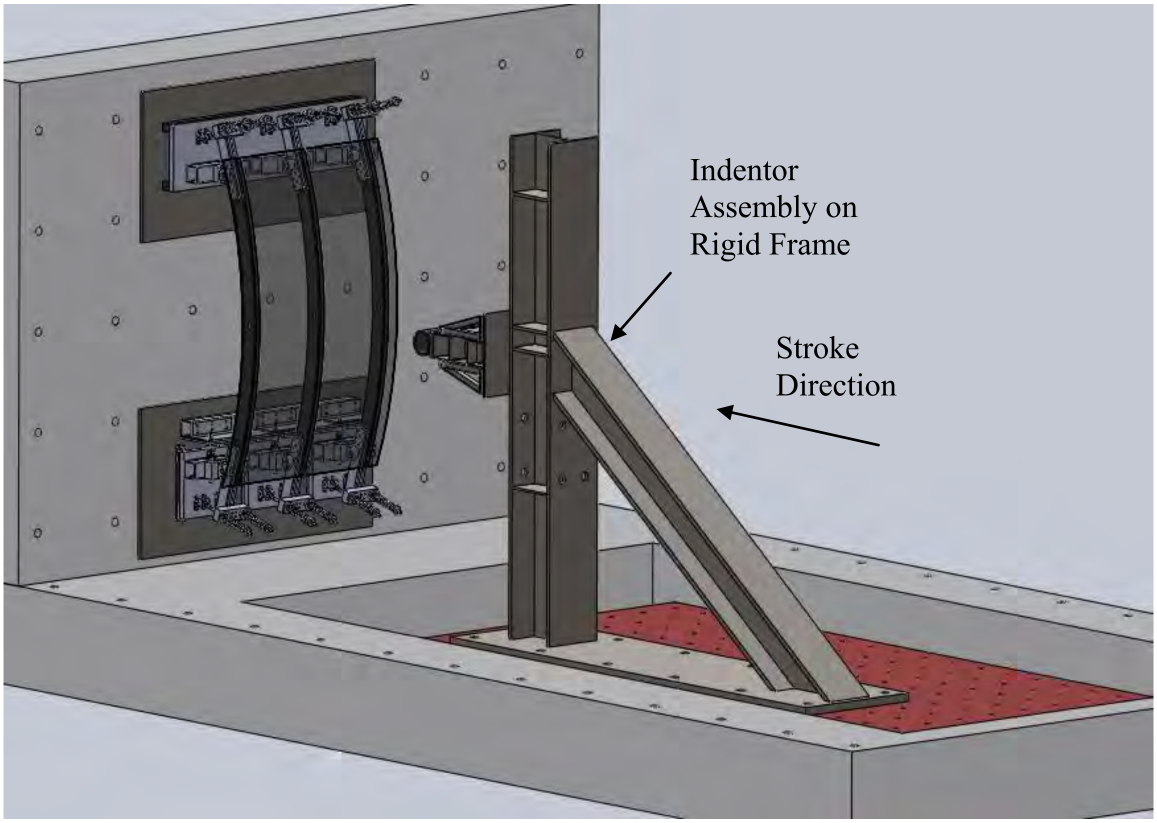

Figure 30. Planned Test Set Up for Frame Specimen on Dynamic 1-D Shake Table to be Run in Displacement Control; Note Entire Strong Wall Not Depicted

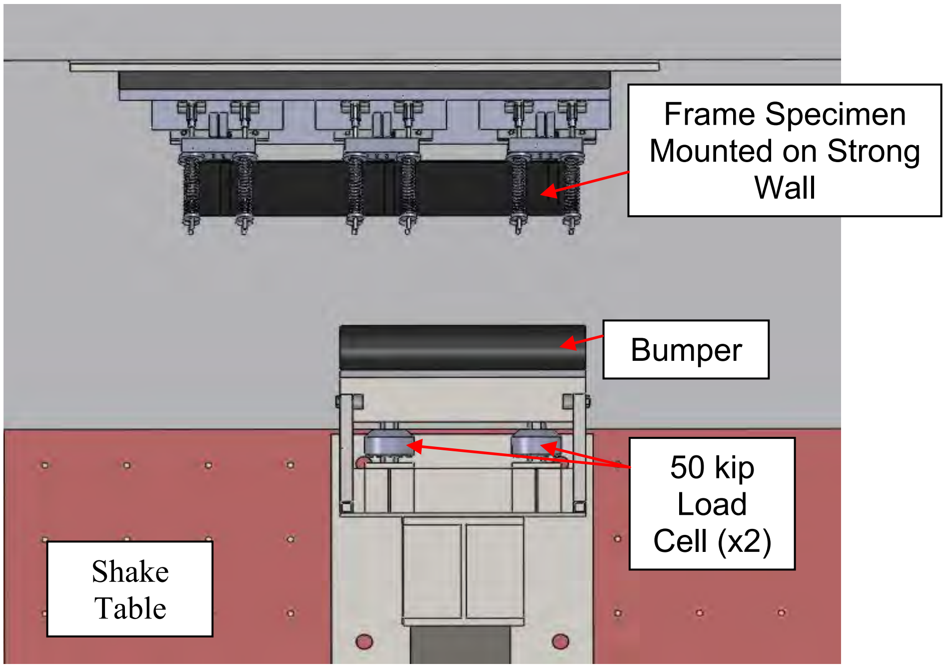

Figure 31. Top View of Experimental Test Setup

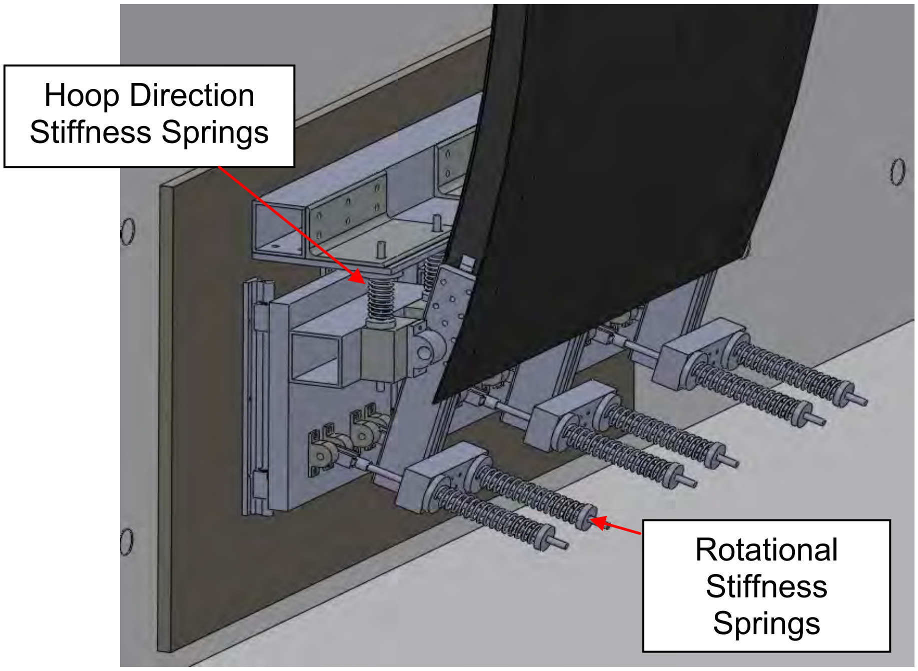

Figure 32. Frame Specimen Connection Detail with Rotational and Translational Stiffness Achieved by Spring Elements

2.1.5 Test Results

To date, three stringer specimens have been tested: Stringer00, Stringer01, and Stringer02. As described in the test matrix in Table 2, specimen Stringer00 is loaded by a 3 in. radius rigid impactor at location 1 directly over the stringer, Stringer01 is loaded by the 3 in. radius rigid impactor at location 3 on the skin between two stringers, and Stringer02 is loaded at location 3 using a rubber bumper. A detailed description of these tests is provided in this section.

2.1.5.1 Specimen Stringer00

1st Loading. Specimen Stringer00 was quasi-statically indented with the 3 in. radius rigid impactor at location 1 (over stringer). During the 1st loading, the panel experienced an initial failure that consisted of a peanut shaped delamination in the skin, directly under the impactor at a load of 2,725 lbs. The resulting peanut shaped delamination was caused by the biaxial bending state from the finite width (3 in.) of the impactor combined with the small radius of the impactor, shown in Figure 33. The delamination was localized to these locations. After initial failure, the test machine was stopped and unloaded, and the panel rebounded to the original undeformed shape with no visible signs of damage from the outer surface, and no observable permanent deformation, as seen in Figure 34.

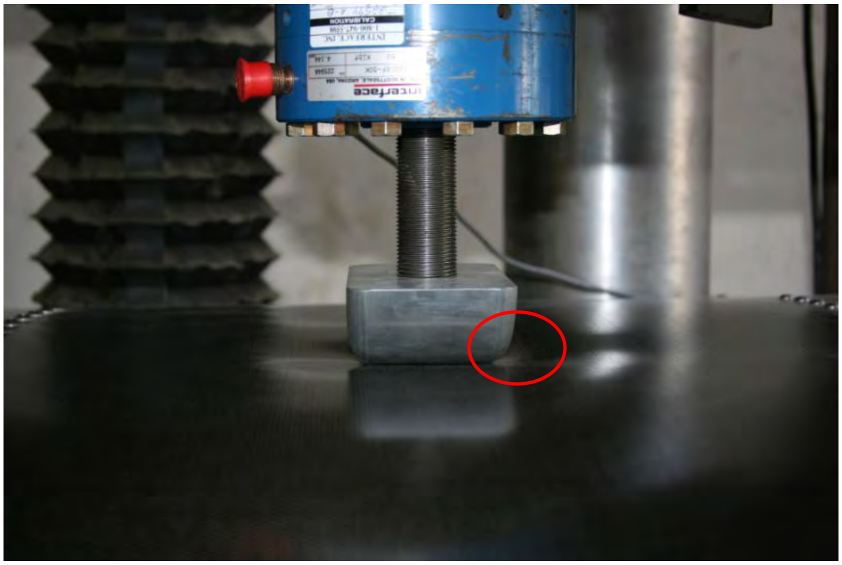

Figure 33. Localized Deformation of Panel Caused by 3 in. Radius Rigid Impactor During 1st Loading of Stringer00. Note Edge of Impactor Causing Biaxial Bending

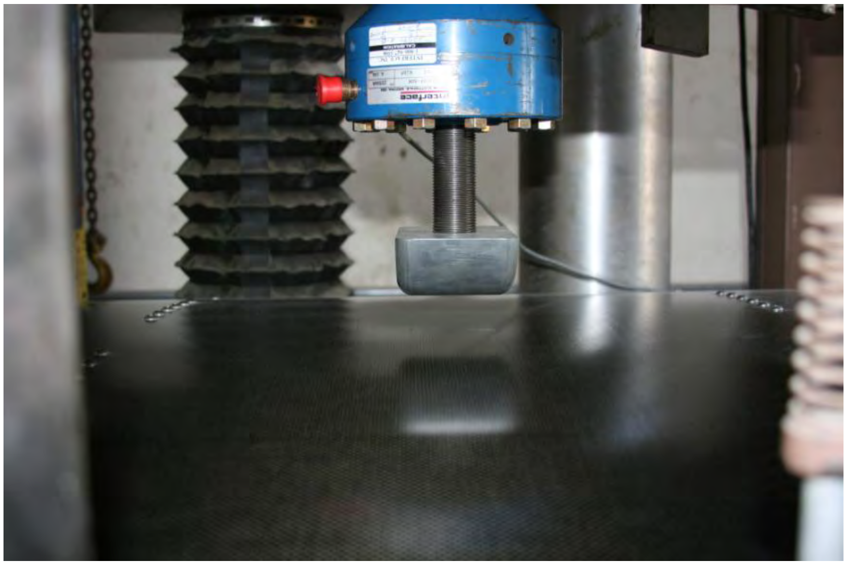

Figure 34. No Visible Permanent Deformation After 1st Loading of Stringer00 Despite Formation of Delamination

2nd Loading. During the second loading, audible crackling sounds began to be detected at approximately 3,000 lbs, indicating further damage occurring, possibly the initial delamination growing in size, or radial delamination developing in the shear ties. At a load of approximately 3,300 lbs, the stiffness of the panel noticeably decreased. This could be caused by compliance in the skin or opening of the shear ties under deformation. Cylindrical-like bending of the panel under high deformation can be seen in Figure 35. Final failure of the panel occurred at 6898 lbs in the mode of penetration through the panel skin (see Figure 36). The penetration damage was a localized failure with no delamination of the stringers detected (between the skin and the stringer flanges). Once completely unloaded, the panel again returned to its overall original shape (see Figure 37) with the exception of the hole produced by the penetration.

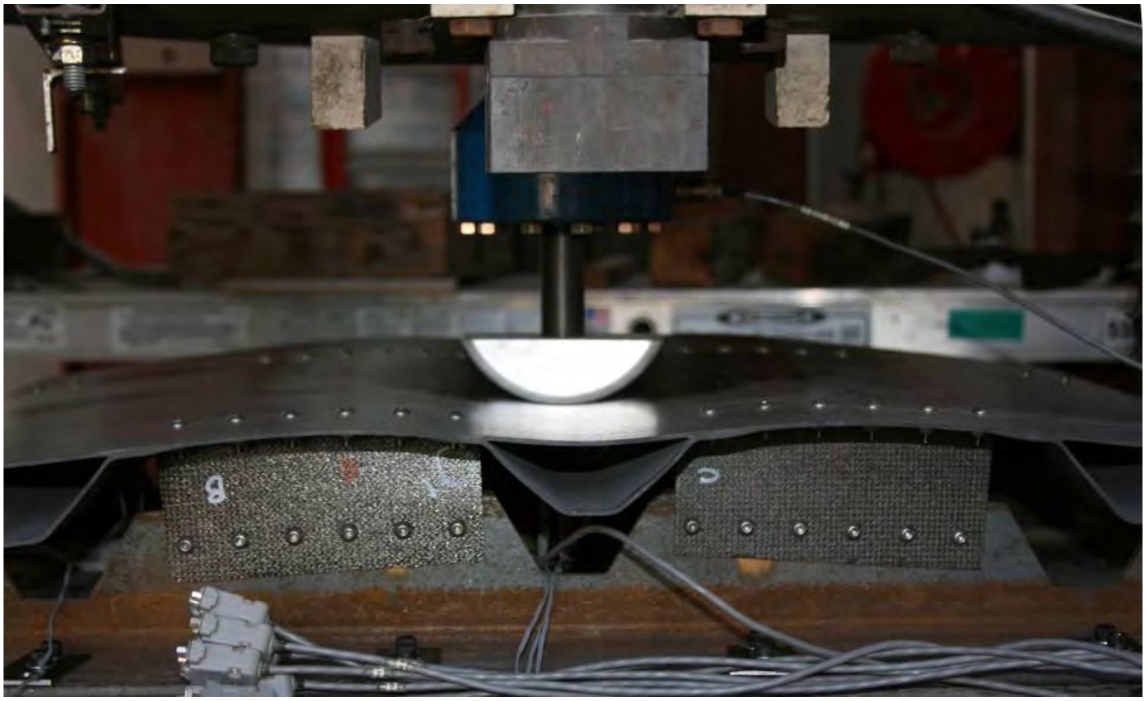

Figure 35. Large Deformation During 2nd Loading of Stringer00

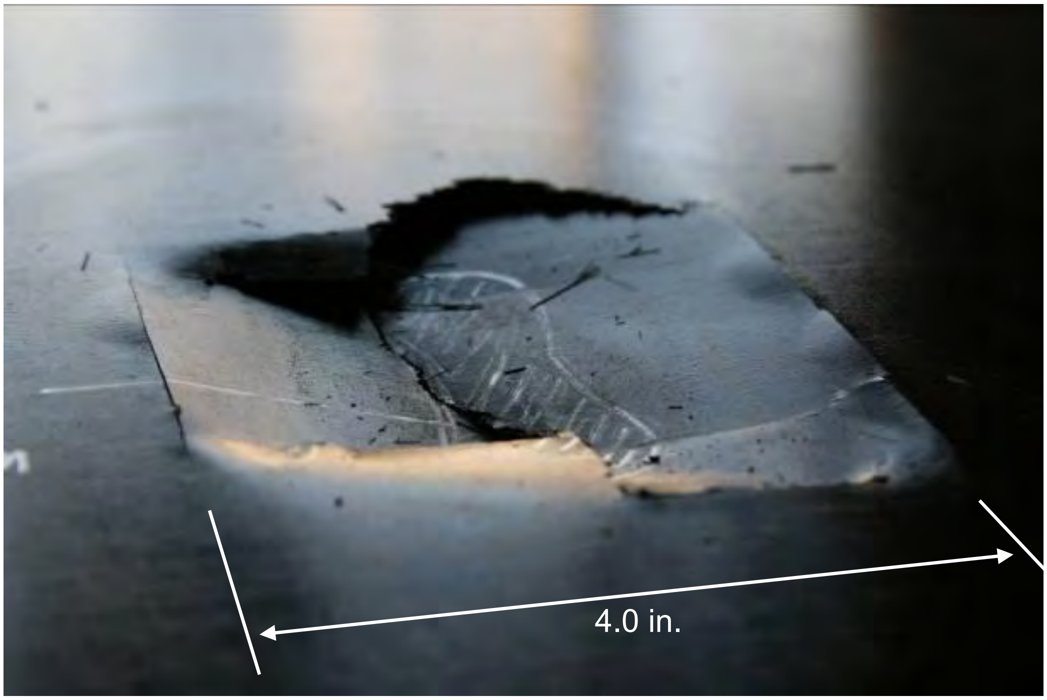

Figure 36. Stringer00 after Final Failure Following 2nd Loading; Initial Peanut Shaped Delamination is Indicated by the Hatch Pattern Zone; Straight Cracks on Left and Right Sides of Photo Spaced at 4 in. Define Stringer Inside Flange Edges

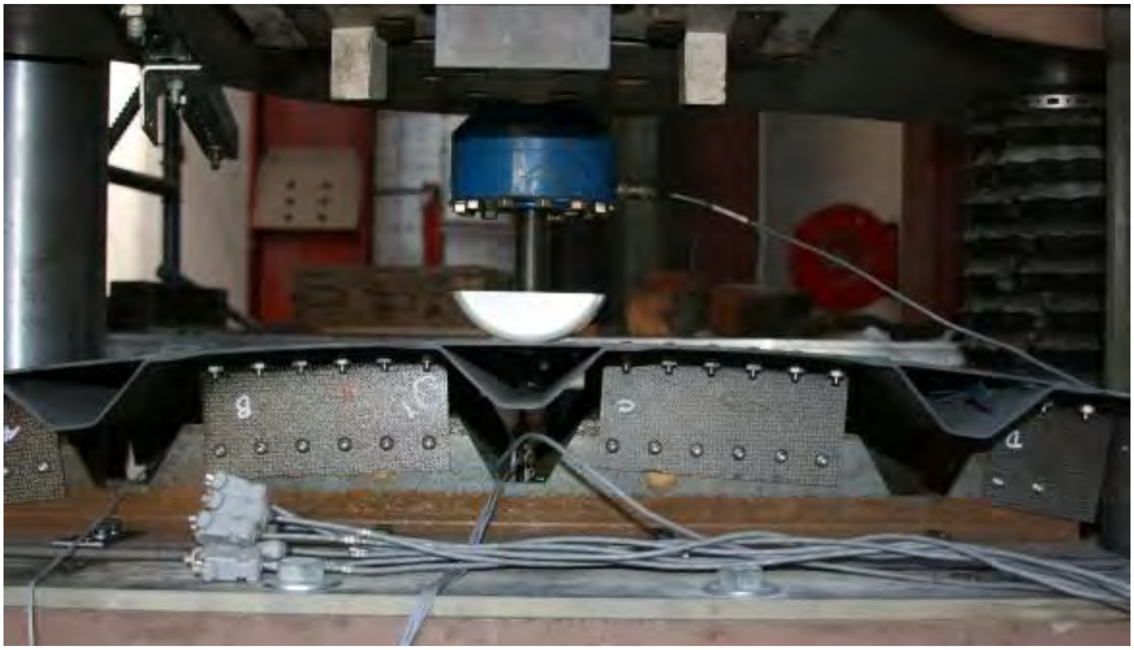

Figure 37. Stringer00 after Final Failure Following 2nd Loading; Panel Rebounds to Original Overall Shape Despite Penetration Damage

Figure 38 shows the force vs. indentation curves for specimen Stringer00. Indentation of the panel was measured by axial displacement of the test machine actuator. The 1st Loading curve shows that the panel initially exhibited a high stiffness before the first failure. However, softening was observed during the 2nd Loading when the load level increased past the point of initial failure observed in the 1st Loading. The walls of the stringer, oriented out-of-plane with respect to the panel skin, provided bending rigidity to the structure. Since the indentation was at the center of the 4.0 in. spacing between the two walls of the stringer, it created a small-span stiff region directly under the impactor, resulting in the high initial portion in the stiffness as seen in Figure 38, until localized delamination softening was observed right under the indentor. Crushing of the shear tie corners closest to the center (directly loaded) stringer was also observed following the 2nd Loading.

Figure 39 shows a time event plot of the different loading sequences applied to specimen Stringer00. Observations during each loading number are noted on the respective loading curve. Audible events such as cracking sounds, distinct popping, and loud (high energy) cracking sounds are noted. These events can be seen to correspond to some inflection in the load vs. displacement curve – a loss of stiffness due to development of damage. Only two loading sequences were applied to Stringer00 before penetration occurred in a sudden manner, following development of local delamination right beneath the indentor. For the 3 in. radius rigid indentor bearing into this short-span space between the two stringer walls, it is expected that high bending stresses develop close to the location of indentor contact.

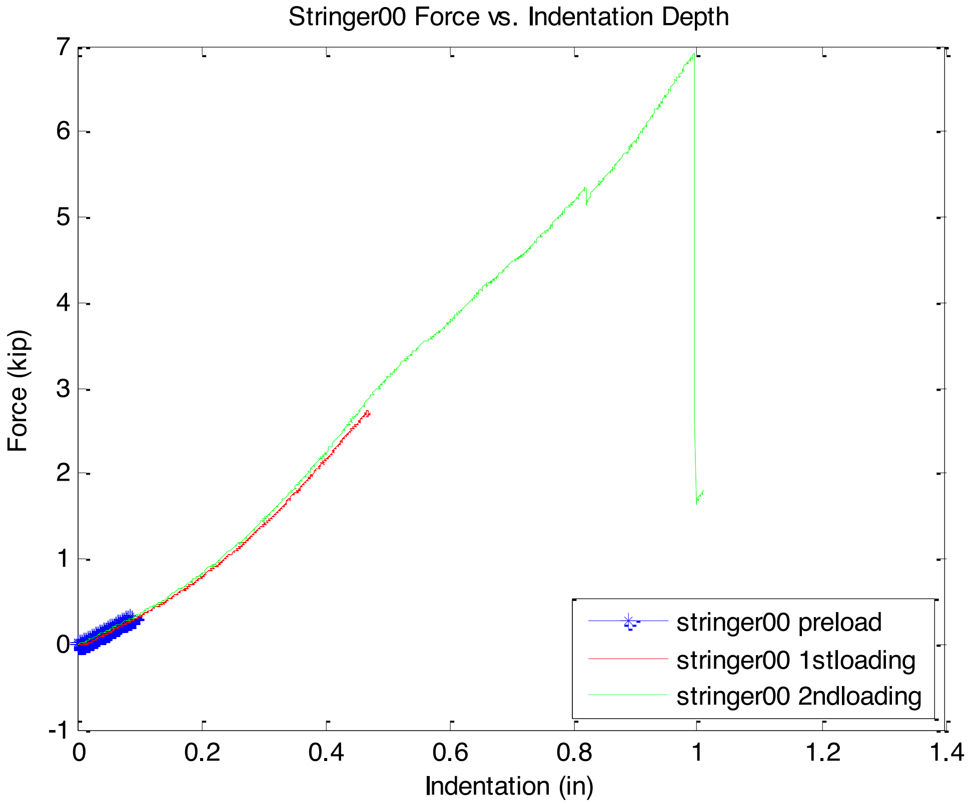

Figure 38: Stringer00 Force vs. Indentation Curves

Figure 39. Stringer00 Time Event Plot

2.1.5.2 Specimen Stringer01

1st and 2nd Loading. Stringer01 was loaded at a location between stringers (see Figures 40 and 41) by the 3 in. radius rigid indentor. While the observation of loud popping sounds defined the end of the 1st Loading, no damage was detectable by visual and A-scan examination. It is surmised that damage might have occurred in the shear tie radius locations, which cannot be inspected by A-scan. Initial (detectable) failure occurred at a load of 2,999 lbs at an indentation displacement of 0.58 in. during the second loading. When the panel was unloaded and inspected by A-scan, two small delaminations in the skin, directly under the impactor edges were observed. Note that this is roughly the same load range at which similarly-located delaminations (under indentor edges) formed in specimen Stringer00.

Figure 40: Panel Rebounded to Original Shape with Localized Damage

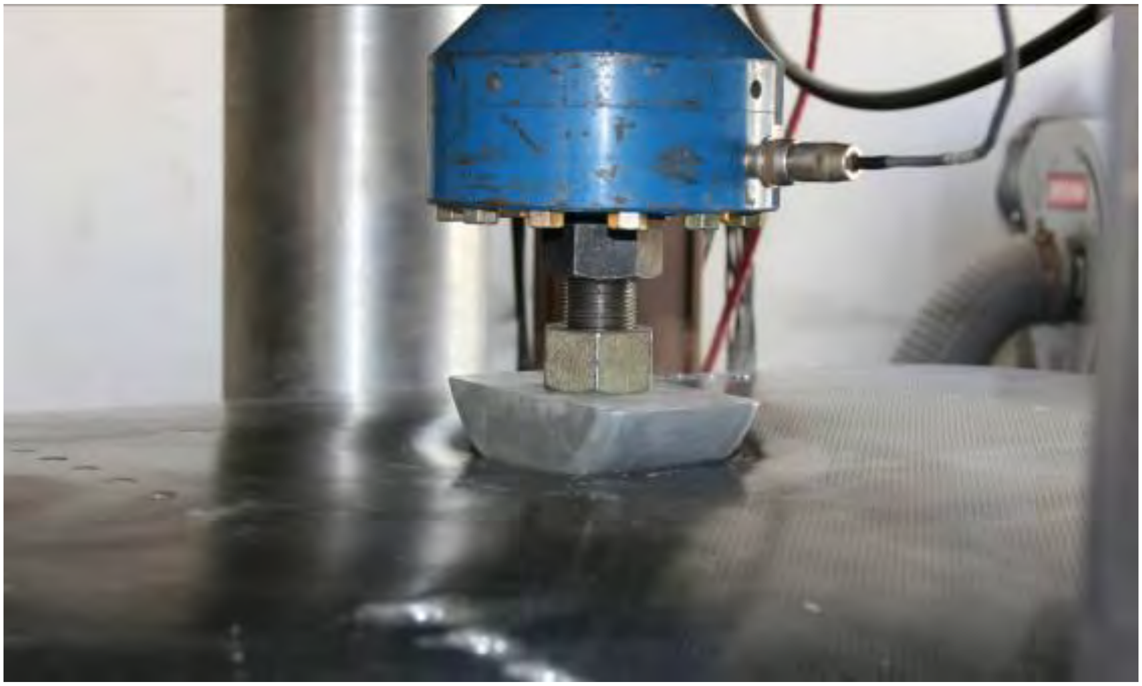

Figure 41: Close-Up View of Penetration of Impactor into Panel

3rd and 4th Loading. During the third loading, small clicking sounds were heard after 3,100 lbs. The test was continued until the next intermediate failure occurred at 5,132 lbs and an indentation displacement of 0.81 in.. A-scan revealed that the delamination under the impactor increased in size. The specimen was then reloaded for a fourth loading, during which a loud crack was heard and slight load drop observed at a load of 6,004 lbs and an indentation displacement of 0.86 in. The machine was stopped and held at a constant actuator position, corresponding to a load of 5,941 lbs, to observe and photograph the damage state. However, the panel could not support this sustained load, and soon after stopping the machine, full penetration of the impactor through the panel skin occurred.

Figure 42 shows the force vs. indentation curves for Stringer01. Indentation of the panel was measured by a linear displacement potentiometer placed on the underside of the panel and directly under the point of indentation. Since the location of indentation was further away from the stringer walls, the panel skin initially deformed more than did Stringer00 (more compliant) under the same load. As large deformations develop and the indentor develops increasing contact area, a more even distribution of the load made it difficult for additional indentation (stiffening). Thus, the curves appear to stiffen with increasing indentation level. A time event plot for specimen Stringer01 is show in Figure 43 together with test observation notes of audible events and major failures.

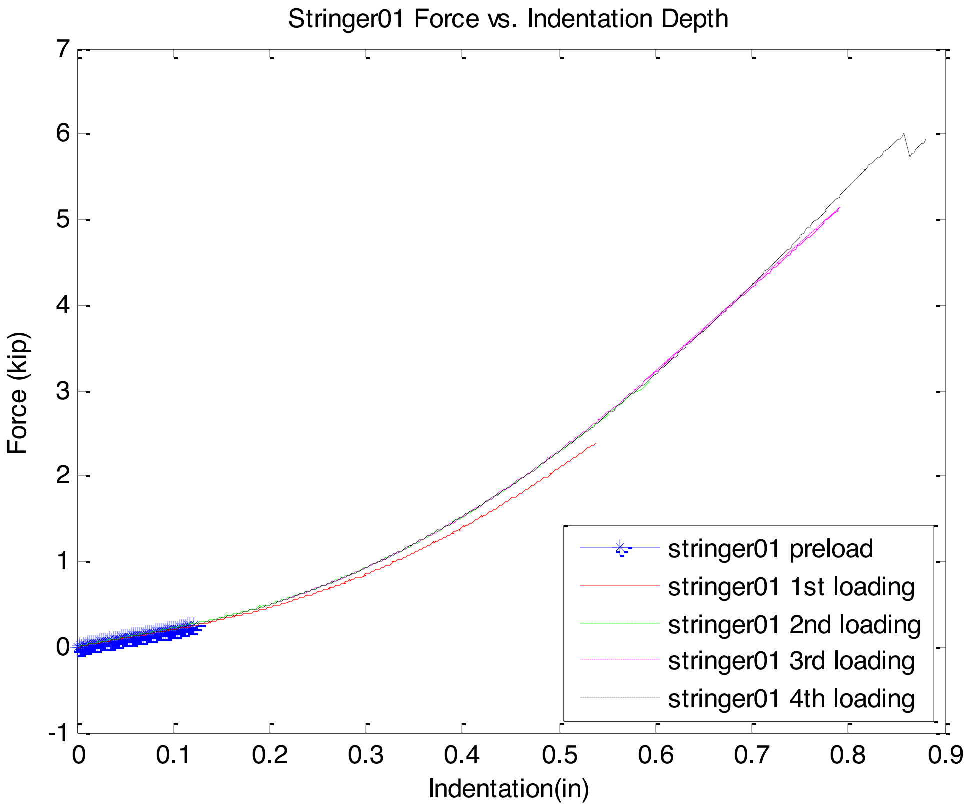

Figure 42: Stringer01 Force vs. Indentation Curves

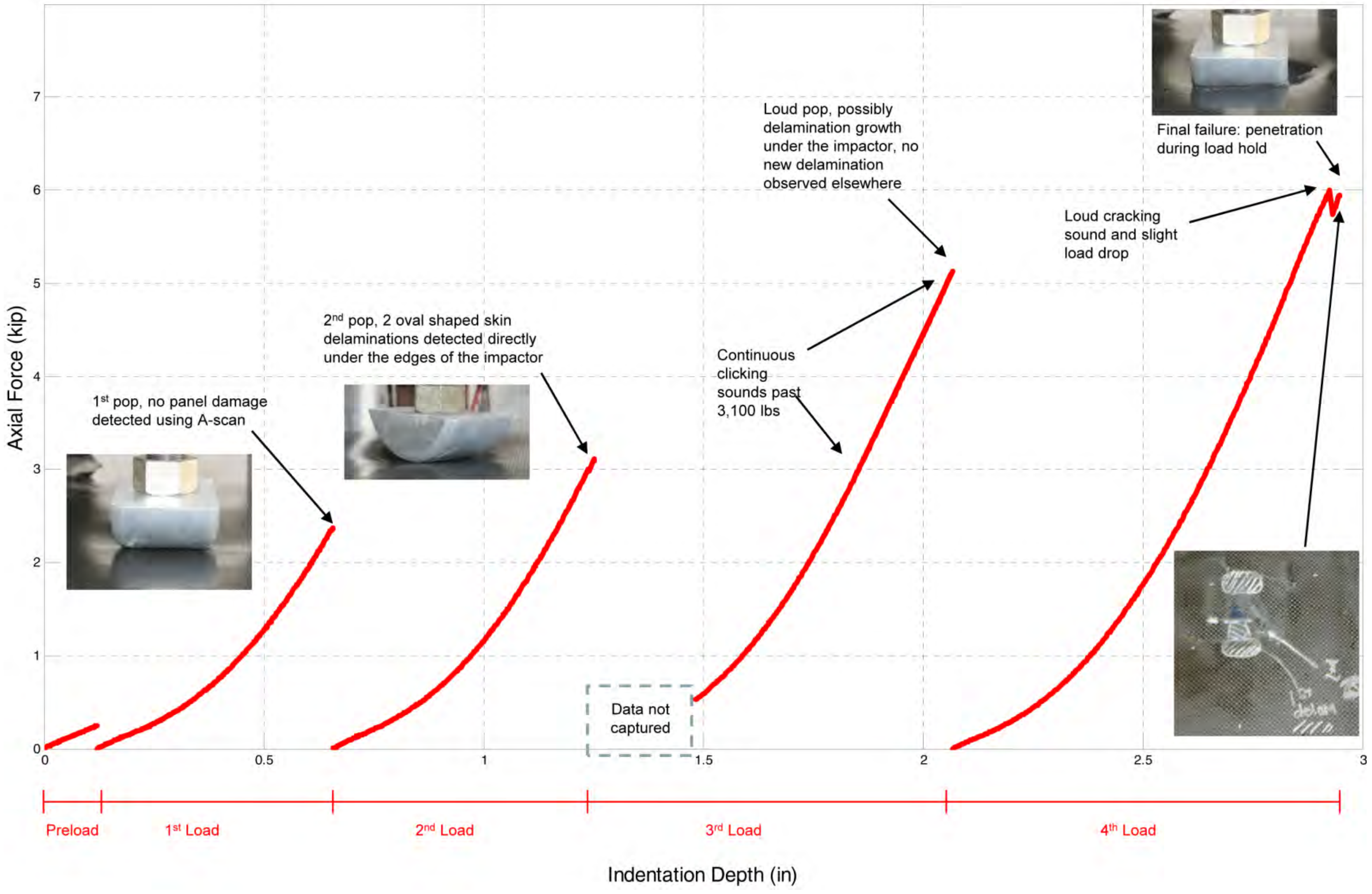

Figure 43. Stringer01 Time Event Plot

2.1.5.3 Stringer Specimen02

Stringer02 was indented at the same location as Stringer01 (on panel skin between stringers) but with the deformable rubber bumper (from TUG belt loader) instead of the rigid impactor. The rubber bumper deformed considerably and thus produced significantly more distributed load than the rigid 3 in. impactor. Figures 44 to 46 show the bumper before and during loading to convey the degree of deformation the bumper undergoes as it flattens out and builds up higher contact forces. The bumper conformed to the panel surface creating a larger contact area, resulting in lower contact pressures and lower localized interlaminar shear stress around the periphery of the contact area, thereby reducing the possibility of localized failure at the contact zone – and making it possible to develop failure in structural features located away from the location of indentation. When the bumper is fully flattened (see Figure 46) and the panel has undergone significant deformation, the corners of the bumper make contact with the stringer-skin connection, providing a direct load path into the stringers.

Figure 44: Stringer02 Prior to Loading by Rubber Bumper

Figure 45: Rubber Bumper in Initial Loading State on Stringer02

Figure 46: Large Deformation of Bumper and Panel Stringer02

1st Loading. During the first loading, the panel held a load of 10,080 lbs and experienced an indentation displacement of 1.09 in. directly under the center of the bumper before loud pop sound was heard. When the panel was unloaded, there was no delamination observed in the panel skin or between the stringers and skin. However, the shear ties experienced residual bending strains (nearly equal + and – values for back-to-back set) and there was visible radial delamination damage in the corners. Note that this load level is over 3X higher than when local damage (delamination) initiates for the 3 in. radius rigid indentor, and over 60% higher than the load at which penetration occurred in previously tested panels Stringer00 and Stringer01, both loaded by the 3 in. radius rigid indentor.

2nd and 3rd Loading. During the second loading, up to 11,214 lbs, active clicking sounds were observed at 10,000 lbs and large deformations in the panel produced an opening moment in the curved portion of the shear ties, leading to formation of radius delaminations at these locations. During the third loading, a large load drop occurred at 13,030 lbs at an indentation displacement of 1.27 in. The location where the panel is bolted to the shear ties experienced delamination between the skin and the stringer (i.e., at internal structural feature located away from indentation site). There was no delamination observed between the panel skin and stringer close to the bumper contact area.

4th Loading. During the fourth loading, delamination occurred between one of the stringer's inner flanges and the panel skin close to the location of indentation (see Figure 47), as well as at locations adjacent to the shear ties. Figure 48 shows the visible crushing/fiber damage in the curved region of the shear ties. The failure occurred at 13,787 lbs with a displacement of 1.36 in. No damage was visible on the exterior surface (see Figure 49) following unloading, even after the development of significant stringer delaminations. A full description of the delamination damage is given in a following section of this paper. There was also radial delamination and crushing/bending failure in the shear ties. It should be noted that after the load drop at 13,787 lbs, the panel still held a load of 10,580 lbs. i.e., it had not been penetrated, and still had load bearing capability. However, due to the extensive damage observed, the specimen was removed from the test machine and carefully inspected (nondestructively) to understand and document the damage incurred.

5th Loading. As a result of the high residual strength in Stringer02, a fifth loading was performed until the final failure (extensive delamination of stringers, greater load drop) occurred. During the fifth loading, asymmetrical loading of the panel was observed because the previously-delaminated stringer flange exhibited less stiffness than the intact stringer, thereby applying some moment loading into the indentor fixture and load cell. This can be observed by the non-horizontal tilt (right-side skewed slightly upwards) visible in Figure 50. The load path is redirected towards the intact stringer on the right-side of Figure 50. At 7,000 lbs, low energy clicks and pop sounds were observed. At a load of 10,500 lbs, substantial popping sounds were heard. The panel held up to a load of 12,440 lbs before the second stringer's inner flange (location ID: S2F1) delaminated as well. Figure 51 show that the final failure is a delamination of the second stringer that runs all the way to the free edge of the panel. It is hypothesized, however, that delamination of the stringer extended 1st from the shear tie location to the center of the panel (where loading is applied) in the zone where through-panel shear stresses exist, and the ensuing large deformations and high energy release propagated the delamination out to the free edge. The extent of the stringer delamination is mapped out by an ultrasonic c-scan and presented in Section 2.1.5.4.1.

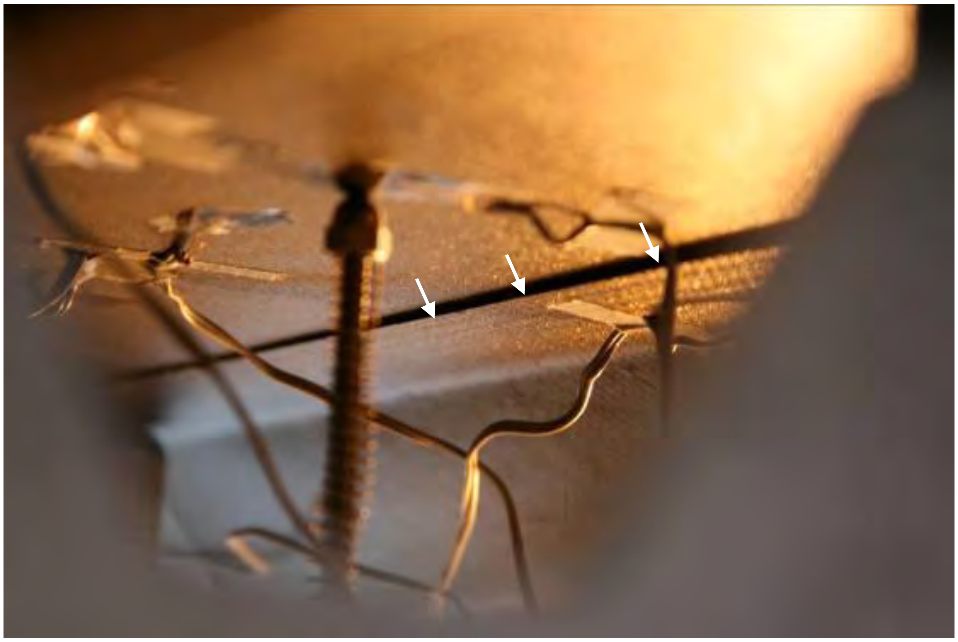

Figure 47: Stringer02 Delamination between the Skin and Stringer Following 4th Loading

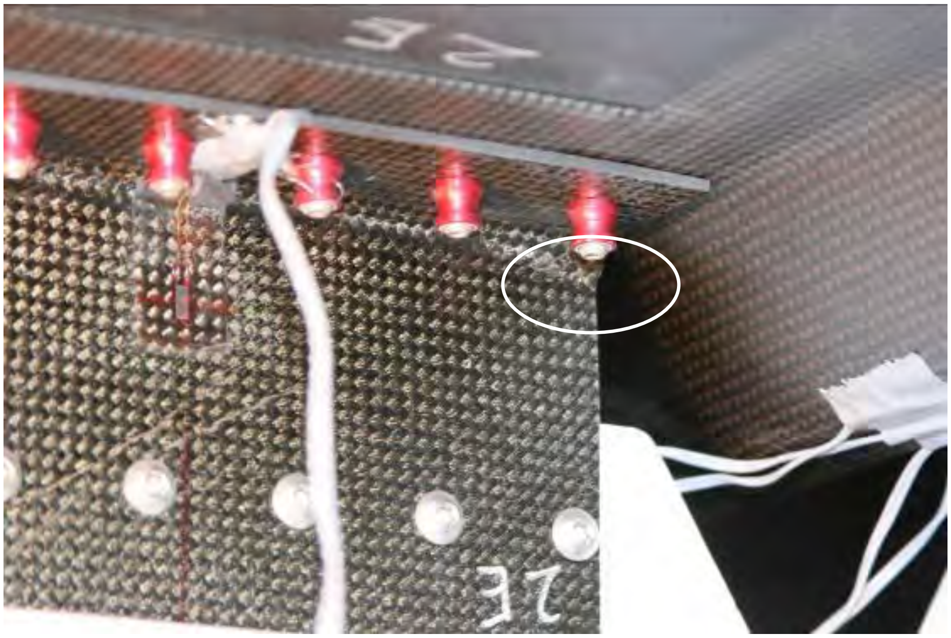

Figure 48: Stringer02 Radial Delamination of Shear Tie and Bending Failure at Corner Locations Following 4th Loading

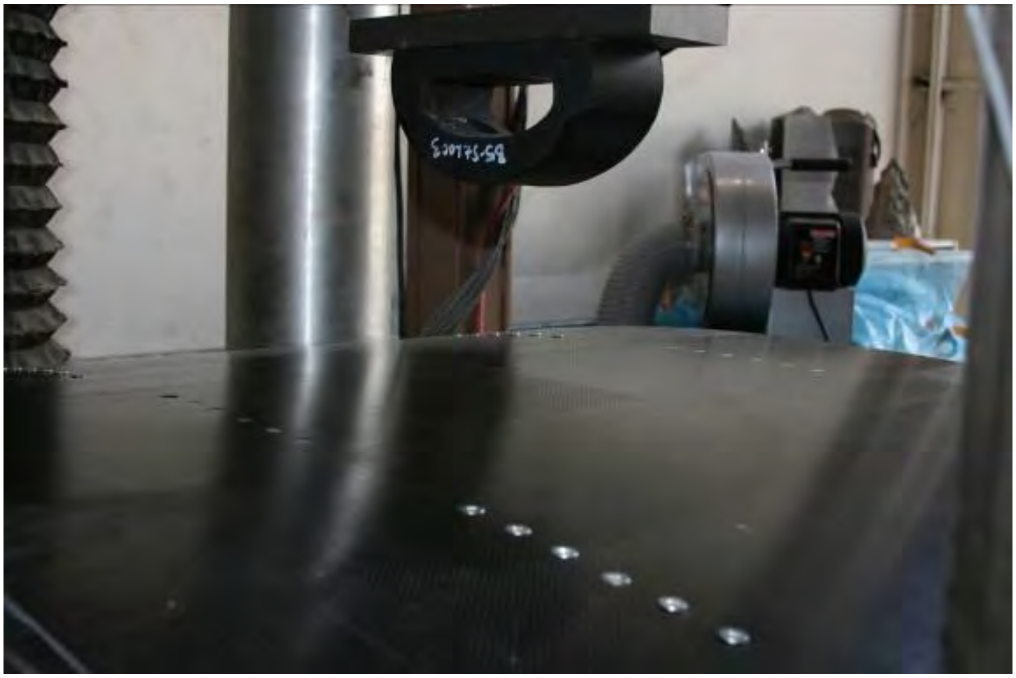

Figure 49: Exterior View of Stringer02 After First Stringer Delamination Following 4th Loading

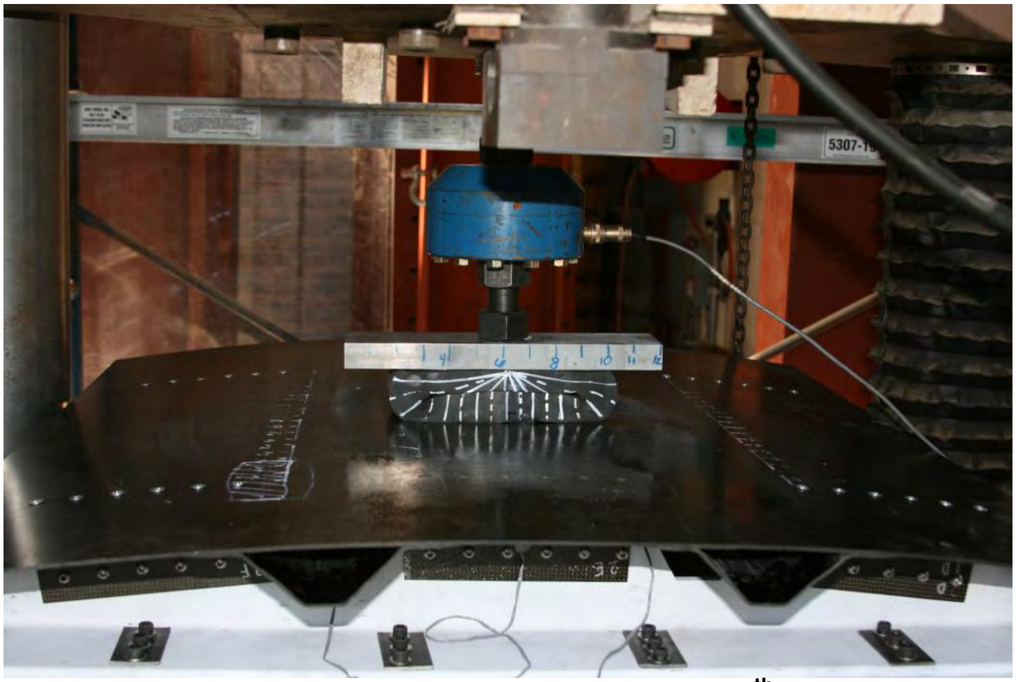

Figure 50: Stringer02 Under Load During 5th Loading

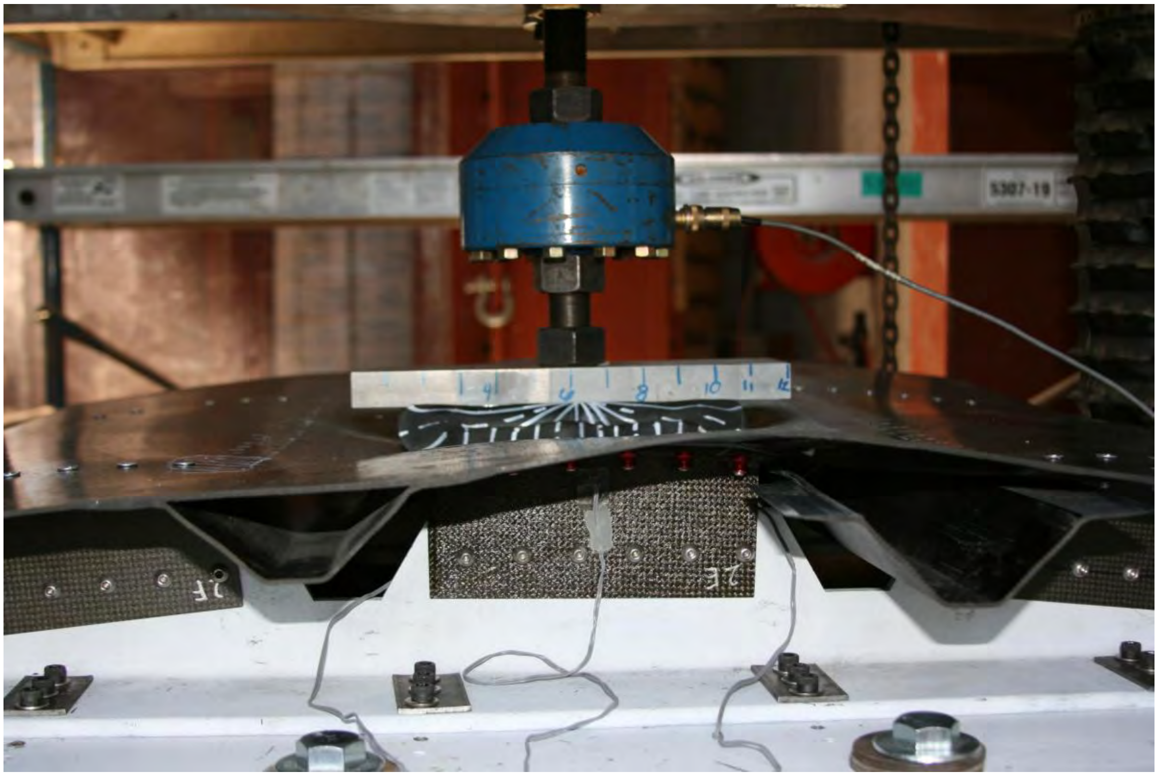

Figure 51: Stringer02 Following 5th Loading. Complete Delamination of the Right-Side Stringer (S2) Out to the Free Edge is Observed

Figure 52 shows the force vs. indentation curves for Stringer02 for each successive loading. Indentation of the panel was measured by a displacement potentiometer placed on the underside of the panel at the same location as Stringer01's. While the load-indentation curves for Stringer02 are similar to Stringer01, there are some inflections in the data observed at low-level loads due to the behavior of the rubber bumper as its "D" shape cavity deforms and collapses. When the load reached approximately 650 lbs (varies slightly with successive loading), the bumper fully collapses, thus stiffening the bumper, so that actuator displacements more directly translate into deformation of the panel.

Significant loss in stiffness can be observed with each successive loading. It is surmised that this is due to the accumulated damage including radial delamination developing in the shear ties, thereby affecting the rotational stiffness boundary condition (in earlier load cycles) and also delamination of thee stringer flanges following the 3rd Loading. Supporting evidence of this hypothesis was observed following specimen removal by noting the significant reduction in bending stiffness of the shear tie radius region, resulting from the extent of delamination forming there. The loading level at which delamination growth occurs can be inferred by noting the gradual softening of the fourth and fifth loading curves in Figure 52. Past 1.0 inch of indentation, the rubber bumper has reached a state of near-full compression so that the stiffness of the panel and the bumper becomes mostly constant, as observed by the nearly linear load vs. displacement relationship. Delamination growth in the stringers, to the degree that global stiffness is affected, is observable as a departures from the linear force vs. indentation trend (indicating stiffness loss). By observing the last segments of the 4th loading curve just before the load dropped, it can be concluded that delamination growth of the first stringer's inner flange (location ID: S1F2) initiated at a load level of 12,600 lbs and propagated until 13,860 lbs because the panel's stiffness drop in this loading range. Similarly, examination of the fifth loading curve allows one to deduced that the delamination growth of the second stringer's inner flange (location ID: S2F1) initiated at 11,520 lbs and propagated until 12,440 lbs.

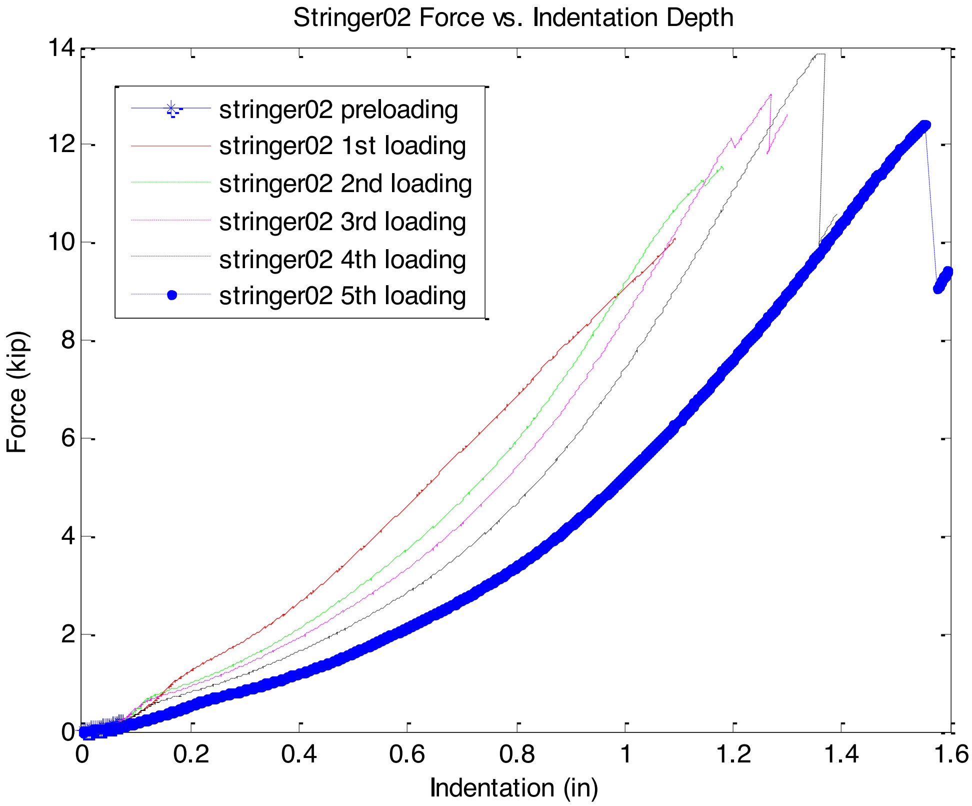

Figure 52: Stringer02 Force vs. Indentation Curves

The time event curve for specimen Stringer02 is shown in Figure 53 together with test observation notes of audible events and major failures for each loading cycle. Photographs of some damage features are also included in the plot. Significant timing passed between the 4th and 5th loadings to allow for careful examination and non-destructive mapping of the damage state. Even though shear ties were removed and re-assembled with new Hi-Lok fasteners, and the whole test fixture needed to be re-mounted on the SAETEC machine, and the specimen installed, the 5th Loading curve passed through the ending level of the 4th Loading (see Figure 52), despite the severe loss in stiffness, thereby indicating that no new damage was accumulated during the inspection

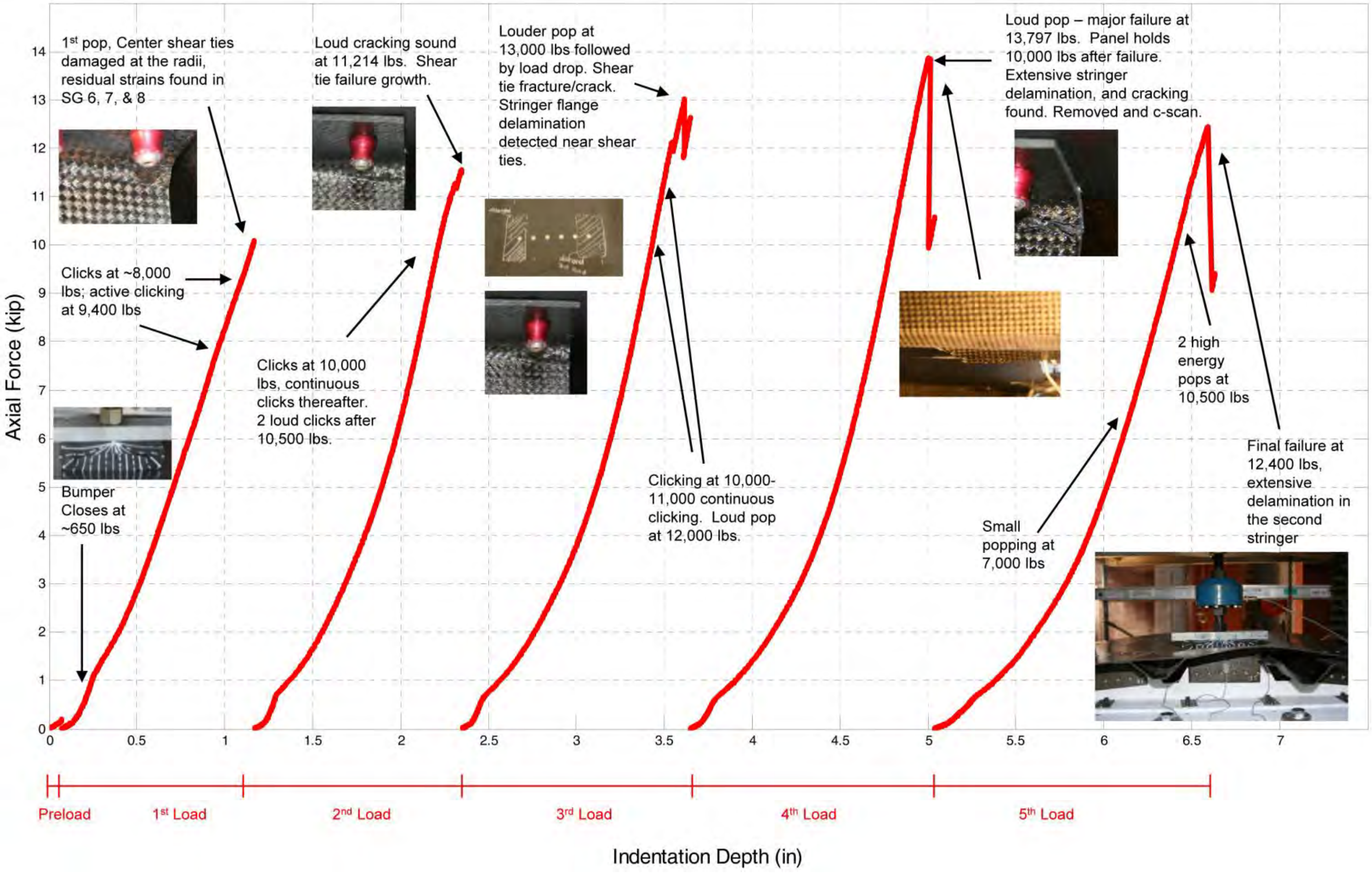

Figure 53. Stringer02 Time Event Plot

2.1.5.4 Post-Test Damage Assessment

2.1.5.4.1 Ultrasonic C-Scans

The center regions of the damaged panels Stringer01 and Stringer02 have been ultrasonically c-scanned from their indented side (one-sided pulse-echo) to map out the extent of damage, particularly internal delaminations of the skin, the stringer flanges and the shims between the skin and shear ties. The panels are scanned using an encoded manual xy-scanner for the Physical Acoustics Pocket UT portable c-scan system. A 5 MHz transducer operated in pulse-echo mode was used for the scans together with Ultragel II® couplant. The operating area of the xy-scanner is 18x15.7 in., which is smaller than the stringer panels. Therefore, multiple scans were conducted on each panel and the images were spliced together (locations of the shims and the bolt holes used to reference their relative positions. The panels were scanned at a line spacing resolution of 0.1 x 0.1 in.

The measurements by the pulse-echo transducer records the time of flight of the back-face reflected pulse, which is converted into a thickness measurement. Any internal delaminations thus show up as a “thinner” region due to the earlier reflection of the ultrasonic signal. These results are superimposed onto an outline drawing of the panel, including details such as stringer flange and shim locations. The colored regions represent the scanned area. The thicker regions on the panels are approximately 0.2 in. thick. These regions represent locations where stringer flanges are attached (co-cured) to the panel skin and also the shimmed skin locations, where the shear ties are bolted. Portions of the specimen that are this thickness are color coded red (darker shades in grayscale) in Figures 54 to 56.. The thinner regions on the panels are approximately 0.11 in. thick (this is the nominal thickness of the panel skin). The regions with this thickness represent the panel skin itself and are color coded blue and green (lighter shades in grayscale) in the figures. Additionally, regions that are this color where stringer flanges and shims are expected to exist (i.e., should be red colored) can be interpreted as locations where delamination has occurred at these interfaces. The white spots in the figures represent regions where an accurate reading could not be obtained due to surface irregularities and angular transitions that caused the transducer to lose contact with the panel – e.g., at transitions from the thin to thick regions of the panel. At these locations, the signal was momentarily lost.

Figure 54 shows the post-test scan of panel Stringer01. Note that the penetration by the Al indenter caused cracks on the panel surface and made it impossible to scan the area around the cracks. However, there is no damage in Stringer01 at locations away from the indentor loading region, as observed by the red and green shades appearing at their expected locations.

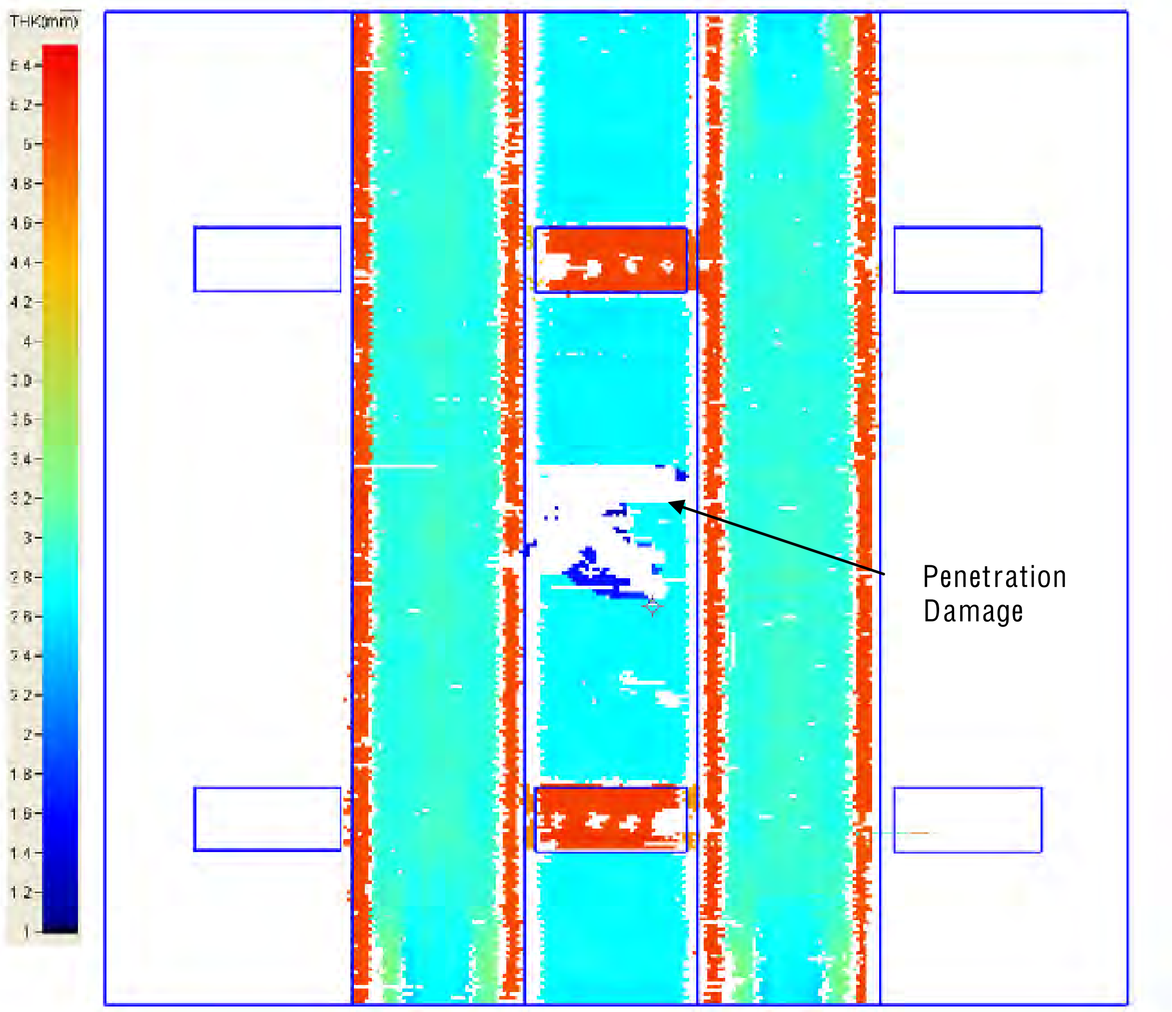

Figure 54. Post Test C-Scan Image of Stringer01 Indented by 3 in. Radius Aluminum Impactor (Resolution: 0.1x0.1 in). No Delamination of Stringer Flanges was Observed.

Figure 55 shows the scan of panel Stringer02 following the 4th Loading where extensive delamination occurred. There is no delamination within the panel's skin where the rubber bumper indenter contacted the panel. However, significant delamination occurred between the left-side stringer (S1) and the panel skin at the stringer's inner flange (S1F2). The damage is apparent by noting that the red colored shade defining the stringer flange locations, which run vertically through the color plot, is replaced by shades of green. The delamination, approximately 22 in. long, was visually confirmed during the test and it extends from the lower shim to past the upper shim. The outer flange of the same stringer also delaminated from the skin near the upper shim. This delamination is not visible from the outside and was undetected until the panel was c-scanned. The stringer on the right side (S2) also suffered delamination adjacent to the shims (shear tie location) as reported previously. Finally, one of the shims is found to have completely delaminated, despite the lack of visual evidence from the exterior. The bolt holes drilled through the shim appear as 4 white dots in the image; however, the red shade (expected due to thickness of skin + shim) is replaced by green (approximately skin-only thickness).

The c-scan image of Stringer02 after its 5th Loading is shown in Figure 56. Comparing Figure 55 with Figure 56, new delamination growth is found mainly in the right-side stringer (S2), whereas the left-side stringer (S1) suffered little to no additional delamination growth during the 5th Loading. This could be due to the asymmetric loading where load was primarily transferred from the rubber bumper to the shear ties and fixtures through the intact right-side stringer S2 (i.e., not through delaminated left-side stringer S1). The strain energy was thus higher in S2, leading to new delaminations only in the S2 flanges. The delamination grew from the shear tie region and extended to both sides of the shear tie along the stringer. It is hypothesized that the delamination first grew slowly towards the center of the panel and only propagated to the free edge during the moment of the final failure due to the large strain energy release. Supporting evidence for this hypothesis is the gradual stiffness change observed in Stringer02 load data, towards the end of the 5th loading, indicating delamination growth between the shear ties and the loading location. Any delamination between the shear ties and the outer free edge would not significantly affect the global stiffness of the panels since this location is no-participating material past the central span of the fixtures.

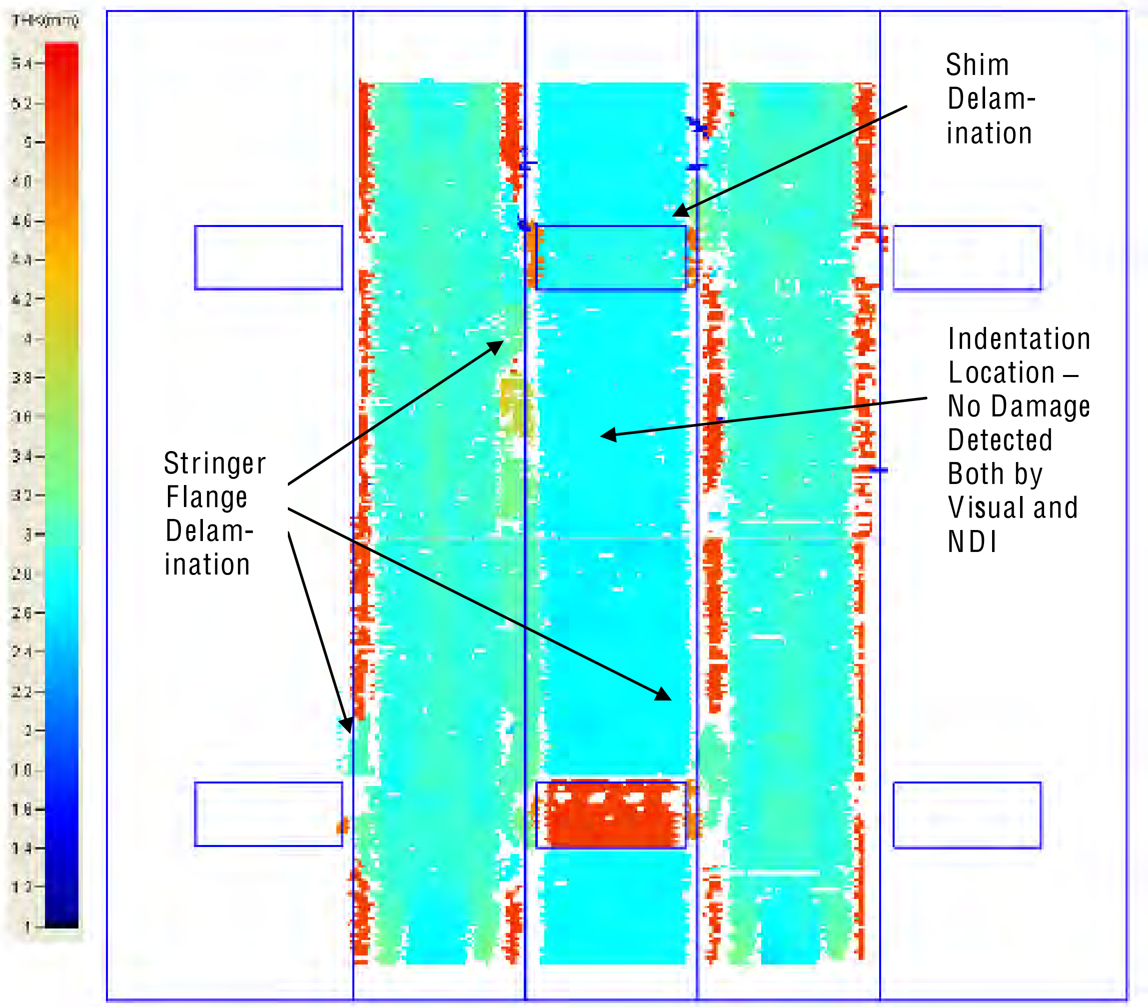

Figure 55. Post Test C-Scan Image of Stringer02 after the 4th Loading Indented by the Rubber Bumper (resolution: 0.1x0.1 in). Extensive Delamination of Stringer Flanges and Shim.

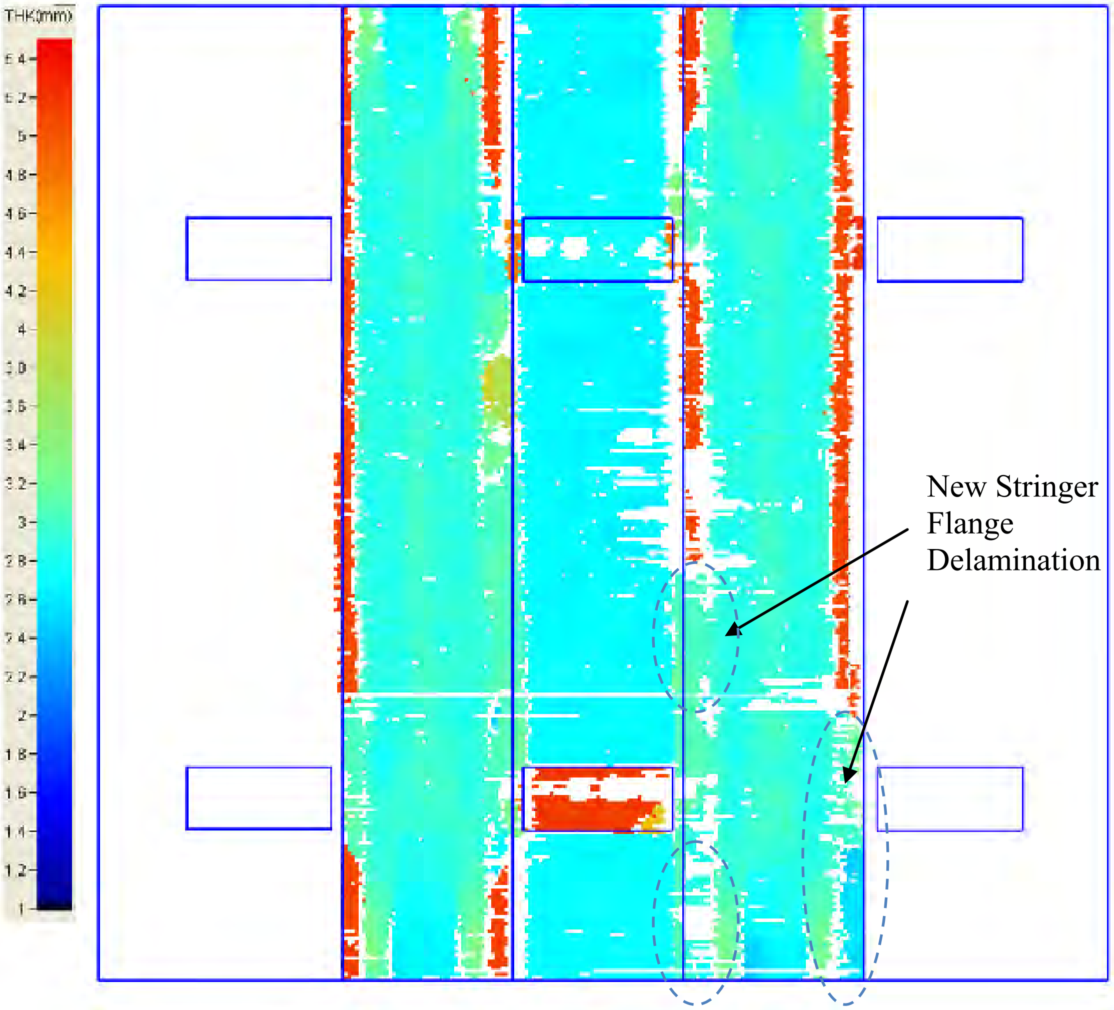

Figure 56. Post Test c-scan Image of Stringer02 after the 5th Loading Indented by Rubber Bumper (Resolution: 0.1x0.1 in). Delamination Growth Primarily in the Right Stringer (S2); Damage State Remained Unchanged Elsewhere in the Panel.

2.1.5.4.2 Shear Tie Delamination

A series of flexure tests were performed to quantify the residual stiffnesses of the shear ties for the recently-tested speciemens Stringer00, Stringer01, and Stringer02. These shear ties, especially those used for Stringer02, have sustained radial delaminations during their respective indentation tests. The names of the shear ties consist of a number and a letter. The number (0, 1, or 2) denotes the panel (Stringer00, 01, or 02) the shear tie was bolted to. The letter denotes the location of the shear tie on the specific panel. Shear ties that show signs of visible damage or are suspected to have been damaged were tested at this time. Shear ties 0B and 0C (from Stringer00) were bolted next to the legs of the loaded stringer on one end of the panel. They both showed crackings in the radius region on the side adjacent to the stringer. Note that shear ties 0F and 0G (opposite to 0B and 0C) showed a similar state of damage, but were omitted from this test. Shear ties 1B and 1E (from Stringer01) were bolted to the center of the panel on the opposing ends of the panel. Neither 0B or 0C showed damage, but are suspected to be damaged internally because of their proximity to the loaded region. Shear tie 1A did not show visible damage and was used as a pristine specimen to compare the data. Shear ties 2B and 2E (from Stringer02) were also bolted to the center of the panel and exhibit extensive radial delaminations.

The shear ties were held fixed to a vertical wall by the flange that would have been bolted to the panel skin. Three different masses were sequentially placed on the flanges of the shear ties at the location of where they would have been bolted to the test fixtures. The deflections were accurately measured by a laser extensometer and are plotted in Figure 57. The stiffness values determined from these data are listed in Table 3. Note in Figure 57 that shear ties 0B, 0C, 1B, and 1E do not exhibit any stiffness degradation, basically aligning with shear tie

1A. Shear ties 2B and 2E from panel Stringer02 suffered significant stiffness degradation.

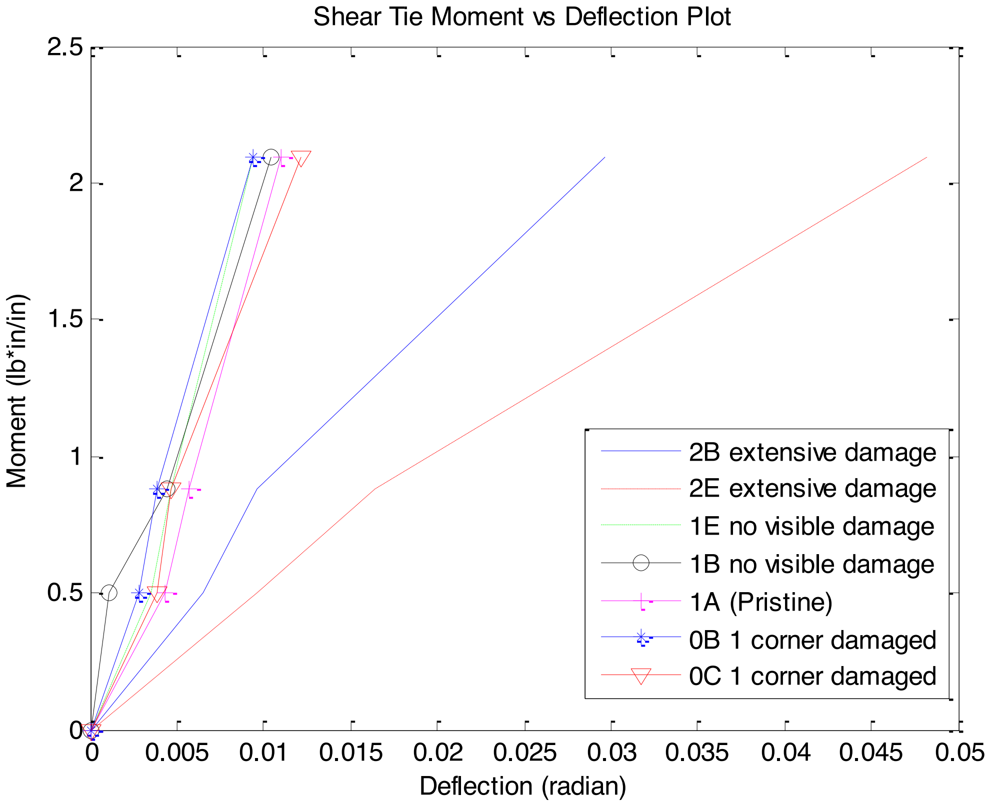

Figure 57. Moment vs. Rotation Plots for the Shear Ties.

Table 3. Residual stiffnesses of the shear ties

Shear Tie ID	Stiffness (lb-in)/rad
0B (1 corner damaged)	222
0C (1 corner damaged)	173
1B (no visible damage)	201
1E (no visible damage)	222
1A (pristine)	190
2B (damaged)	70.6
2E (damaged)	43.6

It should be noted that shear tie 2E visibly suffered more damage than shear tie 2B. A schematic diagram of their locations on specimen Stringer02 is shown in Figure 58. It can be seen that shear ties 2E and 2B were both oriented facing the same direction. Under conditions of small deformation, flexing of the panel skin due to indentation by the impactor would create an opening moment in 2E, and a closing moment in 2B. An Opening moment would cause radial delamination, whereas a closing moment would not. Therefore, if the damage in the shear ties were created by the flexing of the skin alone, shear tie 2B should have been undamaged. However, considering that large deformations were developed, producing significant membrane-tension stress in the panel skin, the ensuing deformation state would be one in which both shear ties 2B and 2E would be subject to opening moment. Also, it is suspected that the panel skin may have shifted horizontally in the direction of shear tie 2E during loading, causing opening moments in shear tie 2B. Additional displacement potentiometers will be used to track any possible horizontal movement of the panel in the future tests.

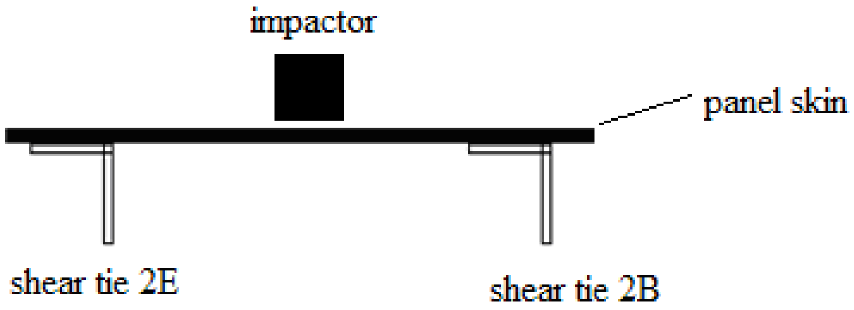

Figure 58. Locations of Shear tie 2E and 2B Relative to the Impactor.

2.1.6. Finite Element Correlation of Indentation Tests

Finite element models of the Stringer00 and Stringer01 panel specimens were developed to model the linear behavior (leading up to failure) of the indentation tests. In addition to correlation using the force vs. indentation data, strain gauges were also attached to the specimens to help develop models with accurately-predicted localized strains. Development of these models allow the prediction of the stress levels and moments in the panel leading up to initiation of local failures. The panel models were created in Abaqus finite element analysis software, using shell models with laminated composite sections. Material properties for the carbon/epoxy woven fabric and carbon/epoxy unidirectional tape were obtained from *Engineering Mechanics of Composite Materials* by Daniel and Ishai [4]. The indenters were created using solid sections. A slave and master surface interaction interface was defined for the contact between the indenter and the panel. The panel models were fixed by the edge of the shear ties in the model to simulate boundary conditions of the actual test. The indenter was displaced a fixed distance into the panel model.

2.1.6.1 Stringer00 FE Model

Figures 59 and 60 show the contact force and panel model surface strain predicted on the underside of stringer directly beneath the indenter, respectively, for specimen Stringer00. There is good correlation between the model and experimental data for the initial levels of indentation. In Figure 59 it can be seen that the load vs. indentation displacement was well matched up to 0.25 in. indentation. Beyond this level, the model is not matching the additional stiffening observed in the test. The surface strain prediction (see Figure 60) is found to closely match the test data for indentation displacement up to 0.5 in., i.e., the end of the 1st Loading of Stringer00. This is when localized delaminations form under the indentor head, causing stiffness loss which the elastic-only models do not capture.

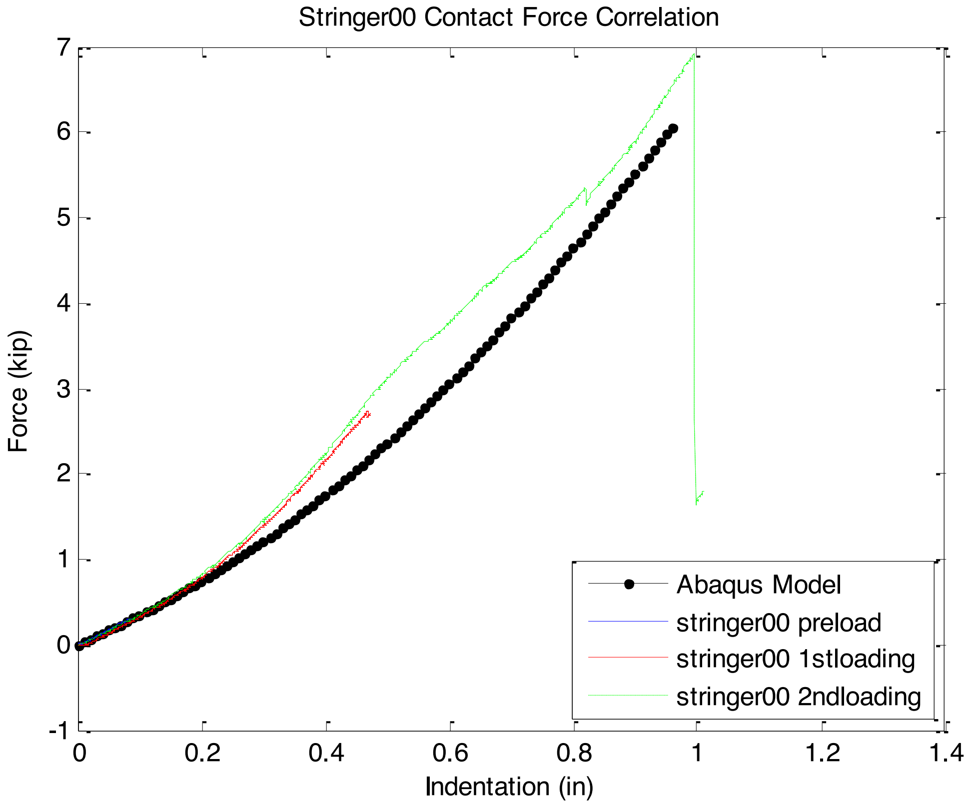

Figure 59. Contact Force of Stringer00 Model Plotted vs. Test Data.

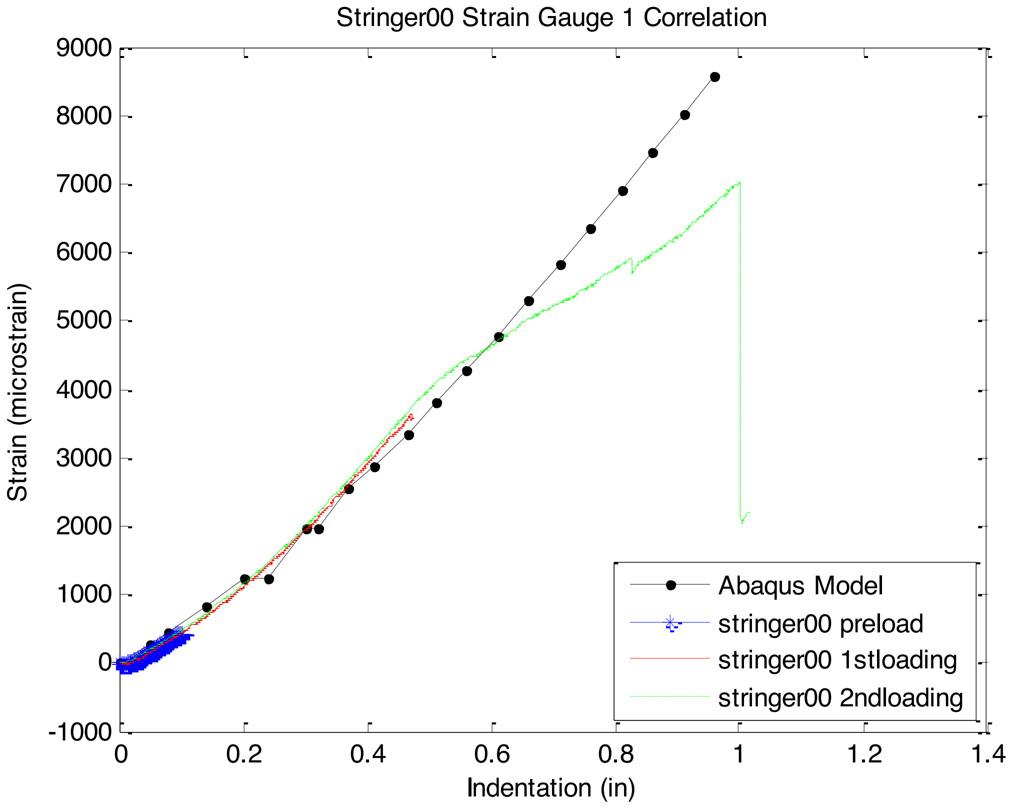

Figure 60. Surface Strain of the Stringer at Location Directly Beneath the Indenter for Stringer00; Model Data are Plotted with the Test Data.

Contour plots of the interlaminar shear stress resultants at an indentation depth of 1.0 in. are shown in Figures 61 (perpendicular to the stringer direction) and 62 (along the stringer direction). Both of these contour plots show a high concentration of interlaminar shear around the location of indentation, particularly at the edges of the 3 in. radius rigid indentor, and at the shear tie regions which is where large reaction forces exist as load is transferred to the fixtures through the shear ties. The location of indentation is where delaminations were observed in specimen Stringer00, and ultimately local bending failure of the skin under the indentor produced penetration failure mode. Higher load levels, would have created delamination near the shear ties, as was observed in Stringer02.

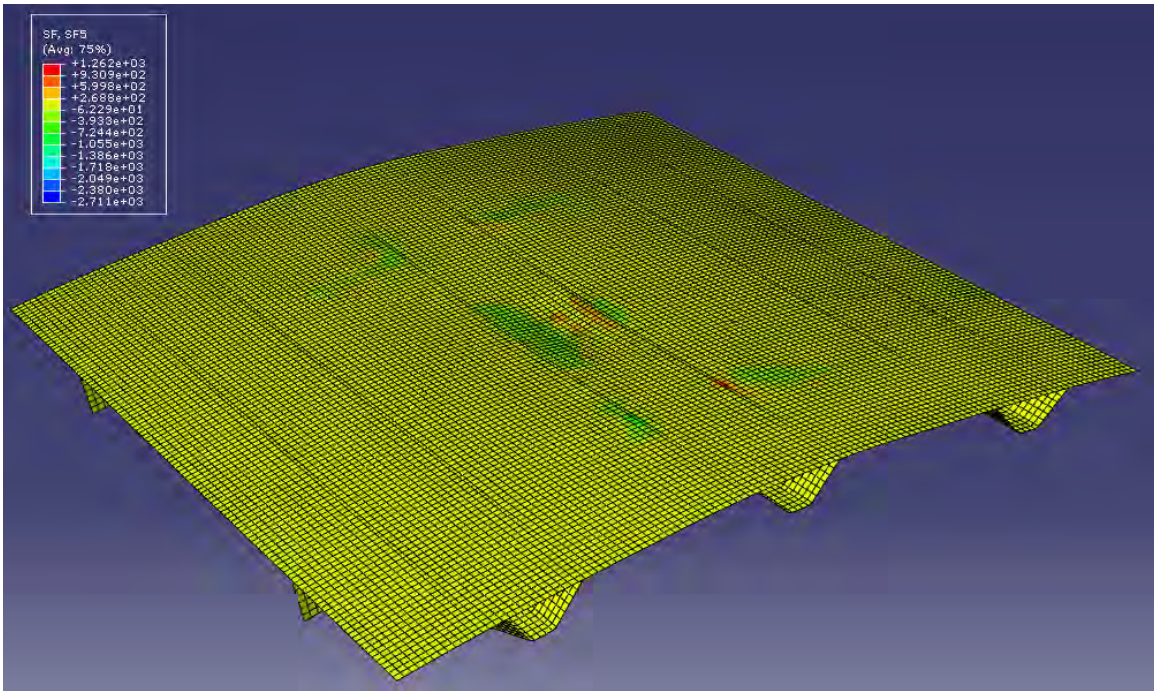

Figure 61. Interlaminar Shear Stress Resultants (Perpendicular to the Stringer Direction) in Stringer00

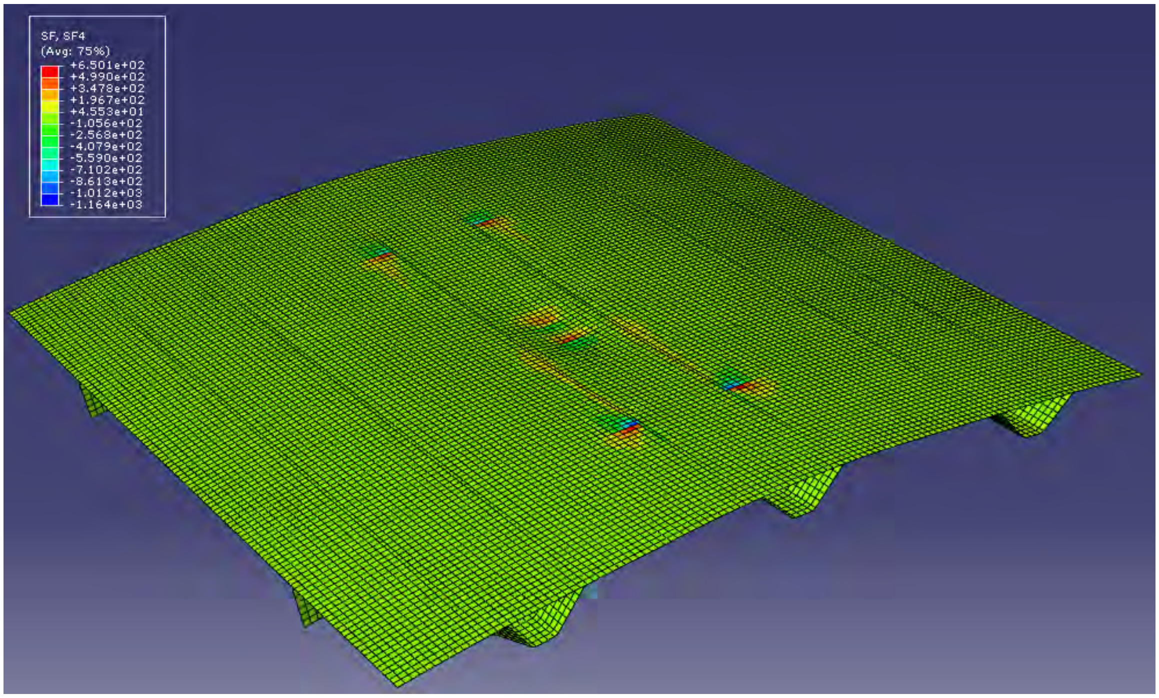

Figure 62. Interlaminar Shear Stress Resultants (Along the Stringer Direction) in Stringer00

2.1.6.2 Stringer01 FE Model

Model-predicted contact force in panel Stringer01 are compared to test data in Figure 63. The contact force showed good match with the test results up until 3,400 lbs, which corresponds with the loading when delamination was observed to initiate under the indentor head. Figures 64 and 65 show the interlaminar shear stress resultants for Stringer01 model at 1.0 in. of indentation depth. It can be observed from these figures that when impacted between the stringers, large interlaminar shear is developed at the edges of the indentor, and the panel develops high interlaminar shear within the stringer flanges adjacent to the shear tie locations (external reaction load paths).

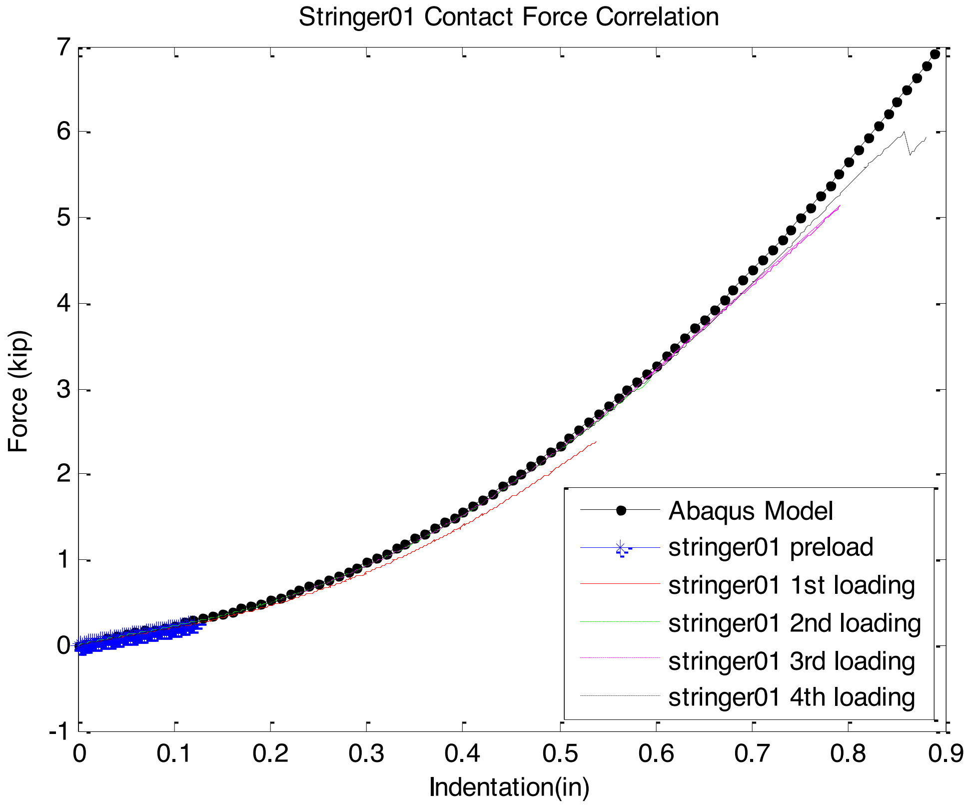

Figure 63. Contact Force of Stringer01 Model Plotted vs. Test Data

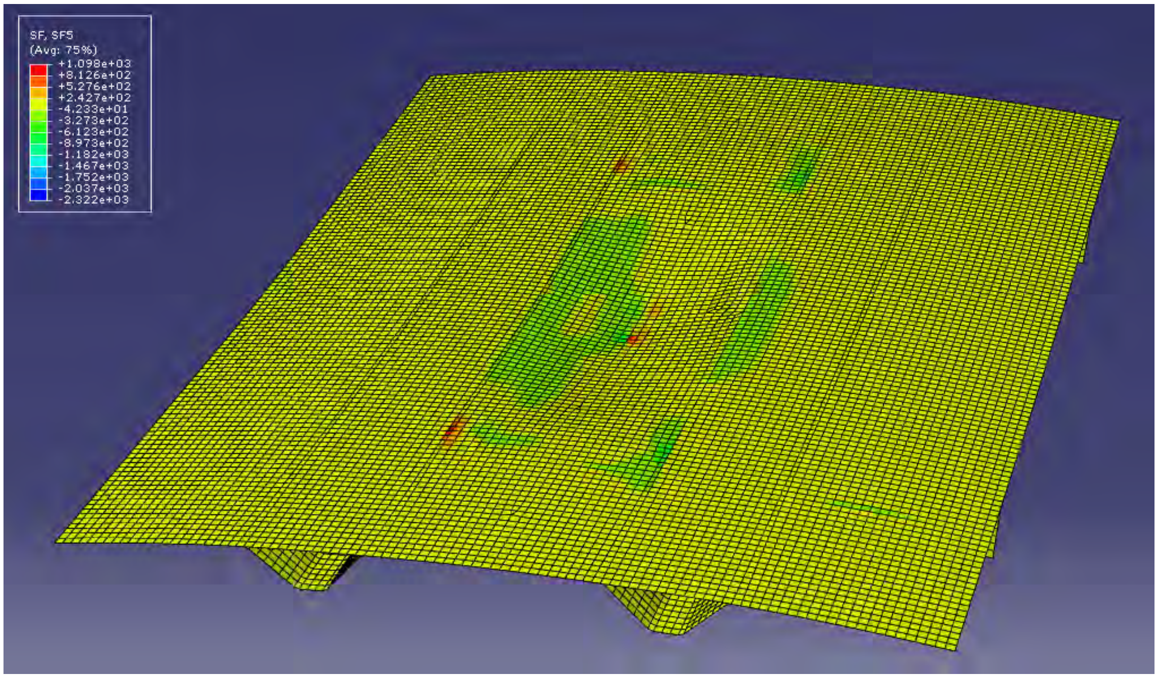

Figure 64. Interlaminar Shear Stress Resultants (Perpendicular to the Stringer Direction) in the Stringer01 Model

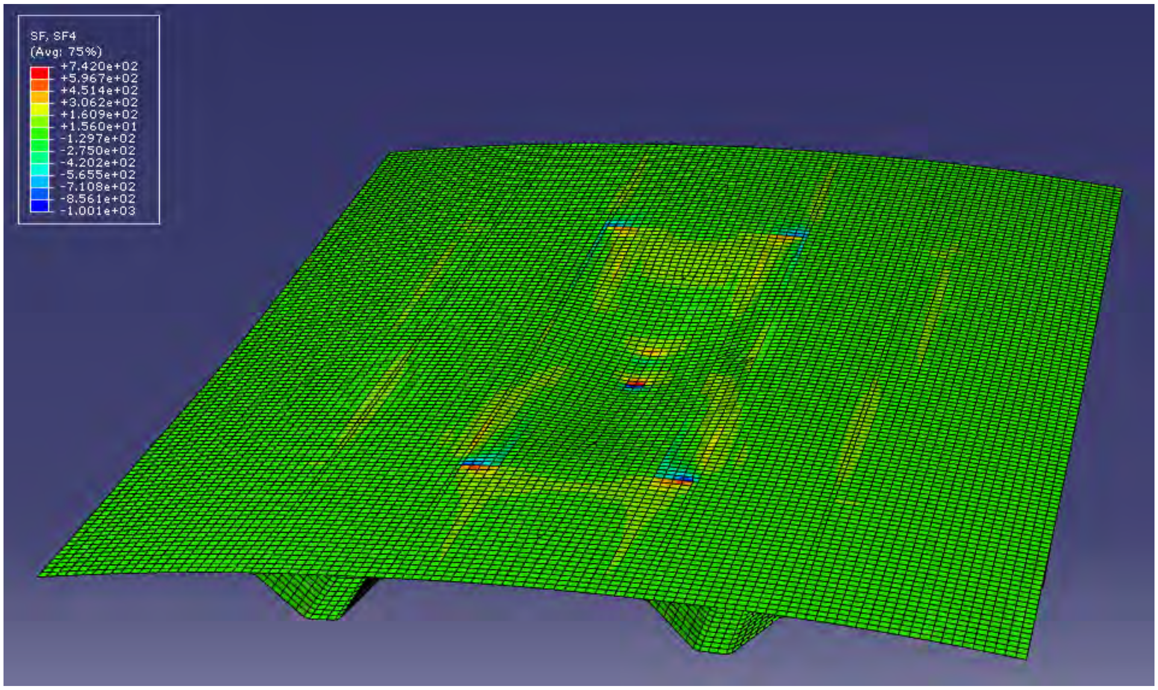

Figure 65. Interlaminar Shear Stress Resultants (Along the Stringer Direction) in the Stringer01 Model

2.1.7. Shear Tie Radius Delamination Coupon Specimens

Three 1-inch wide shear tie coupons were fabricated in order to determine the flexure behavior of the shear ties leading up to radial delamination when subjected to an opening moment. All three coupons were made using the same carbon/epoxy fabric material as that used for the large panel specimen shear ties. Pull-off tests using an MTS 810 22-kip Tensile Testing Machine were performed on these coupons with the setup shown in Figure 66. End tabs were attached to the frame-end of the coupons for gripping by the test machine, while the panel-end of the coupons were bolted to an aluminum fixture. An aluminum plate was also bolted on top of the shear tie to eliminate bolt pull-through failure.

The test results of the three coupons are shown in Figure 67. All the coupons exhibited consistent linear elastic behavior up until failure, with little scatter in failure load. The failure mode for all the coupons was delamination in the curved radius region, resulting from the interlaminar tension created by the opening moment produced from the pull-off loading. Figure 68 shows the radius region of the specimen where radial delaminations are visible, as expected, to exist near the midplane of the laminate. These data are useful in that they provide information on what loading radial delamination will form in the shear ties. They also serve as comparison data for future Finite Element model development which will seek to represent an effective degraded stiffness of the delaminated radius sections within the context of low-order shell elements, which can then be used in full-barrel models for blunt impact simulation.

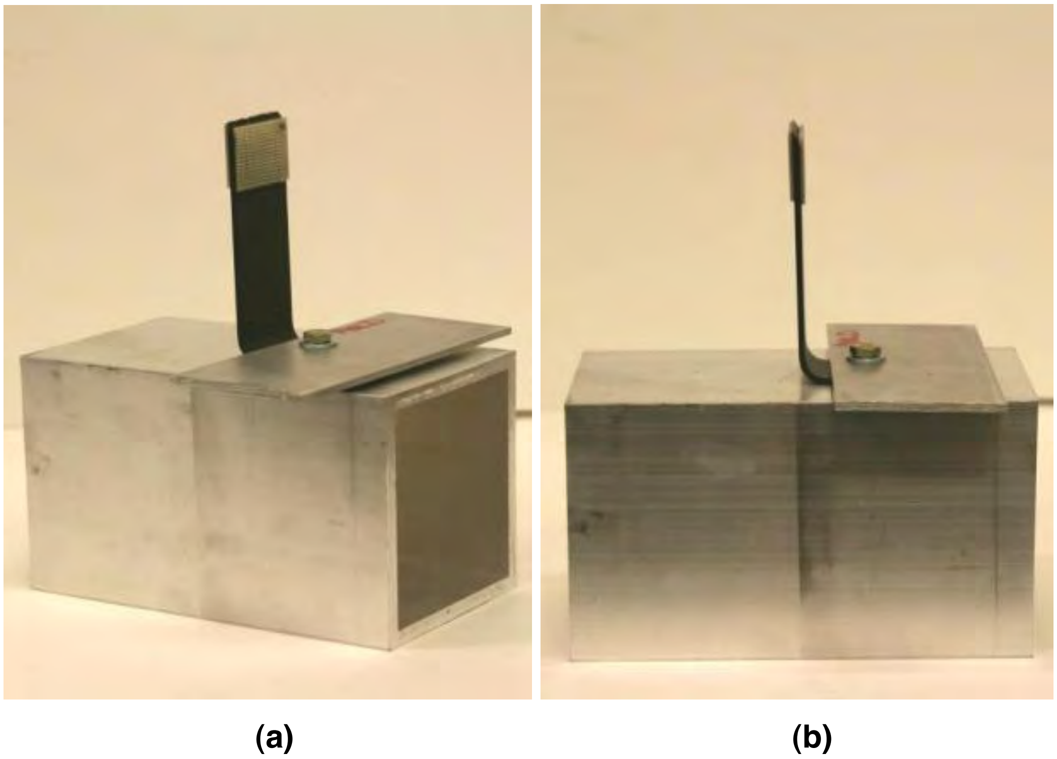
(a)
(b)

Figure 66: (a) Isometric View of the Pullout Test Fixture and (b) Cross-Sectional View of the Fixture.

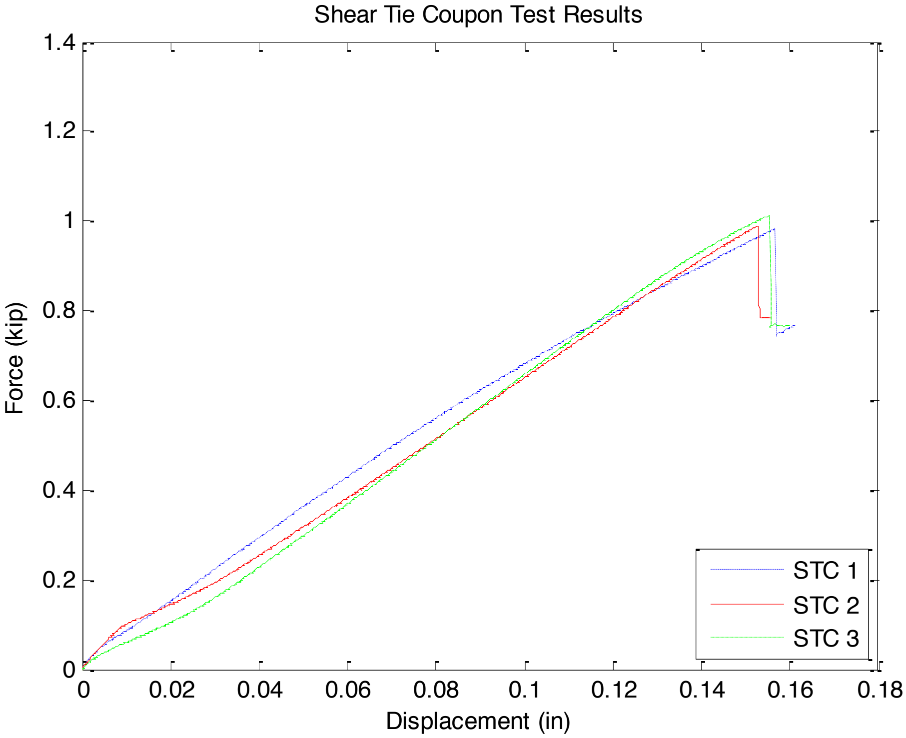

Figure 67. Force-Displacement Plot for the Shear Tie Coupons

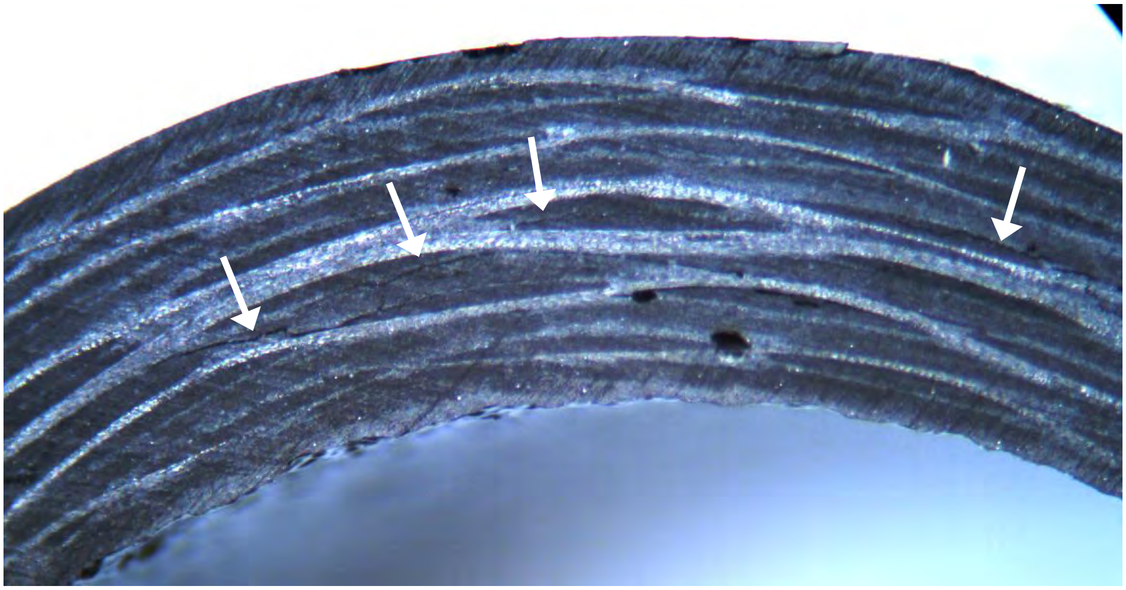

Figure 68. Photomicrograph of Shear Tie Coupons Showing Radial Delamination

2.2 High Velocity Ice Impact Damage to Composites

2.2.1 Overview

The overall objectives of this work includes:

(i) identifying the damage/ failure thresholds of ice impacts onto composite structures,

(ii) accurately modeling the impact event using finite element analysis, including accurate models of ice at impact strain rates and the prediction of damage initiation and damage state of composites, as well as contact force scaling information, and

(iii) determining a law for scaling contact force to allow for estimation of the peak force generated during ice impact as a function of projectile and plate stiffness (both local and global), the first natural frequency of the target, and deformation rate of the impacting object.

The identification of the delamination failure threshold energy (FTE) of aerospace-focused composites, defined as the minimum amount of projectile kinetic energy required to create damage in the structure, is found through a series of impacts onto composite panels to determine at what energy level delaminations start to occur, as detected by ultrasonic nondestructive inspection (NDI). The FTE measurements are aimed at determining the damage resistance of composites to hail ice impact as a function of material properties – describe by failure threshold energy (FTE) and failure threshold force (FTF). In addition, the ice impact experiments serve to produce panels with non-visible and barely visible impact damage (BVID) which are being studied in conjunction with

Airworthiness Assurance NDI Center (AANC) at Sandia National Lab. The emphasis of AANC's activity is on advanced non destructive inspection (NDI) methods for imaging the internal damage states and evaluation of probability of detection via visual inspection. The expected outcome of this work is to provide data, model, and NDI based relationships by which engineering estimations of damage occurrence can be made, given a known incoming projectile threat.

2.2.2 Experiments Description

The study in progress is investigating the damage resistance of composite panels impacted by high velocity simulated hail ice (SHI). Table 4 shows the number of panels being tested for numerous configurations. These tests are being conducted in collaboration with the Airworthiness Assurance NDI Center (AANC) that Sandia National Lab operates for the FAA. In addition, a series of strain gage instrumented tests (see Table 5) will be used to investigate both damaging and non damaging impact energy levels and produce data for model verification as well as force identification (see Section 2.2.4). Finally a series of impact tests will be conducted to investigate the effect of boundary conditions and panel size. The test matrix for this study is shown in Table 6.

Table 4. Failure Threshold Energy Determination Test Matrix (Number of Panels Indicated)

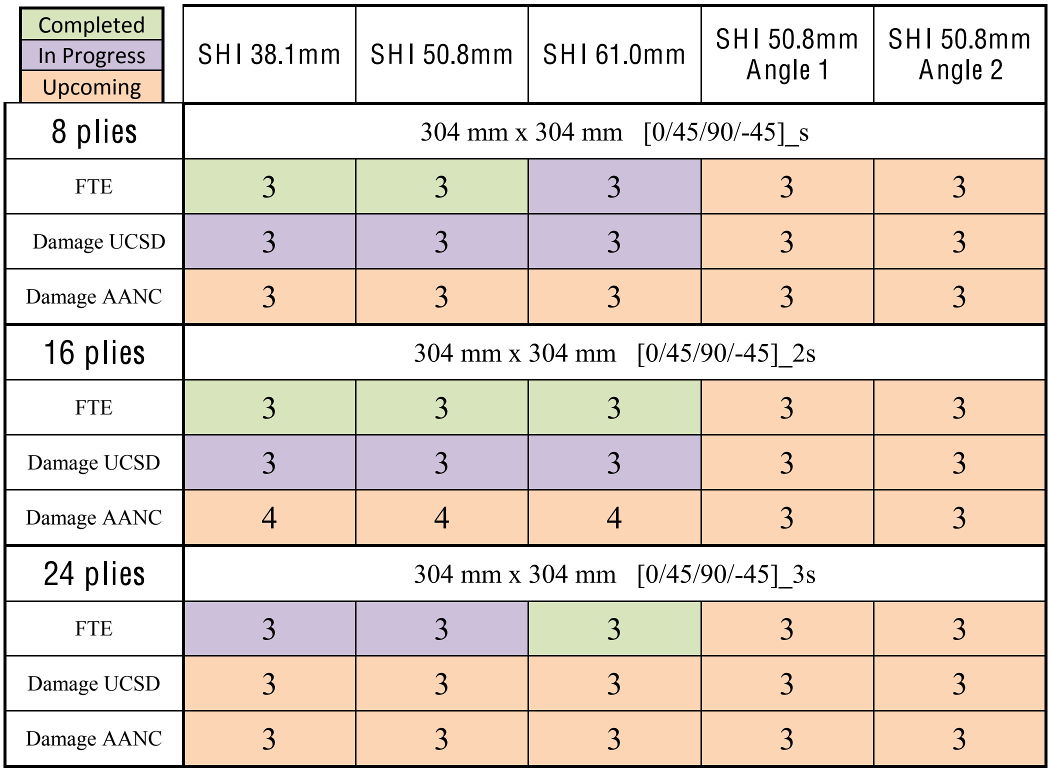

Completed In Progress Upcoming	SHI 38.1mm	SHI 50.8mm	SHI 61.0mm	SHI 50.8mm Angle 1	SHI 50.8mm Angle 2
8 plies	304 mm x 304 mm [0/45/90/-45]_s				
FTE	3	3	3	3	3
Damage UCSD	3	3	3	3	3
Damage AANC	3	3	3	3	3
16 plies	304 mm x 304 mm [0/45/90/-45]_2s				
FTE	3	3	3	3	3
Damage UCSD	3	3	3	3	3
Damage AANC	4	4	4	3	3
24 plies	304 mm x 304 mm [0/45/90/-45]_3s				
FTE	3	3	3	3	3
Damage UCSD	3	3	3	3	3
Damage AANC	3	3	3	3	3

Table 5. Instrumented High Velocity Ice Impact Tests

Panel Size	SHI Diameter	Velocity
8 ply, 304 mm	38.1 mm	Non Damaging V1
8 ply, 304 mm	50.8 mm	Non Damaging V1
8 ply, 304 mm	50.8 mm	Non Damaging V2
8 ply, 304 mm	50.8 mm	Damage 120% FTE
16 ply, 304 mm	38.1 mm	Non Damaging V1
16 ply, 304 mm	50.8 mm	Non Damaging V1
16 ply, 304 mm	50.8 mm	Non Damaging V2
16 ply, 304 mm	61.0 mm	Non Damaging V2
16 ply, 304 mm	50.8 mm	Damage 120% FTE
24 ply, 304 mm	38.1 mm	Non Damaging V1
24 ply, 304 mm	50.8 mm	Non Damaging V1
24 ply, 304 mm	50.8 mm	Non Damaging V2
24 ply, 304 mm	50.8 mm	Damage 120% FTE

Table 6. Test Matrix for Investigating Effects of Boundary Condition and Panel Size

Panel Size	SHI Diameter	Boundary Condition
304 mm, 16 ply	50.8 mm	Bolted Corners
304 mm, 16 ply	50.8 mm	Bolted Corners
608 mm, 16 ply	50.8 mm	Picture Frame
608 mm, 16 ply	50.8 mm	Picture Frame
608 mm, 16 ply	50.8 mm	Bolted Corners
608 mm, 16 ply	50.8 mm	Bolted Corners

The high velocity impact tests set up includes multiple pieces of equipment (see Figure 69): a gas gun, laser velocity measurement system, and high speed video camera. The nitrogen gas gun in use was designed and constructed by Professor Hyonny Kim; it has two possible barrel diameter sizes, 79 mm and 38 mm, and is 2.3 m in length. It utilizes a breech for the insertion of projectiles. The velocity range for projectiles is approximately 30 to 250 m/sec. (Kim et al. [3], Nightingale [5]). Furthermore, a laser photogate system is set in the projectile path to measure velocity prior to impact. The high velocity tests are also recorded by black and white high speed video cameras. The cameras (Phantom V.7.3) are run at frame rate of approximately 10,000 frames/sec with shutter speed 20 μs to capture “frozen” images of the impact process.

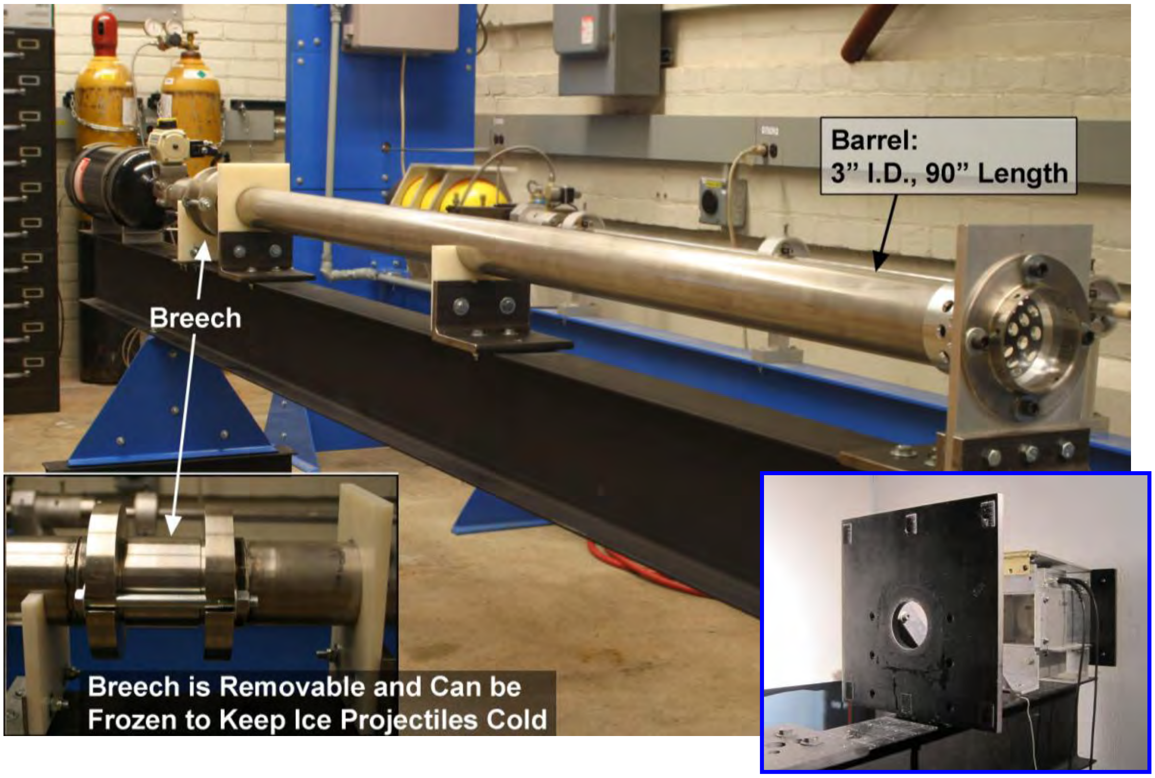

Figure 69. High Velocity Gas Gun System; Sabot Stop and Laser Photogate in Inset

The procedure for high velocity impacts begins by placing removing the SHI from the freezer, recording the mass, and placing it into a foam sabot. The sabot is then loaded into the breech of the gas gun. The breech is closed, pressure is increased to a value determined by the desired velocity and the gun is fired. When the projectile and sabot exit the gun barrel the sabot opens slightly, it is then caught by a sabot stop, which a square steel plate with an approximately 70mm diameter hole in it (see Figure 69). This separates the sabot and SHI, the SHI then continues towards the target passing through a series of three lasers, the first triggers the high speed video, while the second and third allow for a velocity measurement. Finally the projectile impacts the target. The data are processed and video files save. Each test contributes new data to the pressure versus velocity plot shown in Figure 70.

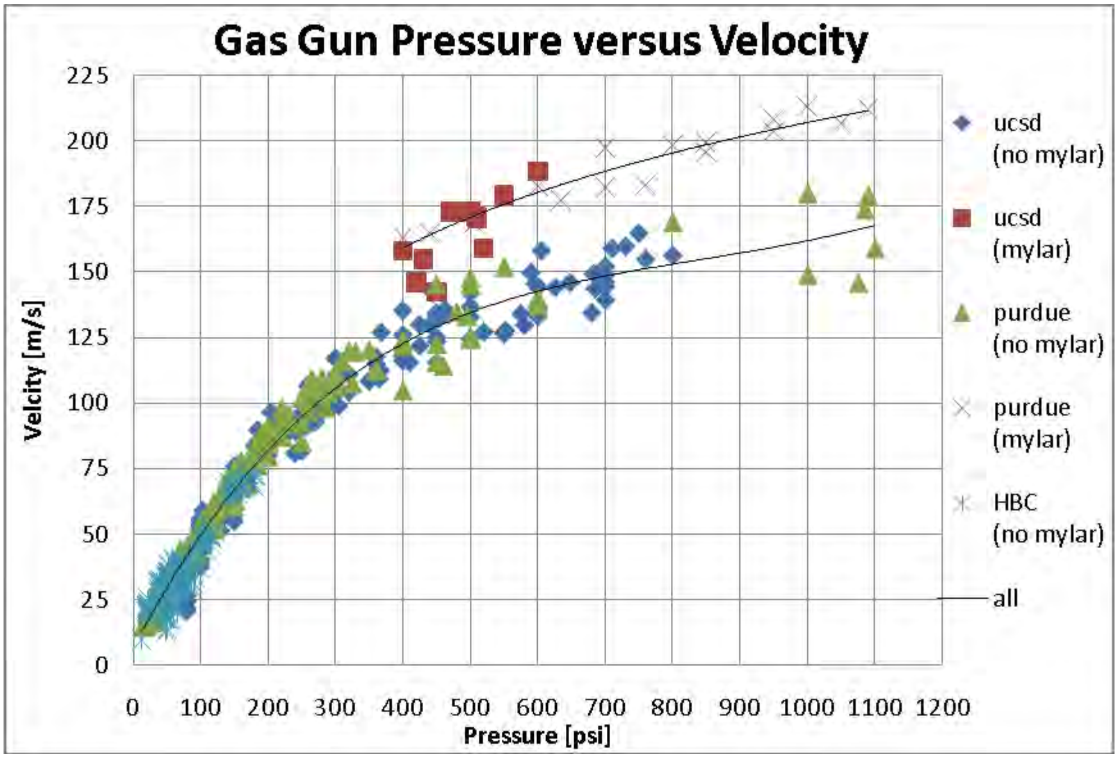

Figure 70: Gas Gun Pressure Versus Velocity

Non-destructive evaluation (NDE) equipment was used to examine the damage created by the impact events. Specifically a Physical Acoustics Pocket UT with a 5 MHz transducer is used for in situ A-scans, and an immersion C-scan tank, a Physical Acoustics UltraPac II system with 5 Mhz through transmission transducers, is used for a complete mapping of the target panels post test. These systems are shown in Figure 71.

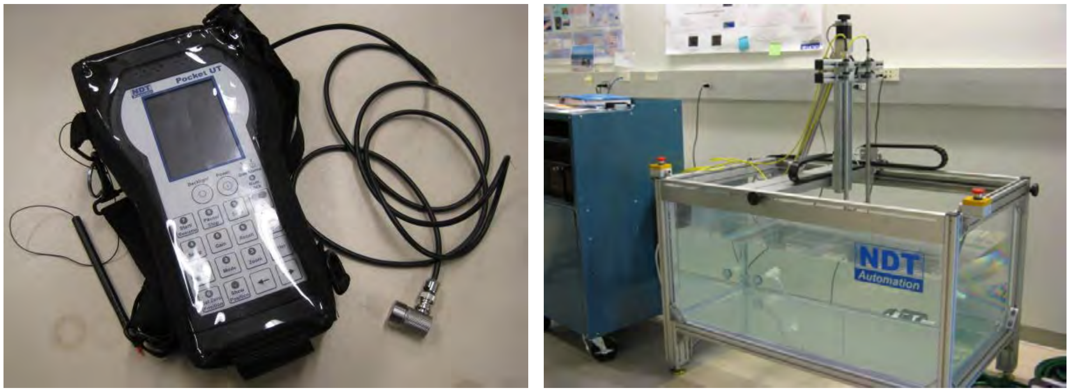

Figure 71: NDE Equipment; Pocket UT (Left) and C-Scan Immersion Tank (Right)

2.2.3 Test Specimen Details

The panels that have been constructed to date are 304 mm square, and of three thicknesses: 8 plies (1.59mm), 16 plies (3.11mm) and 24 plies (4.66 mm), all lay ups are quasi-isotropic, specifically: $[0/45/90/-45]_s$, $[0/45/90/-45]_{2s}$, and $[0/45/90/-45]_{3s}$. Furthermore, all current targets were made from the same material system, Toray T800/3900-2 Graphite/Epoxy tape (a.k.a. BMS8-276N). The properties for this material are shown in Table 7. The fabrication of these panels was completed by UCSD and they were transported to a local company's (San Diego Composites) autoclave to be cured under 90 psi pressure at 355 degrees Fahrenheit with a hold of 130 minutes, in accordance with the cure cycle for 3900-2 resin provided by Toray.

Table 7. Material Properties (Liyong and Soutis [6])

Youngs Modulus:	(Msi)	(GPa)
E11	23.2	160.08
E22	1.3	8.97
E33	1.3	8.97
Poisson:	-	-
v12	0.28	0.28
v13	0.28	0.28
v23	0.36	0.36
Shear Modulus:	(Msi)	(GPa)
G12	0.9	6.21
G13	0.9	6.21
G23	0.5	3.45
Strength:	(ksi)	(MPa)
Long Tensile	412	2842.8
Long Compressive	225	1552.5
Trans Compressive	24	165.6
Fracture Toughness:	in-lb/in^2	m-kg/m^2
G1c	0.86	15.36
G2c	2.7	48.22
Other:		
Shear Nonlinearity	11664	11664
Ply Thickness (in) (mm)	0.00645	0.16383
Fiber interaction zone (in) (mm)	0.055	1.397

The majority of panels are being tested with boundary conditions that are referred to as a “picture frame” fixture. This fixture, shown in Figure 72, has a 267 mm square opening, and restrains out of plane motion and rotation but allows some in-plane motion. As stated in Section 2.2.2, a change in boundary conditions will also be explored. The other condition being investigated is a pinned-free condition: four bolts, one in each corner, are used to hold the panel with a one inch standoff from the test frame. Of interest is how strongly the boundary conditions affect the determination of FTE.

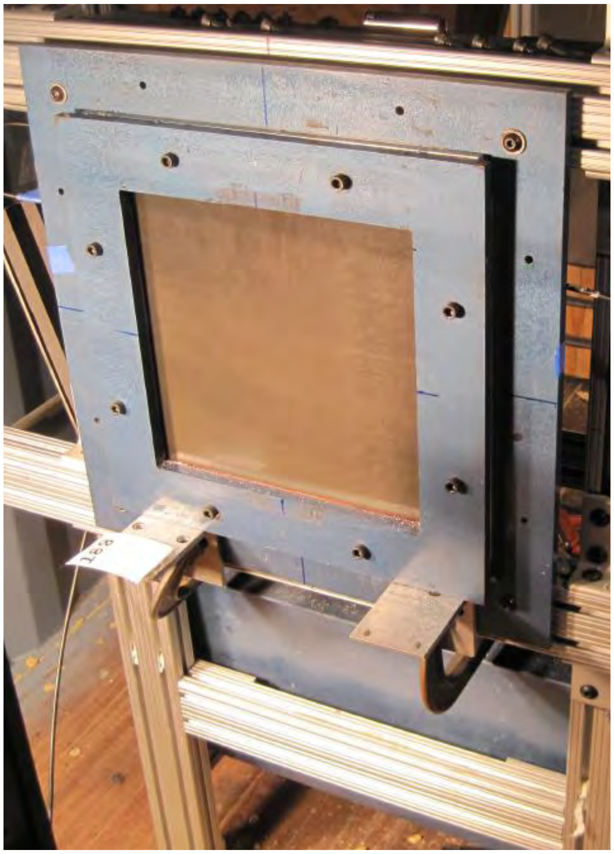

Figure 72: **Composite Panel Mounted in "Picture Frame" Fixture**

2.2.4 Test Results

The identification of the delamination failure threshold energy (FTE), defined as the minimum amount of energy required to create damage in the structure, for a combination of three panel thicknesses and three ice sphere diameters, is presently in progress. These are found through a series of impacts onto composite panels to determine at what energy level delaminations start to occur, as detected by ultrasonic A-scan. Impacts are conducted to narrow the energy range between non-damaging and damaging events. A range of values between the highest non-damaging and lowest damaging shot is used to define the FTE range. Once the energy range is within 10 percent of the average, the configuration is concluded. The current FTE ranges are shown in Table 8. These data, plotted in Figure 73, reveals a linear dependence of the FTE on both panel thickness and SHI diameter.

Table 8. Ice Sphere Impact Failure Threshold Energy Ranges

	SHI 38.1		SHI 50.8		SHI 61.0	
	Lower Bound	Upper Bound	Lower Bound	Upper Bound	Lower Bound	Upper Bound
8 plies	196 J	224 J	254 J	263 J	174 J	276 J
	123 m/s	131 m/s	93 m/s	94 m/s	56 m/s	72 m/s
16 plies	332 J	384 J	453 J	458 J	484 J	505 J
	162 m/s	172 m/s	120 m/s	122 m/s	95 m/s	98 m/s
24 plies	368 J	434 J	666 J	768 J	872 J	925 J
	172 m/s	187 m/s	144 m/s	159 m/s	127 m/s	133 m/s

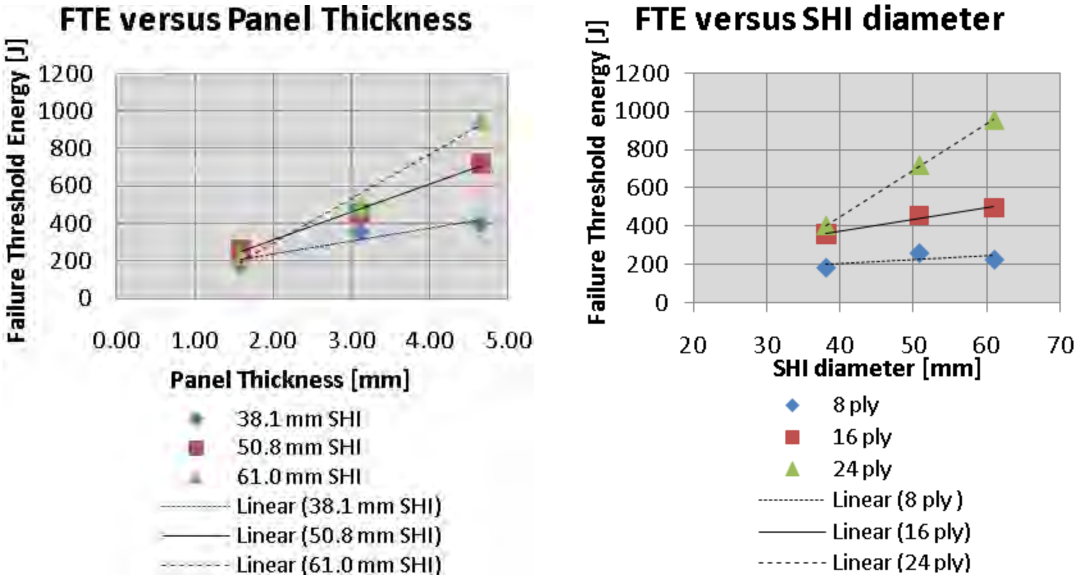

Figure 73: FTE Versus Panel Thickness and SHI Diameter

Once testing of a panel is complete, the panel is subjected to a complete mapping by ultrasonic C-Scan. This allows for the assessment of the size and shape of any delaminations present. Figure 74 shows two example scans. A cluster analysis is done to find the total delamination area. This value is then plotted against the energy of the damaging impact. These plots, shown in Figure 75, of delamination area versus projectile kinetic energy for each configuration are useful in establishing FTE data.

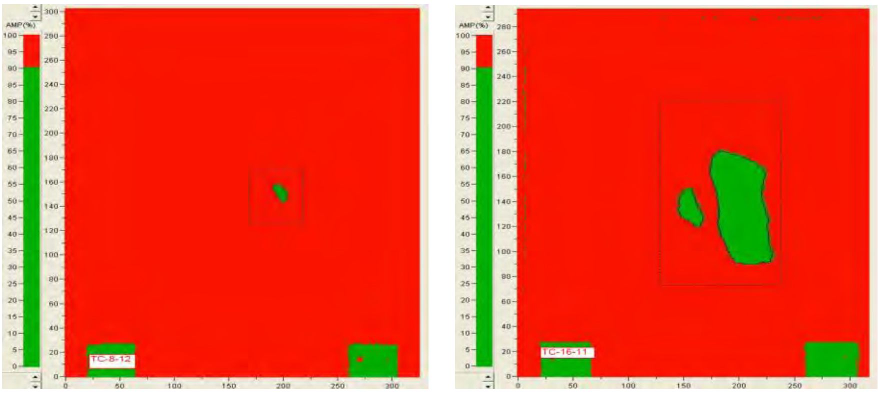

Figure 74: C-Scan of Delaminated Panels.
(Left) Test 205, 38.1 mm SHI Impacting 8 ply Panel at 134 m/s
(Right) Test 173, 61.0 mm SHI Impacting 16 ply Panel at 98 m/s

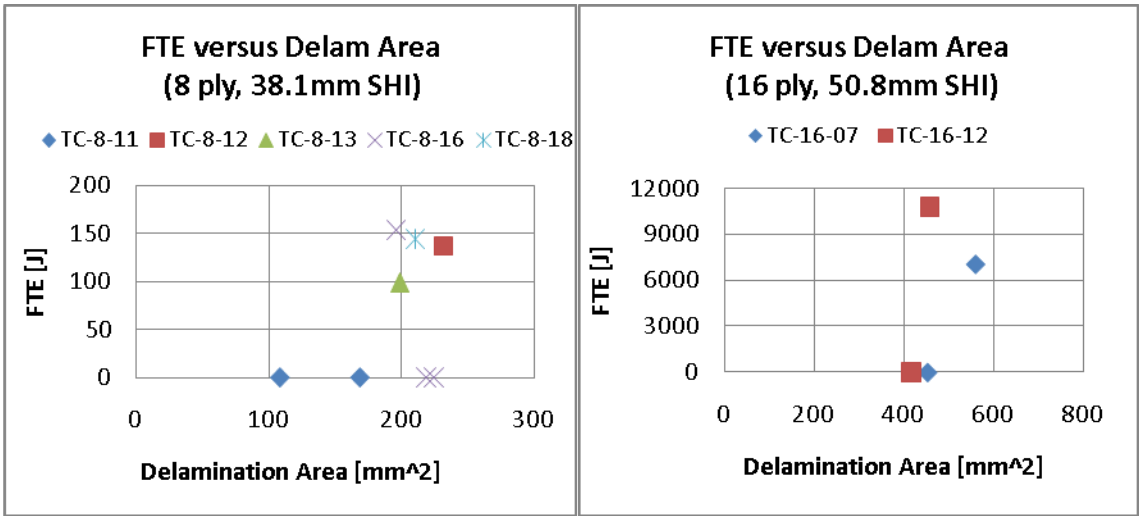

Figure 75: Example FTE Versus Delamination Area for 8 and 16 Ply Panels

For selected tests, strain gauges will be applied to the panel back-face, to measure the panel strain response. These data will serve for Finite Element model correlation. Additionally, the data will be used to find the contact force history of the impact via the Semi Analytical Finite Element (SAFE) method (Bartoil et al. [7]). This is an inverse problem that involves using a MATLAB optimazation algorithm which minimizes the differences between the strain gage measured wave and the SAFE-predicted wave by iteratively changing the force input history. Figure 76 shows some preliminary results for prediction of the contact force history of 38.1 mm diameter SHI impacting a 16 ply composite panel.

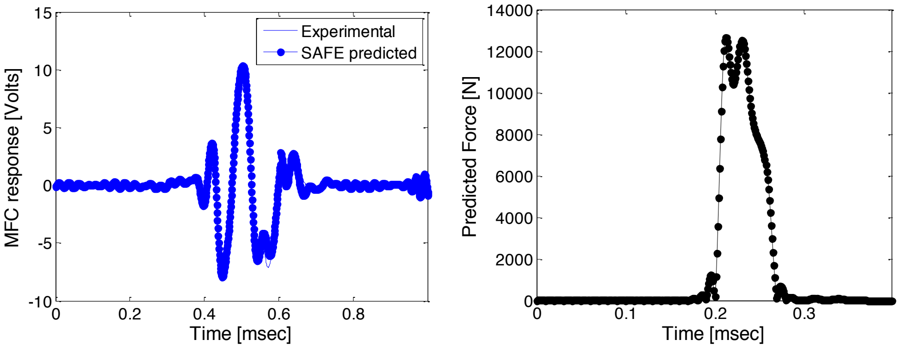

Figure 76: SAFE Force Identification for 38.1 mm Ice Impacting 16 Ply Composite Panel
(Left) Comparison of Experimental versus Sensor Response
(Right) Final Prediction of Impact Force History

2.2.5 Ice Projectile Basic Studies

A fundamental study of ice impact forces and the observation of fracture and breakup of ice during impact was completed. This investigation had been conducted to review the behavior of SHI as it impacts a force measurement bar (FMB). The FMB is essentially a waveguide measuring contact forces applied to one end of the bar (e.g., the transmission bar of a split Hopkinson pressure bar apparatus). It uses strain gages in a half Wheatstone bridge configuration to read the impact-generated strain waves, generating an output voltage, which can be converted into strain and then into contact force. The half-bridge set up allows for the measurement of only axial force, eliminating the bending effects of a slightly off-center hit. A typical plot of the force time histories is shown in Figure 77 for 50.8 mm ice impacting at 90 m/s. Additionally Figure 78 shows a summary of peak forces from all tests. This figure shows that teak force is found to be linearly related to the projectile kinetic energy.

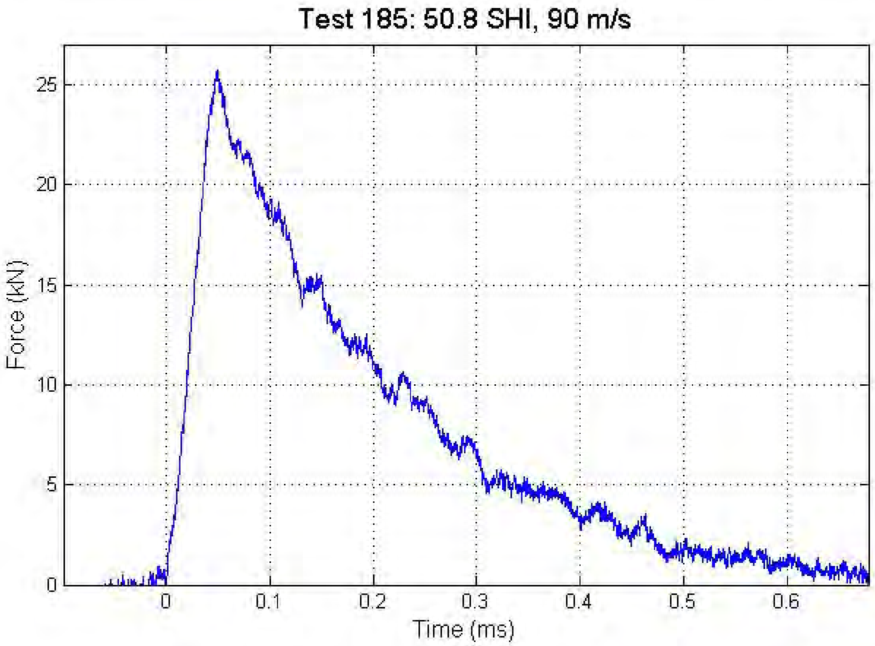

Figure 77: **"Typical" Force History; 50.8 mm Ice at 90 m/s**

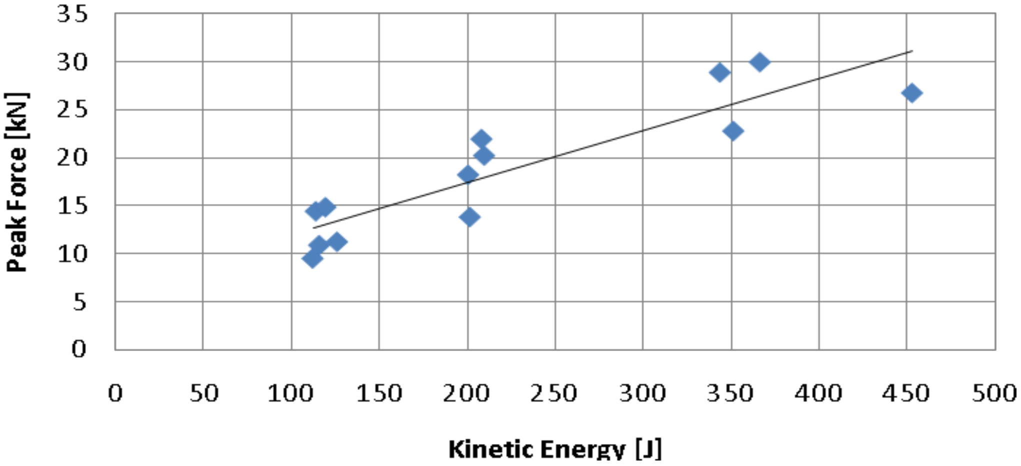

Figure 78: Peak Force Versus Kinetic Energy

A series of tests were conducted to investigate the effect of the SHI structure. The impacts defined so as to be directly comparable with two nominal velocities of 60 m/s and 80 m/s, two diameters of SHI (50.8 mm and 61.0 mm), and two forms of SHI: monolitic and flatwise layered. The construction of the monolithic ice is completed by filling the mold in a single-pour event while the flatwise layered construction of SHI consists of approximatly 10 layers, as shown in Figure 79 (note colored dye used to make ice darker to aid video capture). All layered ice was launched such that the layers are perpendicular to the path of movment. In Table 9, the velocity, peak force, and kinetic energy of each test is summarized.

Figure 79: Monolithic and Flatwise Layered SHI
(Orientations of Flatwise Layered SHI is for Photo Only)

Table 9: SHI Construction Study Test Summary

Test No.	Projectile (L=Layered)	Mass (g)	Velocity (m/s)	Peak Force (kN)	Kinetic Energy (J)
195	50.8 SHI	62.0	65.0	15.5	130.9
196	50.8 L SHI	61.1	62.6	16.0	119.8
197	50.8 SHI	61.8	82.4	21.5	210.0
198	50.8 L SHI	61.3	82.5	23.3	208.6
191	61.0 SHI	105.2	62.0	14.8	202.0
200	61.0 L SHI	107.6	61.1	18.7	201.0
184	61.0 SHI	110.1	81.7	32.0	367.6
199	61.0 L SHI	107.4	80.1	30.6	344.4

An analysis of this work reveals that the difference in construction of SHI does not significantly influence the behavior. Figure 80 shows that both the monolithic and flatwise layered SHI produce peak forces that fall onto the same linear trend relative to kinetic energy. Additionally, Figure 81 directly compares the contact force history of monolithic and layered 50.8 mm SHI impacting at 80 m/s. The force histories are seen to be essentially the same and thus it is concluded that flatwise layered construction provides no added “benefit” in terms of exhibiting higher toughness or greater force and impulse.

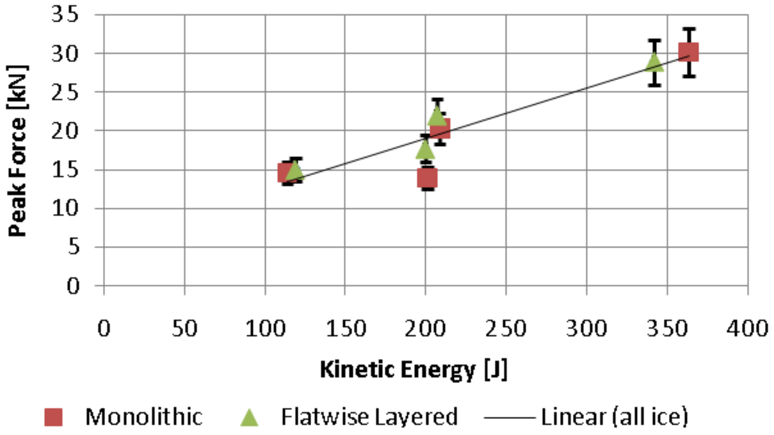

Figure 80: Peak Force versus Kinetic Energy for Monolithic and Flatwise Layered SHI

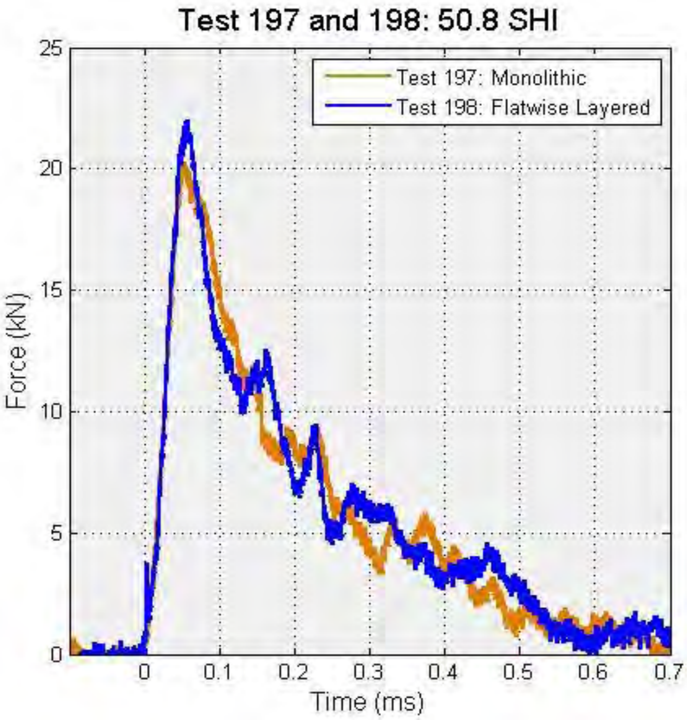

Figure 81: Comparison of Force History for Monolithic and Flatwise Layered SHI; 50.8 mm SHI at 80 m/s

Futher inspection was conductd into the behavior of the ice impact by analyzing high speed video still images against the impact force history. This is summarized in Figures 82 and 83 for 50.8 mm ice at 82.2 m/s. The images themselves reveal insightful observations, particularly during the uploading portion of the force history curve and the formation of axial (impact-direction) cracks up through image # 5, after which time the contact force decreases rapidly, corresponding to gross break-up of the ice projectile. The ice projectile still maintains its overall shape, except for the portion of the sphere that has been crushed and has flowed away.

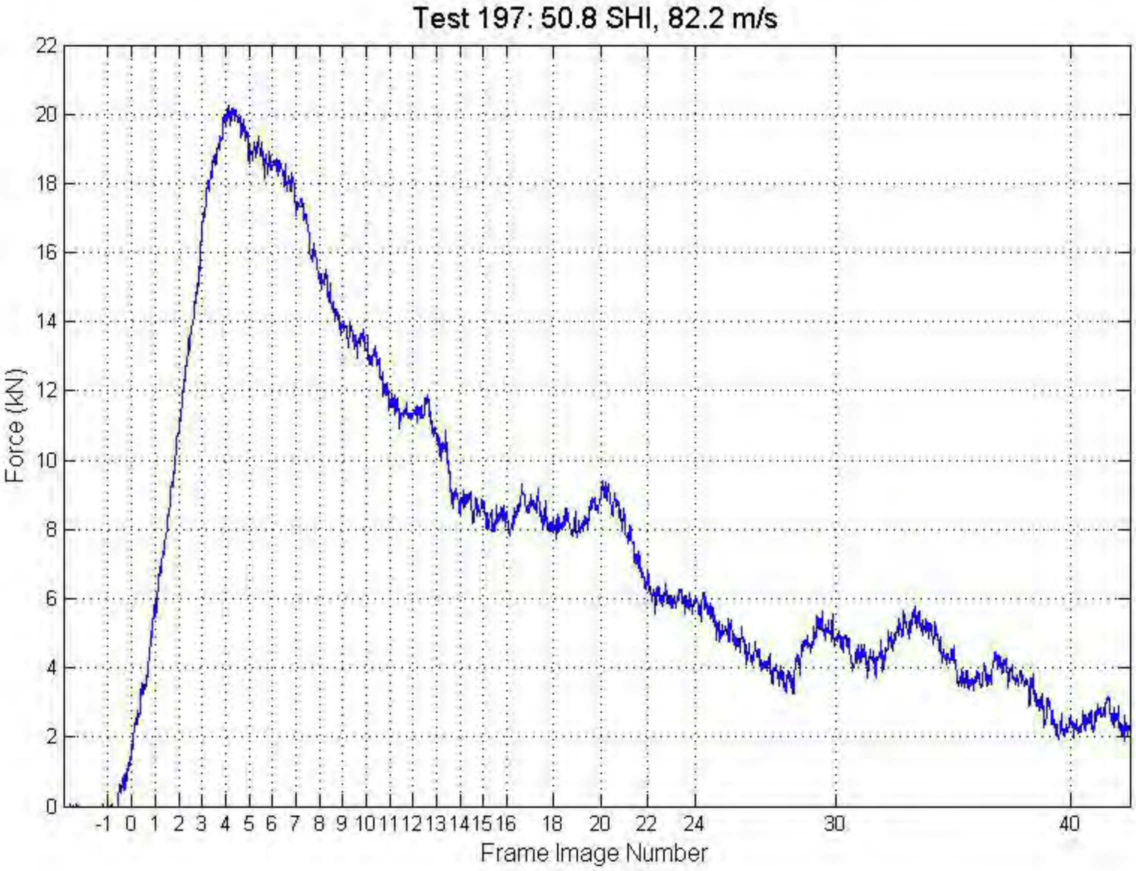

Figure 82: Frame Image Numbers on Force History; 50.8 mm Ice at 82.2 m/s

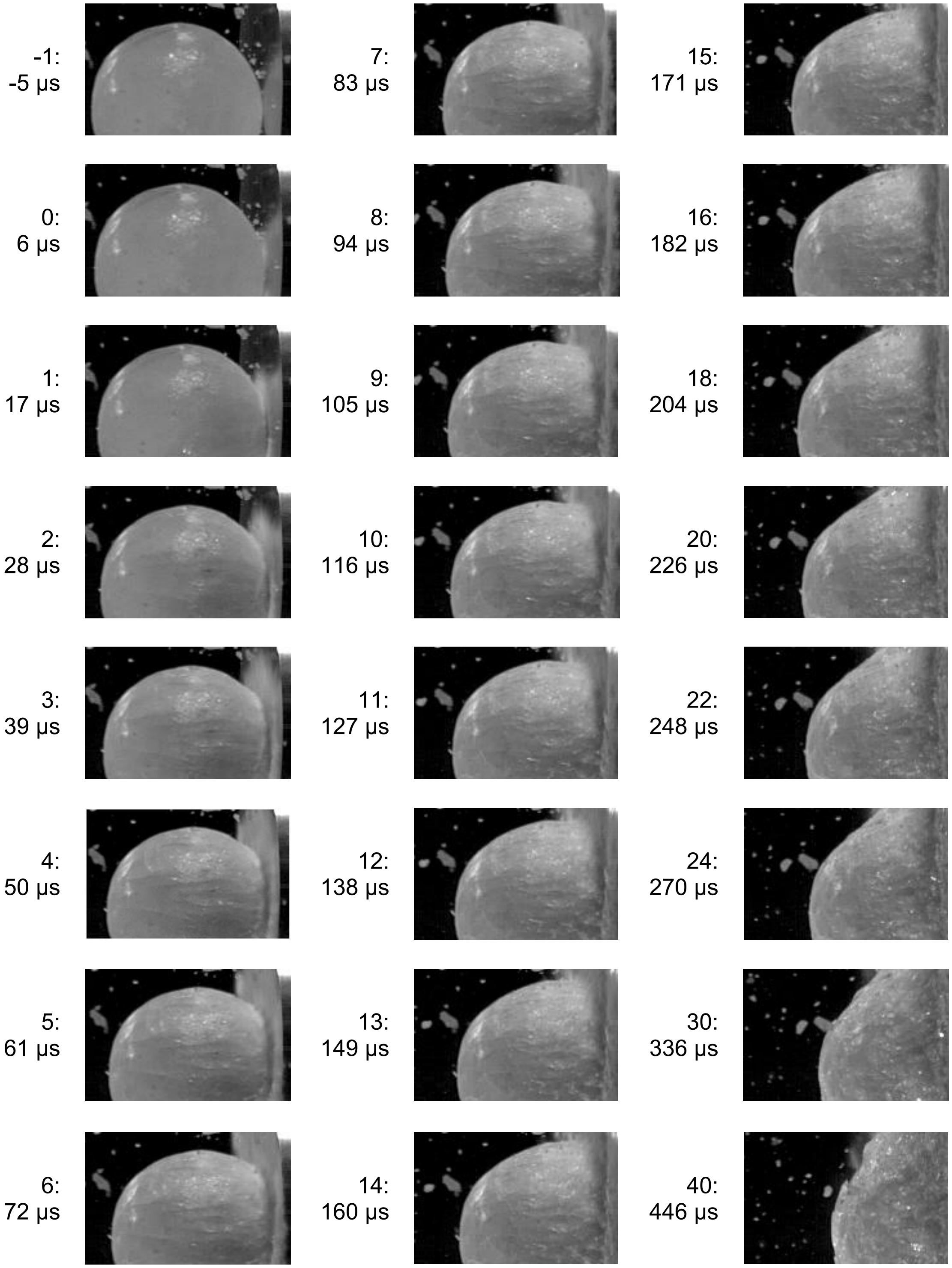

-1: -5 µs

0: 6 µs

1: 17 µs

2: 28 µs

3: 39 µs

4: 50 µs

5: 61 µs

6: 72 µs

7: 83 µs

8: 94 µs

9: 105 µs

10: 116 µs

11: 127 µs

12: 138 µs

13: 149 µs

14: 160 µs

15: 171 µs

16: 182 µs

18: 204 µs

20: 226 µs

22: 248 µs

24: 270 µs

30: 336 µs

40: 446 µs

Figure 83: SHI Impact Images – Frame Number and Time Relative to 1st Contact; 50.8 mm Ice at 82.2 m/s

2.2.6 Dynamic Finite Element Modeling

ABAQUS Explicit finite element models are being developed to accurately simulate ice impact events. Currently a quarter symmetric model is being used for model development with solid elements utilizing an elastic plastic material within ABAQUS that has properties tuned based on past test data (Park [8]). However, work is being conducted to establish a strain rate dependent ice model. Additionally the composite plate targets are being modeled to predict damage. The solid elements making up the composite plate are organized on a ply-by-ply basis and the material is a single orthotropic definition utilizing the orientation command in ABAQUS. The material behavior of these elements is governed by a user subroutine material model that degrades their properties once failure has initiated. In addition, this model employs ABAQUS cohesive zone fracture elements. These are placed between each layer of plate elements and are being used to predict delaminations. The model will be validated by test data (strain measurements, damage onset, extent of delamination) and used to further probe how parameters, such as local bending stiffness or deformation rate of projectile, affects the contact force development, supporting focused investigation on the scaling of peak force and its relationship to damage threshold force, i.e., when damage initiates in the composite.

A new ice projectile model is in development for use in the finite element modeling of ice impact. An ice model has been previously developed by H. Kim in DYNA-3D and ABAQUS finite element analysis tools (Kim and Kedward [2]).

The goal of the new ice projectile model is to create a material model which does not have to be tuned for the various testing conditions. To achieve this goal, a strain rate dependent failure model for this particular ice projectile is being implemented within the ABAQUS framework and correlated to impact tests onto a force measurement bar. These tests were performed at UCSD.

Current efforts have been focused on two aspects of the correlation between test and analysis. With high speed test video focused on the failure of the ice projectile recorded for the first time, the current finite element modeling approach can be compared by examining the failure characteristics of the projectile in the images. These images correlate well with the failure seen in the projectile during the simulation, as shown in Figure 84. Similar location and geometry cracks propagating along the projectile away from the point of impact, but stopping before they reach the opposite pole, are seen in both images. These cracks are thought to be due to the development of considerable hydrostatic tensile pressure within the ice sphere, upon initial stages of impact, which then cause tensile fracture in directions corresponding to peak principal stress. With this qualitative comparison of the kinematic behavior of the failing ice material, the failure model used in ABAQUS is shown to be capable of predicting the failure (behavior) of the ice projectile.

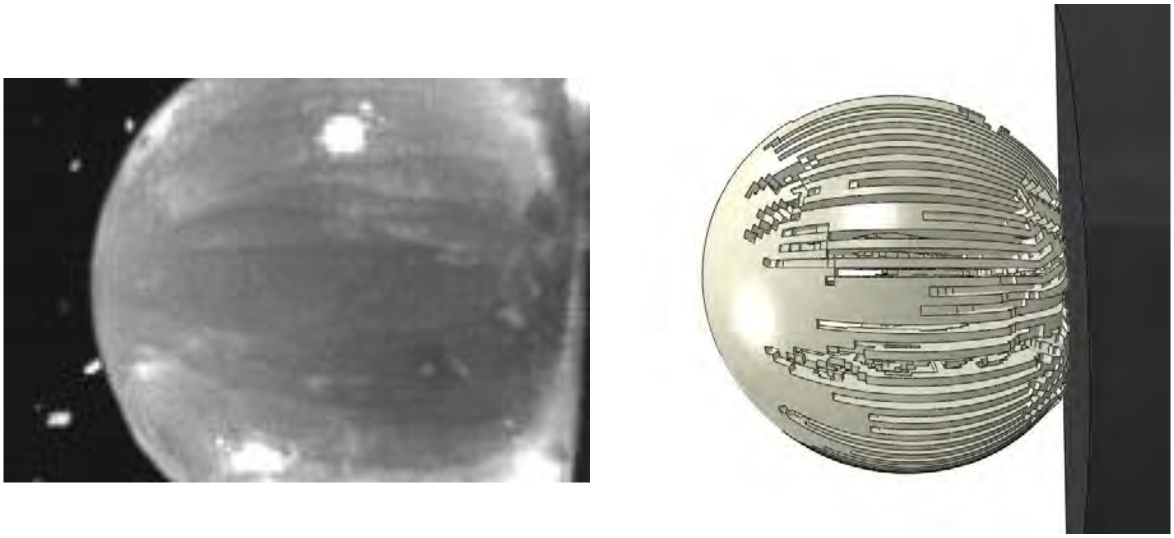

Figure 84. Comparison of Test 195 (61 mm Dia. at 61 m/s) Video (Left) and ABAQUS Simulation (Right) with Failed Elements Removed From View at 75 μs After Initial Contact.

The second and most important correlation is matching the experimentally measured force pulse. These current efforts are ongoing and involve picking the right strength and strain rate relationship based on test data (Kim and Kuene [9]) as well other material parameters available in the model. The sensitivity of these parameters is being studied in order to understand how to best adjust the model to achieve correlation among several tests.

The composite panel damage initiation and failure progression prediction research consists three parts. First are experimental impact tests onto carbon/epoxy composite material. Second is the development of finite element analysis (FEA) progressive failure model and third is the application this model. The development of a simulation tool that can be used to predict initiation of damage due to ice impact onto monolithic panels is underway. Finite element software ABAQUS/Explicit will be used in conjunction with a progressive failure VUMAT subroutine. The onset of select failure modes such as delamination and backside fiber failure will be predicted. Specifically ABAQUS cohesive zon elements will be used for delamination prediction and a progressive failure code will utilize failure mechanisms such as fiber breakage by max strain, matrix cracking using the LaRC (Pinho et al. [10]) modified Puck criteria, and non linear shear. Validation of models will be achieved via comparison with data collected in experimental work. ABAQUS models are in the process of being constructed and the VUMAT subroutine is currently undergoing a one element validation test.

The upcoming third phase of this research applies the model to look at the damage formation due to high velocity hail ice impacts onto monolithic panels. Key phenomena and parameters governing impact damage will be determined via investigations; specifically determining the scaling rules (models) for ice impacts. Furthermore use of the model to find if relationships between damage formation, FTE, and FTF can be generally defined and used to identify key parameters or physical quantities (e.g., panel bending stiffness D and panel aerial density). In addition, these validated models will be used to explore beyond the monolithic panel experimental work and develop a more in-depth understanding of impacts at locations adjacent to internally bonded details such as stiffeners or ribs and glancing impact damage. Finally the model can be used to establish a unified methodology for predicting damage initiation by variety of impactor projectile types such as bird, hail, tire fragment, runway debris, etc., as long as the projectile is modeled accurately.

3.0 Conclusions

Blunt impact sources studied by UCSD include wide-area high energy contacts with ground service equipment (GSE) and hail ice impact. Both are impact sources that can cause internal damage to composites with little or no external visual detectability.

The following conclusions are drawn from the research summaries given in Section 2 of this paper.

Wide Area GSE Impact:

- The rubber bumper applies load over much larger area relative to the “rigid” 3 in. radius indentor. This significantly affects the interlaminar shear stress developed at the edges of the indentor (larger area results in lower interlaminar shear for same applied load).
- The rigid 3 in. radius indentor produces localized damage at the site of contact, initially delaminations form, eventually resulting in full penetration of the surface, as observed in tests of panels Stringer00 and Stringer01.
- The rubber bumper does not produce localized damage under the contact footprint due to decreased interlaminar stress. Damage initiation occurs at loads up to 3X higher than the “rigid” 3 in. radius indentor. Furthermore the damage produced initiates away from the rubber bumper, at the shear ties

where high reaction forces produce interlaminar shear stress, i.e., damage does not initiate at the location of loading.

- Extensive delamination of both stringers was observed for loading by the rubber bumper on the skin spanning between two stringers (specimen Stringer02). In contrast, the rigid indentors did not produce any delamination of the stringer flanges.
- For the rigid 3 in. radius indentor, roughly the same force corresponding to delamination initiation was observed for two different test specimens with loading applied at two different locations (centered over stringer, on skin spanning between stringers). This confirms the notion of a critical threshold force being a key damage initiation metric.
- Final failure load of the stringer specimen indented by the rubber bumper is roughly 2X higher than the final failure load of specimens loaded by the rigid 3 in. radius indentor. The bumper-loaded specimen exhibited distributed damage away from indentation location, whereas the rigid indentor caused localized penetration.
- Permanent deformation of stringer panels was not visible following damage deformation, until after the 5th Loading of specimen Stringer02 when thee stringer was fully delaminated out to the panel edge. Intermediate failures (localized delaminations) were not visually detectable, regardless of specimen type and loading head material (rubber vs. “rigid” aluminum).

- Small scale damage formation plays a critical role in the ultimate failure of the stringer Phase I specimens, particularly for the rubber bumper. Small scale damage initiation occurs 1st in the form or shear tie delamination in the radius regions, then delamination of the stringer flanges at the reaction points (near shear ties) due to development of high interlaminar shear. The delaminations grow inwards towards the indentor location. These "small scale" damage modes accumulate to produce large scale damage– they must therefore be well studied and understood.
- Finite Element models predict large interlaminar stresses under the indentor and also at shear tie locations, within the stringer flanges. Interlaminar shear is the driving force for formation and growth of delamination of the stringer flanges.
- A finalized test configuration for the large ~6x4 ft. frame specimen panels has been established using UCSD's Powell Structural Research Lab 1-D shake table system. While this will be used to apply slow quasi-static indentation to the first phase of specimens, the shake table system allows for future dynamic testing to be conducted. The specimens will be mounted vertically to a high force capacity strong wall which is large enough to permit up-scaling to larger, full-scale barrel test articles (full or half barrel) from a wide body aircraft.

High Velocity Hail Ice Impact:

- Failure Threshold Energy (FTE) levels are being established for T800/3900-2 unidirectional composite on 8, 16, and 24 ply quasi-isotropic specimens of monolithic skin construction.
- Test methods and data processing techniques have been established to allow non-direct determination of the contact forces developed during an impact event. These forces will be used as part of establishing a generic “force scaling” law that would allow one to predict the peak forces developed onto any composite structure, flexible to rigid, and thereby estimate whether damage will initiate based on the critical threshold force concept.
- Fundamental studies focused on ice projectile impact physics were conducted using fast-response force measurement and accompanying 90,900 frames/sec high speed video. No significant difference between flat-wise layered vs monolithic ice sphere construction was found.
- High speed video analysis, correlated with impact contact force time history, shows the initial “uploading” portion of force data to develop in conjunction with longitudinal cracks growing in the ice sphere, reaching a critical density and length towards the back of the sphere, and coinciding with the time at which peak force occurs. Afterwards the force drops and is mostly from ice debris flow impinging onto the target surface.
- Numerical simulation models of spherical ice projectiles have been established and found to accurately represent the physics of ice fracture

and degradation, including formation of longitudinal cracks in the initial portion of the force history curve.

4.0 Future Follow-On Activities

The project activities summarized herein are ongoing. Most notably, the Frame Specimen panels are to be tested in June/July of 2010 at UCSD. Future scope of activities are described below.

Wide Area GSE Impact:

- Experimental investigation of larger-sized specimens – 5-7 frames (4-6 bays) or even ¼ to ½ barrel. Specimens of this size scale need to be obtained from industry participants.
- Beech Starship full barrel tests. This fuselage section is at UCSD at present and can be tested using the 1-D shake table system.
- Investigate dynamic effects via analyses and experiment. Also investigate glancing impact effects – confirm previous year's study prediction of lower angle impacts causing higher transmitted impulse.
- Establish detailed FE simulation and prediction capability that includes small-scale damage formation using element types that are amenable to large-structure modeling (i.e., shell elements). Fundamental research question is how to make shell elements effectively represent stiffness degradation due to interlaminar failures (which are not predicted by standard shells).

- Implement photogrammetry system for detailed geometry mapping of panels before and after indentation/impact to gain quantitative description that can be related to visual detectability.
- Conduct focused small scale specimen failure studies and accompanying model development and correlation. This is to understand how small scale damage develops (e.g., delaminations in shear ties, in stringer flanges) and grows to form large level of damage.
- Investigate the residual strength of blunt impacted panels – e.g., load previously-indented/damaged stringer panels in compression to determine the knockdown in load capability as function of penetration vs. stringer delamination damage modes.
- Conduct full scale ground vehicle impact tests using OEM equipment, or equivalent.

High Velocity Hail Ice Impact:

- Conduct comprehensive experimental study of sandwich panel impacts. This type of study has never been done for ice. Preliminary data show significantly lower (3-4X) damage resistance to hail impact for composite face sheet when compared to same-thickness monolithic panel. Also include computational model development focused on damage initiation prediction.

- Investigate internal structure effects on damage resistance and damage modes. Of particular interest is impact locality to stringers, stiffeners, thickness transitions, splices, etc.

5.0 References

1. International Air Transportation Association 2005, “Ground Damage Prevention Programme Targets 10% Cost Reduction,” Industry Times, Edition 7, September, Article 4.
2. Kim, H. and Kedward, K. T., “Modeling Hail Ice Impacts and Predicting Impact Damage Initiation in Composite Structures,” AIAA Journal, Vol. 38, No. 7, 2000, pp. 1278-1288.
3. Kim, H., Kedward, K.T., and Welch, D.A., “Experimental Investigation of High Velocity Ice Impacts on Woven Carbon/Epoxy Composite Panels,” Composites Part A, Vol. 34, No. 1, 2003, pp. 25-41.
4. Daniel, I & Ishai, O 2006, *Engineering Mechanics of Composite Materials,* 2nd Edition, Oxford University Press, New York.
5. Nightingale, J., Experimental Correlation between Intrinsic Material Properties and the Failure of Composite Laminates under Ice Impact. Purdue University MSAAE Thesis 2006.
6. Liyong Tong and Costas Soutis, Recent Advances in Structural Joints and Repairs for Composite Materials (Springer, 2003).
7. Ivan Bartoli, Alessandro Marzani, Howard Matt, Francesco Lanza di Scalea, and Erasmo Viola. “Modeling wave propagation in damped waveguides of arbitrary cross-section” Proc. SPIE 6177, 61770A (2006).
8. Park, Hwun. “Resistance of Adhesively Bonded Composite Lap Joints to Damage by Transverse Ice Impact” Masters Thesis, Purdue University. 2006.
9. Kim, H. and Kuene, J., “Compressive strength of ice and impact strain rates,” Journal of Material Science, Vol. 42, 2007, pp. 2802-2806.
10. Pinho, Silvestre T., Davila, Carlos G., Camanho, Pedro P, Iannucci, Lorenzo, and Robinson, Paul. Failure Models and Criteria for FRP Under In-Plane or Three dimensional Stress States Including Shear Non-linearity. NASA/TM-2005-000000. Feburary 2005.